

NORTHWESTERN UNIVERSITY

Atomically-Precise Synthesis of Platinum
catalysts on Strontium Titanate using Atomic
Layer Deposition

A DISSERTATION

SUBMITTED TO THE GRADUATE SCHOOL
IN PARTIAL FULFILLMENT OF THE
REQUIREMENTS

For the degree

DOCTOR OF PHILOSOPHY

Field of Materials Science and Engineering

By

Chuandao Wang

Evanston, ILLINOIS

December 2014

UMI Number: 3669341

All rights reserved

INFORMATION TO ALL USERS

The quality of this reproduction is dependent upon the quality of the copy submitted.

In the unlikely event that the author did not send a complete manuscript and there are missing pages, these will be noted. Also, if material had to be removed, a note will indicate the deletion.



UMI 3669341

Published by ProQuest LLC (2014). Copyright in the Dissertation held by the Author.

Microform Edition © ProQuest LLC.

All rights reserved. This work is protected against unauthorized copying under Title 17, United States Code



ProQuest LLC.
789 East Eisenhower Parkway
P.O. Box 1346
Ann Arbor, MI 48106 - 1346

© Copyright by Chuandao Wang 2014

All Rights Reserved

ABSTRACT

Atomically-precise Synthesis of Platinum Catalysts on Strontium Titanate using Atomic Layer Deposition

Chuandao Wang

This dissertation examines growth of platinum nanoparticles from atomic layer deposition (ALD) on SrTiO₃ using a characterization approach that combines imaging techniques and other complementary analytical methods. The primary suite of characterization probes includes high resolution transmission electron microscopy (HRTEM), high angular annular dark field-scanning transmission electron microscopy (HAADF-STEM), X-ray photoelectron spectroscopy (XPS), inductively coupled plasma-atomic emission spectroscopy (ICP-AES) and The Fourier transform infrared (FTIR). All imaging techniques reveal that Platinum nanoparticle grown via ALD are ultrafine with very narrow size distribution and well dispersed on either single crystal or nanocuboid shape strontium titanate (SrTiO₃, STO) substrates.

The fundamental growth mechanism of Pt nanoparticles is investigated in details using HAADF-STEM, XPS and ICP-AES. During the initial cycle of ALD the deposition process begins with nucleation followed by growth, both occurring on a fast time scale relative to the deposition time. The final size is determined by net Pt deposition which is affected by reaction temperature. For multiple cycles, the particle size increases with the number of ALD cycles which also relies on net Pt deposition during that cycles. The increase in size per cycle is significantly lower than first cycle. This effect is due to carbonaceous material left on the surface

from decomposition of the MeCpPtMe_3 ligands. A negligible change of particle density during multiple cycle ALD deposition suggests a minimum secondary nucleation or particle coalescence.

The influence of different ALD parameters, e.g. reaction temperature, number of cycles, substrate, reagents and type of ALD methods, to acquired Pt nanoparticles are investigated and discussed individually. Particle size, density and loading vary with reaction temperature, number of cycles and type of ALD method. Pt growth orientation and shape can be changed by using different substrates. Application of Winterbottom construction to the observed shape of Pt nanoparticles on strontium titanate nanocuboids revealed that the surface structure of substrates and particle shape, growth orientation are interlinked, with control over one allowing equally precise control over the other. And changing the 2nd reagent can leads to different chemical states and compositions of formed particles. Thus, atomic level controlling synthesis in particle size, density, loading, chemical composition, growth orientation and thermodynamic shape of deposited Pt nanoparticles can be achieved by tuning these ALD parameters. Combining these observations will allow one to understand and improve catalytic performance when these particles are used for catalytic purposes, as selectivity and reactivity are often heavily dependent on catalyst size, shape, dispersion, exposed surfaces and chemical state. By choosing CO oxidation as a probe reaction, we revealed that Pt catalyst performance is strongly depends on their supporting material and size, as changing of which will alter the number or type of active sites of Pt catalysts which will change their catalytic performance.

Professor Peter C. Stair

Professor Laurence D. Marks

Acknowledgements

I would like to begin by thanking my advisors, Professors Laurence Marks and Peter Stair for their support, guidance, and advice over the past five years. Without their input, I could not have achieved any of my academic goals and they make it possible to continue to the next opportunity. Through the research I performed with both, I have learned much about science, and discovered many things about myself as well. I also would like to thank my committee members, Professors Michael Bedzyk and Scott Barnett, for serving on my doctoral committee and for their helpful discussions. I really appreciate their time, energy, support and feedback which they have provided along the way and each time that the committee has sat for my presentations.

As principal collaborators, I want to recognize Yuyuan Lin and Linhua Hu. They have not only supplied me the STO nanocuboids to support this work, but also provide many opportunities for me to conduct research and improve my work. I am also indebted to Alexis Johnson for revise so many papers for me patiently and offering thoughtful discussions. I am grateful to Neil Schweitzer for helping with FTIR data collection and setting up GC for final CO oxidation catalytic test to end the current project. Without them, all this work might not exist, certainly not in their current form. A special mention also goes to those students who will be taking the results outlined herein and moving them into the future: Lawrence Crosby and Pratik Koirala. I also owe thanks to all the people behind the scenes, who made things run: Pat and James in the Catalysis center, Shuyou Li, Jingsong Wu and Xinqi Chen in NUANCE center, for helping me when I got in trouble with TEM and XPS. And thank you as well to the rest of the Marks and Stair groups, past and present, who have contributed insights at meetings and through informal discussions.

Thank you to all of my relatives and for all the support you've offered along the way in good times and bad. To my grandparents, grandparents-in-law, cousins, especially my aunts and uncles, for always being there and supporting me and believing in me and for all the other things you've done, which is more than I could ever properly thank you for. You are the best grandparents anyone could ever ask for. Thank you especially to Mom and Dad: for raising me up, always believing in me, for supporting me and helping me through all my difficulties, for teaching me how to think for myself and figure things out, and for other things without number. I love you all.

Specially, thank you to Lishan. You are the wonderful girl I have met. You are everything I could ever want or hope for, thank you for appearing in my life and for your love, friendship, understanding, joy, and, of course, for your smile.

Finally, thank you to all these people who I really treat as friend and enjoyed the time with for the past years: Junchen, Qianfei, Linlin, Yu, Shuangping, Zhenyu, Xiaohan, Betty, Ting, Mike, Katie, Martin, Yang, Jiajun, Zhongbi, and everyone else who I left out. Special thanks to Yongli, Shiqiang and Ye. With you guys, the winter here is always exciting as snowboarding trip is organized so diligently.

Table of Contents

Abstract	3
Acknowledgements	5
List of Figures	10
List of Tables	16
Chapter I: Metal Oxide Supported Noble Metal Catalysts	17
1.1: Introduction.....	18
1.2: Heterogeneous catalyst preparation.....	21
1.2.1 Traditional methods for preparation of catalytic material.....	21
1.2.2 New application of atomic layer deposition for catalyst synthesis.....	23
Chapter II: Synthesis Approach of High Surface Area Catalytic Support with Specific Exposed Surfaces	29
2.1: Introduction.....	30
2.2: STO-NCs synthesis from lamella micro-emulsion.....	32
2.2.1 STO nanomaterials synthesis from different microemulsion structures.....	32
2.2.2 Electron microscopy.....	33
2.3: Result and discussion.....	34
2.3.1 Morphology of as-synthesized STO-NCs.....	34
2.3.2 Mechanism of formation of STO-NCs beyond synthesis.....	36
2.3.3 Influence of covered surfactant to surface properties.....	39
2.3.4 Surfactant removal or replacement.....	40
Chapter III: ALD Synthesis of Platinum Nanoparticles on Single-crystal SrTiO₃	50
3.1: Introduction.....	51
3.2: Experimental.....	53
3.2.1 Sample preparation and wet chemical etching.....	53
3.2.2 X-ray photoelectron spectroscopy (XPS).....	55
3.2.3 Transmission electron microscopy sample preparation and image recording.....	56
3.2.4 Platinum ALD.....	57
3.3: Result and discussion.....	58

3.3.1 Carbon removal and hydroxyl group enrichment on SC-STO (100) surface	58
3.3.2 Morphology and composition study of SC-STO before ALD	60
3.3.3 Study of deposited Pt nanoparticles on SC-STO substrates with different treatment	60
3.4: Conclusion	61
Chapter IV: Controllable ALD Synthesis of Platinum Nanoparticles by Tuning Different Synthesis Parameters	72
4.1: Introduction	73
4.2: Experimental	76
4.2.1 Morphology and surface structure of two types of STO-NCs	76
4.2.2 Platinum ALD deposition	77
4.2.3 Characterization	79
4.3: Results and discussion	80
4.3.1 General morphology and structure of Pt/STO-NCs	80
4.3.2 Size measurement from HAADF images depends on probe size	81
4.3.3 Temperature dependence of Pt ALD synthesis	83
4.3.4 Dependence of size and density of Pt nanoparticles on number of cycle and ALD method	85
4.3.5 Influence of supporting material on the structure and loading of ALD formed Pt nanoparticle	87
4.3.6 Role of reagent in ALD process	89
4.3.7 Pt nanoparticle formation through nucleation and diffusion controlled growth process	92
4.4: Conclusion	100
Chapter V: Winterbottom Shape Tailoring of Platinum Nanoparticles on Perovskite Oxides $Ba_xSr_yTiO_3$	123
5.1. Introduction	124
5.2: Experimental	126
5.2.1 Substrates synthesis	126
5.2.2 Pt atomic Layer deposition	126

5.2.3 Pt nanoparticle characterization.....	127
5.3: Results and discussion.....	127
5.3.1 General morphology and structure of BTO-NCs and STO-NCs.....	127
5.3.2 Platinum nanoparticles deposited on BTO-NCs and STO-NCs.....	128
5.3.3 Morphology and shape of platinum nanoparticles on BTO-NCs and STO-NCs.....	128
5.4: Conclusion.....	131
Chapter VI: Platinum/Strontium Titanate-Nanocuboids System Towards Catalytic Application.....	141
6.1: Introduction.....	142
6.2: Experimental Methods.....	143
6.2.1 Catalyst supporting material preparation.....	143
6.2.2 Pt atomic layer deposition.....	144
6.2.3 Catalyst characterization.....	144
6.2.4 Catalytic testing.....	148
6.3: Results and discussion.....	149
6.3.1 General information of different Pt catalysts.....	149
6.3.2 Fourier transform infrared studies of CO adsorption.....	149
6.3.3 Carbon monoxide combustion catalytic test.....	152
6.4: Conclusion.....	154
Chapter VII: Conclusion.....	164
References.....	168

List of Figures

Figure 1.1. Cubic perovskite unit cell. Blue spheres represent the A cations, yellow spheres represent the B cations, and red spheres represent oxygen anions forming an octahedral.....	27
Figure 1.2. Schematic of compositions a pervoskite structure.....	28
Figure 1.3. An ALD thin film deposition cycle shown schematically with the TMA-H ₂ O process as an example.....	28
Figure 2.1. Schematic diagram shows the procedure for Pt/STO-NCs TEM sample preparation on copper TEM grids.....	42
Figure 2.2. HREM image of a typical STO-NC with a power spectrum inset.....	42
Figure 2.3. HAADF images of different STO-NCs (a~l) are the nanocuboids1~12 in Table 2.1.....	44
Figure 2.4. TEM images of STO-NCs with oleic acid synthesis. (a) Experimental HREM image of STO-NC along [110], where the bright spots can be interpreted as atoms. (b) Low magnification image of (a). (c) FFT image of (b). (d) Simulated HREM image of (a). In (a) the sample thickness and defocus are increasing from left to right. Therefore, (d) is generated using 3 images simulated with continual changing defocus and thickness, increasing from left to right.[1].....	45
Figure 2.5. Direct observation of lamellar structure of oleic acid. (a,b) cyro-EM image of STO-NCs dispersed into oleic acid. (c) negative staining TEM image, showing the average 3.4 nm thickness of the double layer of oleic acid without water.....	46
Figure 2.6. Schematic figure of the lamellar structure of oleic acid at different temperatures: (a) 18 °C, (b) 160 °C. (c,d) STO-NCs form three layers of water and two layers of oil, total thickness 7.9 nm, very similar to the 8 nm thickness of the synthesized STO-NCs. The reaction process is (1) coordination of Sr ²⁺ with oleic acid and amorphous gel in basic condition at room temperature, (2) formation of SrTiO ₃ nuclei in the water phase (water layer), and (3) growth to STO-NCs(blue color).....	47
Figure 2.7. X-ray photoelectron spectroscopy (XPS) studies shows the removal of carbon species from STO-NCs after 15 min ozone bath at 200 °C.....	48

- Figure 2.8.** Amorphous carbon fringes generated by electron beam irradiation shows the contamination level of the sample (a) STO-NCs without ozone treatment shows clear amorphous fringes after 5 min beam irradiation (b) STO-NCs with ozone bath for 15 min at 200 °C didn't show any evidence of contamination after 5 min beam irradiation..... 49
- Figure 3.1.** Crystal structures for SrTiO₃ (b). The respective lattice constants are 0.3905 nm. The space group of SrTiO₃ is $P\bar{m}3m$ (#221)..... 63
- Figure 3.2.** Diagram shows etching procedure of different sample (a) as-purchased EPI polished sample (b) mechanic polished sample..... 63
- Figure 3.3.** X-ray photoelectron spectroscopy ESCALAB 250Xi at Nuance Center Northwestern University..... 64
- Figure 3.4.** (a) O 1s core level XPS peaks of SC-STO with Gaussian profiles denoted as O1s and OH, respectively; (b) C 1s and Sr 3p_{1/2} XPS peaks of SC-STO with Gaussian profiles denoted..... 65
- Figure 3.5.** (a) Schematic diagram shows the procedure of single crystal strontium titanate TEM sample preparation. (b) Image of a rotary cutter (c) A Gatan Dimple Grinder (d) A Gatan Precision Ion Polishing System..... 66
- Figure 3.6.** (a) A photograph of atomic layer deposition equipment used in this work. (b) Schematic diagram of all connected components of the ALD system..... 67
- Figure 3.7.** Surface composition evolution of carbon and OH species with different chemical etching. (a) OH species changing with FA-HP and BHF-HP etching. (b) OH species changing with FA-HP and BHF-HP etching. (c) (d) Carbon and OH on SC-STO with BHF-HP etching at elevated temperature..... 68
- Figure 3.8.** HRTEM, dark field and bright field image of as-prepared SC-STO TEM sample (a),(b),(c) and BHF-HP etched SC-STO TEM sample (d),(e),(f), inserted image in (a)(d) is diffraction pattern of corresponding sample. (g) (h) is XPS C1s and O 1s peak of two types of TEM sample. 69
- Figure 3.9.** HRTEM of Pt/SC-STO (a) Pt deposited on as-prepared TEM sample. (b) Pt deposited on BHF-HP etched SC-STO TEM sample..... 70
- Figure 3.10.** Pt 4f core level XPS peaks of (a) Pt/as prepared SC-STO TEM (b) Pt/BHF etched SC-STO..... 71

Figure 4.1. TEM images of STO-NCs with two different hydrothermal synthesis methods. (a), (c) STO-NCs with oleic acid synthesis which is described in Chapter II. (b),(d) STO-NCs with acetic acid synthesis as described by Federico et. al.....	102
Figure 4.2. (a) Image shows STO-NCs substrates are well spread in a stainless steel tray before loaded into ALD reactor (b) Schematic diagram shows the N ₂ flow route during Pt precursor deposition for ABC-type and static ABC-type ALD.....	103
Figure 4.3. A light yellow solution of 5 mg Pt/STO dissolved in a mixture of 1 mL of nitric acid with 3 mL of hydrochloric acid.....	104
Figure 4.4. (a) A HREM image of Pt/STO-NCs (oleic acid) (b) TEM image of Pt/STO-NCs (acetic acid) obtained with 5 cycles at 200 °C using MeCpPtMe ₃ and H ₂ O.....	104
Figure 4.5. HAADF images of Pt/STO-NCs (1 cycle 300 °C) taken with a range of electron beam probe sizes (a) 1.5 nm (b) 1.0 nm (c) 0.7 nm (d) 0.5 nm (d) 0.2 nm.....	105
Figure 4.6. Measured nanoparticle size as a function of used electron probe size based on different samples (a) Pt/STO-NCs 1 cycle 300 °C (b) Series of Pt/STO-NCs synthesis with 1 cycle at different reaction temperature.....	106
Figure 4.7. HAADF images of Pt/STO-NCs(OA) synthesized under reaction temperatures of (a) 200 °C (b) 250 °C (c) 300 °C.....	106
Figure 4.8. Pt particle size plotted as a function of ALD reaction temperature.....	107
Figure 4.9. (a) Diagram shows definition of particle density, the image is HAADF image of Pt/STO-NCs (oleic acid) synthesized with 1 cycle AB type ALD at 300 °C. (b) Pt particle density as a function of ALD reaction temperature.(c) Diagram illustrates that particles from both top and bottom surface will contribute the particle density measurement.....	108
Figure 4.10. Pt weight loading as a function of ALD reaction temperature.....	109
Figure 4.11. Pt particle density as a function of commenced number of ALD cycle under two different ALD reaction temperatures of 200 °C and 300 °C.....	110
Figure 4.12. Images of Pt/STO-NCs synthesized using (a) MeCpPtMe ₃ and H ₂ O (b) MeCpPtMe ₃ and O ₂ . In each image, left and right sample are Pt deposited on oleic acid and acetic acid synthesized STO-NCs respectively.....	111
Figure 4.13. HREM image of Pt on (a) STO-NCs (OA) obtained by 10 cycles tradition ALD at 200 °C. (b)STO-NCs (AA).....	112

Figure 4.14. XPS studied Pt 4f/Ti 2p ratio synthesized using oxygen and water as a function a deposition cycles.....	113
Figure 4.15. XPS Pt 4f spectroscopy of Pt/STO-NCs (Oleic Acid) deposited with 6 cycles AB type ALD at 250 °C (a) oxygen (b) H ₂ O.....	114
Figure 4.16. Pt(0) and Pt(II)+Pt(IV) percentage of Pt/STO-NCs deposited using water and oxygen as a function of number of ALD cycles.....	115
Figure 4.17. XPS I(C 1s)/I(Sr 3p) ratio of Pt/STO-NCs prepared using water and oxygen as B reagent.....	116
Figure 4.18. Measured Pt particle size depends on Pt precursor dosing time based on HAADF image.....	117
Figure 4.19. Schematic of nucleation process of a new phase on an substrates, $\gamma_{pg}, \gamma_{sg}, \gamma_{sp}$ is interfacial energy between Pt-Gas, substrate-gas, substrate-Pt.....	117
Figure 4.20. Diagram showing enthalpy of formation. Pt-O-X-STO is the Pt configuration after Pt precursor adsorption and ligands elimination.....	118
Figure 4.21. Schematic diagram showing the formation of a depletion boundary after nucleation during Pt ALD process.....	118
Figure 4.22. Pt particle size as a function of commenced number of ALD cycles measured based on HAADF image.....	119
Figure 4.23. Platinum (a) particle size (b) Particle density as a function of ALD reaction temperature after single cycle synthesis. (c) Pt weight loading as a function of ALD reaction temperature. The black curve shows the difference between calculated and ICP-AES measured loading.....	120
Figure 4.24. (a) C 1s/Ti 2p ratio from XPS data of Pt/STO-NCs deposited with different number ALD cycle. (b) ICP-AES measured net Pt loading change during a specific cycle.....	121
Figure 4.25. Pt loading as a function of number of ALD cycles at 200 °C and 300 °C from ICP-AES measurement. For comparison particle loading measured from HAADF is included.....	121
Figure 4.26. Schematic representation of Pt particle formation on oxide surface for 1 st ALD and multiple cycles synthesis.....	122
Figure 5.1. (a), (b) TEM images and (c) Aspect ratio (Length/Width: L/W) plots of BaTiO ₃ (Top row) and SrTiO ₃ (bottom row).....	133

- Figure 5.2.** HRTEM images of (a) STO-NCs (b) BTO-NCs. The insert image is a live FFT image of corresponding HRTEM images..... 134
- Figure 5.3.** HAADF-STEM images of (a) Pt/BTO-NCs (b) Pt/STO-NCs. Both of which is deposition with 2 cycles of ALD at 250 °C. (c) Pt particle size as a function of commenced number of ALD cycles on STO-NCs and BTO-NCs substrates measured based on HAADF images..... 135
- Figure 5.4.** HRTEM images of (a) Pt/BTO-NCs, 3 cycles ALD at 200 °C (b) Pt/STO-NCs, 3 cycles ALD at 200 °C. The insert image shows a lattice fringe mismatch between substrates and deposited Pt nanoparticles..... 136
- Figure 5.5.** HRTEM images shows Winterbottom shape of Pt nanoparticle deposited on (a) (b) BTO-NCs (c) STO-NCs. A simulated Winterbottom shape is overlaid near the Pt nanoparticle..... 137
- Figure 5.6.** Wulff construction of a cluster with (100) and (111) surface exposed. Different ratio shows different shape (a) $\gamma_{111} : \gamma_{100} = 0.84$ (b) $\gamma_{111} : \gamma_{100} = 0.7$ 138
- Figure 5.7.** Cross section of a cluster supported on a (111) facet for a positive (a) and a negative (b) value of the effective surface energy γ' . H denotes the height of the cluster..... 139
- Figure 5.8.** Winterbottom construction for Pt on a substrate (a) shows difference in Wulff shape caused by $\gamma_{111} : \gamma_{100}$ ratio. (b) shows different degree of truncation caused by difference in $\gamma_{interface} - \gamma_{STO}$ 140
- Figure 6.1.** Images of (a) Nicolet 6700 DRIFTS (b) reactor BenchCat 4000 with microreactor and clamshell furnace marked out in red box (c) Agilent GC..... 155
- Figure 6.2.** (a) A typical FTIR spectra of CO adsorption on Pt surface, three peaks area are assigned to bridging/three-fold, linear CO and CO on STO-NCs substrates. (b) A detail peak shows CO adsorption on STO-NCs, the adsorption can be easily desorbed..... 156
- Figure 6.3.** FTIR CO spectras dosen't show obvious change for thermal desorption at 100 °C four different sample (a) Pt/Al₂O₃(commercial) (b) Pt/STO-NCs(AA) prepared using 6 cycles ALD deposition at 250 °C (c) Pt/STO-NCs(OA) prepared using 6 cycles ALD deposition at 250 °C (d) Pt/STO-NCs(AA) prepared using 3 cycles ALD deposition at 250 °C..... 157

- Figure 6.4.** FTIR CO spectra evolves with different oxygen dosing duration on four different sample same as described in Figure 6.3..... 158
- Figure 6.5.** Initial CO adsorption and resorption after oxygen removal on four different Pt samples same as Figure 6.3. The inserted spectras in (b) and (d) indicate that linear CO resorption peaks changed remarkably comparing to initial CO adsorption on Pt/STO-NCs(AA)..... 159
- Figure 6.6.** FTIR CO spectra evolves with different treatment on four different sample same pretreated using oxygen exposure(a)Pt/Al₂O₃(commercial) (b) Pt/STO-NCs(AA) prepared using 6 cycles ALD deposition at 250 °C (c) Pt/STO-NCs(OA) prepared using 1 cycles ALD deposition at 200 °C (d) Pt/STO-NCs(OA) prepared using 6 cycles ALD deposition at 250 °C..... 160
- Figure 6.7.** CO catalytic test results of different Pt catalysts (a)(b) CO conversion as a function of $W_{\text{total Pt/F}}$ and $W_{\text{surface Pt/F}}$. (c)(d) Plot of CO conversion of Pt/Al₂O₃ clearly shows deactivation after 5 hours test..... 161
- Figure 6.8.** HAAF images of three different Pt/STO-NCs before(left side) and after(right side) CO oxidation test (a),(b) 6c 250 °C Pt/STO-NCs(AA) (c),(d) 3c 250 °C Pt/STO-NCs(AA) (e),(f) 6c 250 °C Pt/STO-NCs(OA)..... 162
- Figure 6.9.** HAAF images of Pt/Al₂O₃ (a) before and (b) after CO oxidation test..... 163
- Figure 6.10.** (a) TOFt (b) TOFs as a function of Pt particle size of different Pt catalysts..... 163

List of Tables

Table 1.1. Atomic positions in cubic perovskites.....	27
Table 2.1. Results for the three dimensional analysis of the SrTiO ₃ nanocuboids.....	43
Table 3.1. Summary of XPS analysis of Pt deposited on two type of SC-STO sample.....	70
Table 4.1. Comparison between ABC-type and Static ABC type ALD.....	103
Table 4.2. Dependence of size and density of Pt nanoparticles on number of cycle and ALD method under two reaction temperatures of 200 °C and 300 °C.....	110
Table 4.3. Migration Distance (300s) of single Pt atom on STO-NCs substrate under different reaction temperature.....	119
Table 6.1. Linear CO adsorption fine peak composition of different Pt catalysts.....	158
Table 6.2. CO oxidation turnover frequency at 70 °C for Pt/STO-NCs and Pt/Al ₂ O ₃	161

Chapter I:

Metal Oxide Supported Noble Metal Catalysts

1.1: Introduction

Noble metal catalysts materials is an active area of research with the potential for high impact in applications such as chemical manufacturing, pollution control, green chemistry, liquid fuel production, and power generation[2-4], e.g. Platinum, Palladium and Rhodium based catalysts are the most popular catalysts currently used in automobile exhaust cleanup to reduce diesel generate harmful pollutants such as nitrogen oxides (NO_x), carbon monoxide (CO), unburned hydrocarbons (HC), particulates, and sulfur oxides (SO_x). Gold catalyzed coupling reactions that result in formation of new C-C bonds are strategically important in organic synthesis. However, because of the high cost and limited availability of these metals, it is important to use as low a noble metal concentration in these catalysts as feasible. This is accomplished by keeping the active metals at a high degree of dispersion. Thus these metals are usually used as catalysts in the form of nanoparticles with diameter in the range of 1-100 nm The systems have a high surface to volume ratio which allows these catalyst to be more reactive for same the weight.

Catalytic supports are primarily selected for their high surface area or thermal, chemical, and mechanical stability, but the support can also affect the selectivity and reactivity of the catalyst.[5-7] Understanding the impact of the substrate on nanoparticle growth is also desired, as it has been proven by many early catalytic studies that support materials play a very important role in the selectivity and reactivity of the catalyst. Change of the support can alter the chemisorption and catalytic behavior dramatically.[8-11] Metal oxides comprise a diverse and fascinating class of materials that contain metal elements and oxygen anion in the oxidation state of -2 . The properties of these materials can cover the entire range of conductor (or even

superconductor), semiconductor and insulator. When used as catalysts supports, as strong interaction will occur between catalysts and metal oxide, thus their surfaces play crucial roles which can alter catalytic behavior of supported catalysts obviously. For catalyst would be able to take advantage of the different exposed faces to show different selectivity and reactivity.[12] Thus one of intriguing aspects of metal oxide support effects is the potential to stabilize and optimize the selectivity and reactivity of a catalyst with the exposed faces carefully controlled.[13] Many fundamental works have been done to explain the interaction of catalysts and supports. The general role of these supports proposed based on these studies includes sites at the metal-support interface,[14] surface structure sensitivities,[15] and strong metal-support interactions.[16, 17] The latter includes concepts such as intermetallic bond formation and charge transfer,[18] diffusion of metal species between support and catalyst,[5, 19] geometric decoration,[20-22] and other electronic effects.[23] These insights have been gained from studies on model systems, largely on single crystals. However, catalysts dispersed on single-crystal metal oxides supports have very low loading due to extremely low surface to volume ratio. There have been many attempts to avoid this by creating high surface area nanostructured metal oxide supports with specific exposed surfaces.[24, 25]

Among all different types of catalytic supports, perovskites are mainly attractive due to their lower cost for commercial reasons, but more importantly because of their thermal stability as well as great flexibility in their composition and structure, offering tremendous tailoring capability for the development of future heterogeneous catalysts. The first mineral perovskite (CaTiO_3) was discovered in the Ural Mountains, Russia, by Gustav Rose, in 1839, which was name in tribute to the Russian mineralogist Lev Aleksevich von Perovski. Currently the name

“perovskite” is also commonly employed to name a specific group of oxides with general formula ABY_3 and similar crystal structure, where “A” and “B” are cations and “Y” is an anion. The traditional view of the perovskite lattice is that it consists of small B cations within oxygen octahedra, and larger A cations which are six fold coordinated by oxygen. The structure of an ideal cubic perovskite is shown in Figure 1.1, where the A cations are shown at the corners of the cube, and the B cation at the center with oxygen ions in the face-centered positions. The space group for cubic perovskites is $Pm\bar{3}m$ (#221)[26]; the equivalent positions of the atoms are detailed in Table 1.1. Compared to other oxide families such as pyrochlore, perovskite related compounds can be synthesized with a wide variety of combinations of chemical elements, and in addition the structure is highly tolerant to vacancy formation. For all possible combinations of the cation metal elements on the lattice site, there are total 96 combinations are available. In these oxides with formula ABO_3 , the A site can be filled either by A^+ (Na, K), A^{2+} (Ca, Sr, Ba) or A^{3+} (Fe, La, Gd), and the B site can be occupied either by B^{5+} (Nb, W), B^{4+} (Ce, Zr, Ti) or B^{3+} (Mn, Fe, Co, Ga), Figure 1.2. As a result of the combination of different ions, the materials may show insulating, semiconducting, ionic conducting and superconducting behavior being useful for technological applications in sensor devices, refractories, electronic components, solid oxide fuel cells (SOFC) and so on[27-29]. More important, changing of these ions will alter surface physics and chemical properties dramatically which will change catalytic performance when these materials are used as either catalysts or catalyst supports.

One area of particular interest in this work is heterogeneous catalysis of perovskite metal oxide supported platinum metal nanoparticles, for which we selected strontium titanate and Barium titanate as a model substrates. Atomic level controlling over the size, shapes, orientations,

and surface structures and even active sites of deposited catalysts will allow for optimizing catalytic performance. As almost all industry chemical processes involve catalysis, the ability to manufacture a catalyst with optimized performance would be invaluable. So one important goal of this work, therefore, is to apply different strategies to accomplish controlling over desired properties of heterogeneous catalysis.

1.2: Heterogeneous catalyst preparation

1.2.1 Traditional methods for preparation of catalytic material

Catalytic materials, either homogenous or heterogeneous, can exist in various forms and their preparation involves different protocols with a multitude of possible preparation schemes.[30-32] The properties of a good catalyst for academy or industrial can be divided into two categories: (1) properties which determine the number of active sites accessible by reactants will directly determine catalytic activity and selectivity, for which porosity, surface area, exposed surface, chemical composition and local micro-structure are important; and (2) properties which ensure their successful implementation into the catalytic reaction process, for this thermal and mechanical stability of catalyst particles counts. Thus to achieve the goal of designing a good catalyst with a high stability, reactivity and selectivity for either academy or commercial purpose, a preparative method is to synthesize catalysts with sufficiently high surface area, selected exposed surface, suitable mechanical strength and high thermal stability. For heterogeneous catalysts, the catalytic properties are strongly affected by every step of the preparation together with raw material it used.

One of most frequently applied scientific approach to the preparation of catalysts is precipitation which was introduced by Marcilly.[33] The formation of precipitation from a homogeneous liquid phase usually occurs in three processes: supersaturation of specific particles for nucleation, nucleation of the particles and growth or agglomeration of formed nuclei, which are either caused by physical transformations due to change of temperature, pressure of solvent, or even more is determined by chemical processes. Other frequently used production method for supported catalysts synthesis is so-called impregnation methods, which accomplished by pore filling of a carrier with an active phase. The object of this method is to fill pores of the support with a solution of the catalyst precursor, e.g., a metal salt of sufficient concentration to achieve the desired loading. Under equilibrium conditions, the amount of catalysts introduced onto the support are determined by the binding of the catalysts precursor onto the support surfaces, which depends on the equilibrium concentration of the impregnating solution, the porous volume of the carrier, and the adsorption isotherm. The maximum loading is limited by the solubility of the precursor in the solution. On the other hand, increasing the weight loading requires higher concentrations, however, of which may cause support disruption and substitution of ions into the support lattice.[34] If even higher loadings with active phases are required, it is mostly necessary to repeat the impregnation after drying or calcination of the intermediate few times. Besides these two synthesis techniques, there are also plenty of other methods such as microemulsions, surface capping, ion-exchange etc, all of which are effective in producing nanostructure catalysts. Unfortunately most of these methods lack atomic-level control over the catalyst composition, surface structure and often yield relatively large metal clusters with a broad size distribution. New synthesis techniques with atomic level control are desired for next generation catalyst synthesis.

1.2.2 New application of atomic layer deposition for catalyst synthesis

Atomic Layer Deposition (ALD) is a thin film deposition technique which applies self-limiting or sequentially self-terminating films via chemical vapor deposition (CVD). The concept was first published with the name “Molecular Layering” (ML) in the early 1960s by Prof. S.I. Kol'tsov from the Leningrad Technological Institute (LTI). However, it was the work of Dr. Tuomo Suntola and coworkers in Finland in mid-1970s for ZnS film deposition which made the scientific idea become a true thin film deposition technology and took that into an industrial use and worldwide awareness. The motivation behind developing ALD was the desire to make the thin film electroluminescent (TFEL) flat panel displays[35-37], which demands high dielectric strength over a large area of deposited material since an electric fields in the range of megavolts per centimeters will be applied across polycrystalline and deposited film. For the magic of such technique, ALD was successful in meeting the requirements with low pinhole density and high uniformity over the large-area substrates and since then it has been employed in TFEL production since the early 1980s.[37, 38] In addition to thin film deposition on flat substrates, ALD has also been developed and used in surface processing of porous materials for heterogeneous catalysts application, e.g. chemical modification of high surface area silica and alumina powders[39-41], nanoporous silicon layers[42] and alumina membranes[43, 44] have been processed.

As implied above, ALD is a chemical gas phase thin film deposition method which deposits materials in a layer-by-layer fashion. The Layers are formed during reaction cycles by alternately pulsing precursors or reactants and purging with inert gas in between each pulse. Similar to CVD, the reaction is between binary reactions of two reactants A and B which is

usually denoted simplistically as $A + B \rightarrow \text{Product}$. On the other hand, ALD is also distinct from CVD in several aspects, e.g. during ALD process the reactant source is pulsed into the reactor separately, one at a time, with an inert gas purging (e.g. high purity nitrogen, argon) periods applied before next reactant exposure. In the majority case of ALD that film deposition operated in a cyclic manner, one full cycle usually consists of four steps: 1) exposure of the first precursor, 2) 1st inert gas purging, 4) exposure of the second reagent, and 5) 2nd inert gas purging. By using this exposure strategy, each precursor pulsing step will saturate at surface with a monomolecular layer of that precursor in an ideal ALD process, which results in a unique self-limiting film growth mechanism with a number of advantageous features comparing to CVD, such as excellent conformity, uniformity and accurate film thickness control. Depending on the process and deposited materials, one cycle deposition will roughly yield sub-angstrom growth in thicknesses. In order to obtain the desired film thickness, certain number of ALD cycles need to be repeated as necessary.

Here, we use growth of Al_2O_3 from trimethylaluminum ($\text{Al}(\text{CH}_3)_3$, TMA) and H_2O as an example to schematically illustrate the ALD process, Figure 1.3. When TMA was pulsed onto the surface terminated with functional groups (e.g. hydroxyl group for this case), the precursor molecules react with surface by ligands exchanging with surface hydroxyl groups releasing some byproducts (e.g. hydrocarbons C_xH_y) formed from desorbed ligands, Figure 1.3a. The byproduct is then purged away by a sufficient long inert gas purging before next reagent dosing. The water which works as 2nd reagent is then exposure to the new formed surface and consequentially a new functional hydroxyl layers will form, Figure 1.3b. After a 2nd inert gas purge, the surface is recovered same as initial surface and such procedures can be simply repeated to deposit alumina

with desired thickness. The actual reaction taking place under TMA exposure step depends largely on the presence or the absence of reactive functional group on the surface of the growing film. In the case of oxides, for example, functional surface hydroxyls often terminate the surface after exposure to water. If there are no or insufficient functional groups on the surface, the incoming TMA molecule can only or mainly through chemisorb, either intactly or dissociatively. As a consequence of a finite number of the reaction or chemisorption sites on the surface, only a small portion of the precursor can firmly bond to the surface. And for this situation ALD will not ideally form film which is same as an ideal case we discussed above.

For most cases, the formation of a film is not always occur in the first few ALD cycles as the process strongly depends on surface condition and how efficiently a monolayer of precursor will adsorb on the surface. The efficiency of ALD in the early stages will be related to surface condition, dosing time, reactivity of the precursor, and the temperature. These factors combine to give a growth regime where an incomplete film forms and eventually coalesces of the incomplete film leading to the steady state growth regime as the number of cycles increase. ALD at the early stages, before formation of a complete film, has also been studied and consequently extend the capabilities of the technique for metal or metal nanoparticles synthesis.[45, 46] The key prospect related to this project is the formation of nanoparticles due to the incomplete coalescence of a film for the case of platinum. Metal ALD chemistries are particularly prone to the formation of nanoparticles, e.g. Smeds et al. obtained high dispersed Ni nanoparticles on Al_2O_3 using several cycles of ALD synthesis.[47] Backmen et al. also showed uniform cobalt nanoparticle on SiO_2 deposited using ALD.[48] A detailed understanding of the nucleation, growth and coalescence of the nanoparticles is needed at the nanometer length scale in order to systematically pursue the

technological application of such nanoparticles from ALD. A lot of chemistry, morphology and surface science studies have been performed on these materials which indicates that ALD could allow one to control the particle size[49], particle density[50] and composition[51] on an atomic level. These features are critical to developing ALD processes with the finest control over particle size, dispersion and loading for catalyst synthesis.

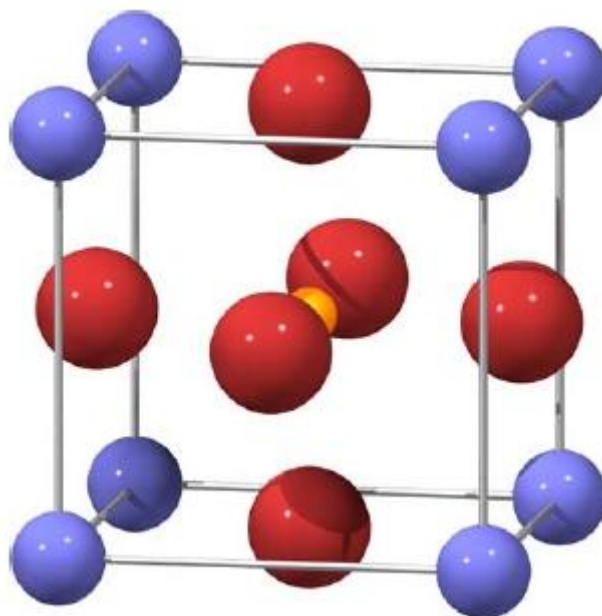


Figure 1.1. Cubic perovskite unit cell. Blue spheres represent the A cations, yellow spheres represent the B cations, and red spheres represent oxygen anions forming an octahedra.

Table 1.1. Atomic positions in cubic perovskites

Site	Location	Co-ordinates
A cation	(2a)	(0,0,0)
B cation	(2a)	(0.5,0.5,0.5)
O anion	(6b)	(0.5,0.5,0) (0.5,0,0.5) (0,0.5,0.5)

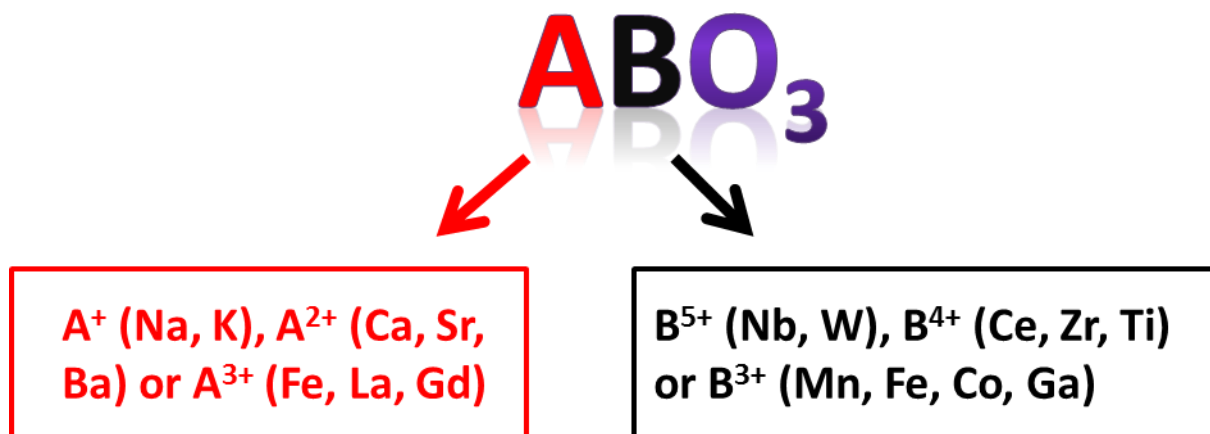


Figure 1.2. Schematic of compositions a pervoskite structure

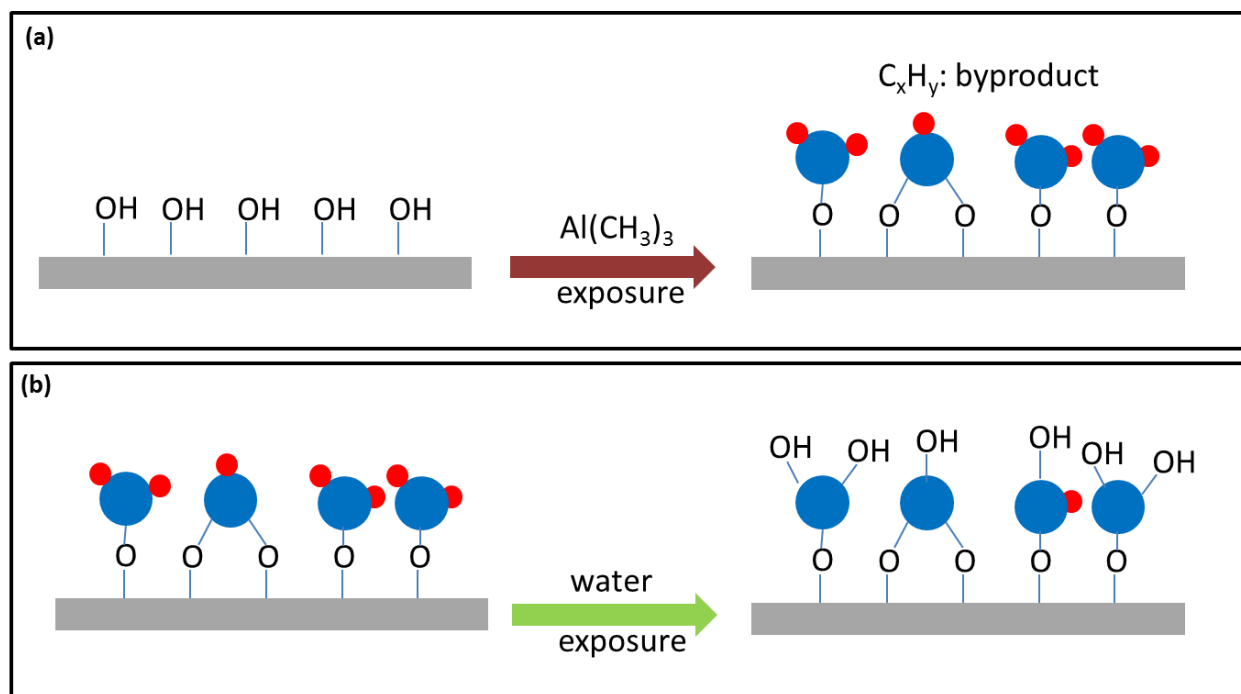


Figure 1.3. An ALD thin film deposition cycle shown schematically with the TMA- H_2O process as an example.

Chapter II:

**Synthesis Approach of High Surface Area Catalytic Support
with Specific Exposed Surfaces**

2.1: Introduction

The properties of catalyst support surface are decisive for its catalytic application. On the one hand, the catalytic activity and selectivity performance of support surface itself depends directly on the kind and concentration of the different active sites. On the other, the support surface affects the formation of definite structures of the active phase of supported catalysts and further affects the catalytic activity and selectivity performance of the catalyst. Other important characteristics of support surface, such as its adsorption ability and its pigmentation, also depend on the surface properties. To fundamental understanding these, literature studies have been done on both single crystals and nanomaterial powder as a catalyst support, although the latter is the only realistic industrial option for catalysts. However, an atomic level structure and surface science studies of model catalyst supported on single crystals substrates will help provide insight of correlation of structure-surface-chemistry-performance between substrates and catalysts. Thus we employ both single crystal and nanomaterial powder as catalyst substrates in this project. In this chapter we will introduce method for chemical synthesis approach of nanostructured catalytic support. Detail discussion of catalysts supported on single crystal substrates will be saved for next chapter. As single crystal substrates can be easily acquired from commercial substrates vendors such as MTI Corp. (Richmond, California), Crystal GmbH (Berlin), and CrysTec GmbH (Berlin). Usually purchased sample are with very similar quality and properties such as exposed orientation, miscut angle and doping level can all be customized from these vendors. Thus we will only spend few sentences in Chapter III to introduce such type of material growth with an example of SrTiO_3 single crystal growth using modified Verneuil method.[52] A lot of nanomaterial powder substrates can also accessed by commercial purchase but most of which are usually with irregular shape, undetermined termination and stoichiometry, large size

distribution etc. A novel synthesis method that can synthesize nanoparticles with regular shape, controllable exposed surface, narrowed size distribution is necessary and will be discussed in details here.

The microemulsion-based synthesis is an excellent way to make metals, metal salts and metal oxides, e.g. about 30 years ago Boutonnet et al. showed that metallic nanoparticles could be obtained by simple mixing of two water-in-oil microemulsions, one containing a salt or a complex of the metal and the other containing a reducing agent, such as sodium borohydride or hydrazine.[53] Generally, there are three major microemulsion structures in a mixture of water, oil, and surfactant: normal micelle, reverse micelle, and the lamellar liquid crystal structures. For instance, oleic acid and oleate species can form lamellar liquid crystal structures where the hydrophilic oxygen-terminated groups of the surfactants align across the water phase while the hydrophobic hydrocarbon-terminated groups align across the oil phase.[54] When the mole fraction of the components change, the lamellar liquid crystal structure will convert to a normal micelle structure at low oleic acid concentration or reverse micelle structure at high oleic acid concentration. Numerous studies have exploited normal or reverse micelles for the synthesis of nanoparticles.[55-57]

While the synthetic conditions relies on different microemulsion structures have in many cases now become quite refined, in many examples the details of exactly why these differences in synthetic condition change the nanoparticle shape are often much less clear. In normal or reverse micelles the rate limiting step is diffusion in the liquid phase which, owing to the tortuosity of the structure, is slow. Atoms arriving from the solvent at the nucleation site add at the closest available site, which leads to irregular shapes. In contrast in a lamellar microemulsion

the quasi-two-dimensional diffusion to the nucleation site is fast so growth is limited by conventional nucleation of new steps on the surface leading to a standard kinetic-Wulff construction[58]. In this work, two types of Strontium Titanate Nanocuboids (STO-NCs) were synthesized by Northwestern Researcher using a hydrothermal method based on microemulsion-based synthesis. STO-NCs synthesized from a lamellar structure will be discussed in details here. As reported by Hu, L. H. et al, the microemulsion plays a major role in dictating the kinetics of the growth which in turn determines the overall shape and the findings show that the cuboid shape of as-prepared SrTiO_3 nanocrystals is a consequence of the elastic constraints of the lamellar liquid crystal structure established during the hydrothermal process.[59]

2.2: STO-NCs synthesis from lamella micro-emulsion

2.2.1 STO nanomaterials synthesis from different microemulsion structures

Different microemulsion structure can be form by changing the oleic acid concentration in the solution. With a low oleic acid concentration, e.g. using 2mL oleic acid with other chemicals amount used same as for STO-NCs synthesis, the solution falls in the region of the phase diagram where normal micelles will occur. The as-prepared SrTiO_3 crystallites from these solutions are irregular, round and trifurcate nanoparticles. At higher concentration of 15mL oleic acid the phase diagram will from reverse-micelles. Small, curved STO nanorods form suggesting cylindrical water in oil micelles are formed with a diameter of 6~8nm. For the intermediate concentration of 7.5mL oleic acid a lamellar liquid crystal will occur.

STO-NCs in this Chapter were synthesized from the lamellar structure microemulsion which is formed following a sol-precipitation-hydrothermal treatment procedure[60, 61]: 1.5 mmol of titanium butoxide ($\text{Ti}(\text{OBu})_4$, 99% Alfa Aesar Company) was added to 52.5 mL of

ethanol and 7.5 mL of oleic acid to form solution A, 1.5 mmol of strontium acetate ($\text{Sr}(\text{Ac})_2$, 99% Alfa Aesar Company) in 15 mL of water was used to form solution B, and 1.2 g of NaOH in 6 mL of water was used to form solution C. Solutions B and C were successively added to solution A and mixed while stirring for a few of minutes with a pH of 13–14, and the resultant solution was sealed in a 125 mL autoclave and then heated at 160 °C for 8 h. All chemicals were of analytical grade and were used as received without further purification. Distilled water without CO_2 was used throughout.

2.2.2 Electron Microscopy

The size and morphology of the nanocrystals were determined by a HD2300 transmission electron microscope (TEM) at 200 kV, and a high-resolution electron microscopy (HREM) and scanning transmission electron microscopy (STEM) using a JEOL 2100F at 200 kV. For High Angular Annual Dark Field-Scanning Transmission Electron Microscopy (HAADF-STEM) imaging, the inner and outer angles of the detector are 124 mRad and 268 mRad. All TEM samples were prepared by placing several drops of a cyclohexane dispersion of the as-prepared materials on the surface of a carbon film supported on a copper grid, Figure 2.1. For Cryo-EM analysis done by Linhua Hu, a total of 5 μL of the STO synthesis solution was transferred to a freshly glow discharged 300-mesh copper grid covered with a thin layer of carbon film. The grid was then blotted and plunged into a reservoir of liquid ethane at its melting temperature (~ 90 K) at a speed of about 2–4 m/s. All the above procedures were done in a Vitrobot (FEI). Then the grid was transferred to liquid nitrogen, mounted in a cold stage, and rapidly introduced into a JEOL 1230 transmission electron microscope operated at 100 kV.

2.3: Results and discussions

2.3.1 Morphology of as-synthesized STO-NCs

The as-synthesized STO-NCs following the recipe above have a well-defined, thermodynamically stable shape with primarily (100) type surfaces exposed, which are also non-porous, single-crystalline with average sizes are approximately to be 20 nm, Figure 2.2. To determine their true 3D morphology, based on the fact that these nanocuboids only have (100) facets, we tilted by 10-30° during HAADF-STEM operation to measure the projected edge-lengths and the angles between them, and then did a standard least-squares inversion based on the solver analysis method to determine the true length, width, and thickness[62], Figure 2.3.

If we assume A, B, C is the real dimension parameter of nanocuboids (length, width, thickness) and theta, phi is angle for first tilt and second tilt of these cuboids from (100) zone axils. Thus, the matrix of measured dimension from HAADF images after these two tilts will be:

$$M' = \varphi\theta M =$$

$$\begin{pmatrix} 1 & 0 & 0 \\ 0 & \cos\varphi & \sin\varphi \\ 0 & -\sin\varphi & \cos\varphi \end{pmatrix} \begin{pmatrix} \cos\theta & 0 & -\sin\theta \\ 0 & 1 & 0 \\ \sin\theta & 0 & \cos\theta \end{pmatrix} \begin{pmatrix} x \\ y \\ z \end{pmatrix} = \begin{pmatrix} \cos\theta & 0 & -\sin\theta \\ \sin\varphi\sin\theta & \cos\varphi & \sin\varphi\cos\theta \\ \cos\varphi\sin\theta & -\sin\varphi & \cos\varphi\cos\theta \end{pmatrix} \begin{pmatrix} x \\ y \\ z \end{pmatrix}$$

We assume a, b, c, alpha, beta, gamma is experimental measured value from HAADF:

$$a = A\cos\theta \quad (1)$$

$$b = B\sqrt{(\sin\varphi\sin\theta)^2 + (\cos\varphi)^2} \quad (2)$$

$$c = C\sqrt{(\sin\varphi\sin\theta)^2 + (\sin\varphi)^2} \quad (3)$$

$$\cos\alpha = \sin\varphi\sin\theta / \sqrt{(\sin\varphi\sin\theta)^2 + (\cos\varphi)^2} \quad (4)$$

$$\cos\beta = \sin\phi \cos\theta \left(\frac{(\sin\theta)^2 - 1}{\sqrt{(\sin\phi \sin\theta)^2 + (\cos\phi)^2}} \right) \sqrt{(\cos\phi \sin\theta)^2 + (\sin\phi)^2} \quad (5)$$

$$\cos\gamma = \cos\phi \sin\theta / \sqrt{(\cos\phi \sin\theta)^2 + (\sin\phi)^2} \quad (6)$$

We define the fitting error as,

$$\text{Error} = \sqrt{(a-a_0)^2 + (b-b_0)^2 + (c-c_0)^2 + (\cos\gamma - \cos\gamma_0)^2 + (\cos\alpha - \cos\alpha_0)^2} \quad (7)$$

Set: $0 \leq \phi \leq 90^\circ$; $0 \leq \theta \leq 90^\circ$; $0 \leq A \leq 22 \text{ nm}$; $0 \leq B \leq 22 \text{ nm}$; $0 \leq C \leq 22 \text{ nm}$; $\cos\gamma = \cos\gamma_0$; $\cos\alpha = \cos\alpha_0$; With Error is minimization, all real three dimension information can be acquired and the results is summarized in Table 2.1. This analysis confirmed the formation of a cuboid shape with shorts edge approximate $\sim 8 \text{ nm}$ and longest edge around $\sim 20 \text{ nm}$.

Additionally to determine 3D morphology, the surface termination is also carefully characterized. As STO are stacked with SrO and TiO_2 in $\langle 100 \rangle$ direction, thus it can be terminated with either termination. Here we employ the HREM to solve the structure. A typical STO-NCs synthesized with recipe described above imaged along the $[110]$ direction is shown in Fig. 2.4(b) which is taken by Yuyuan Lin. A higher magnification image of this nanocuboid with the surface layer (the top layer) clearly resolved is shown in Fig. 2.4(a). The contrast in the bulk region can be directly interpreted: the bright spots are atoms. This is consistent with previous High Resolution Electron Microscopy (HREM) study of SrTiO_3 single crystals under similar imaging conditions (small Cs and small overfocus).[63] Figure 2.4(d) shows a simulated HREM image from a DFT relaxed SrO (1x1) surface, which matches the experimental image. Note that other surface structures can show the same surface periodicity, but the contrast is drastically different from the experimental image. The surface of the nanocuboids synthesized by the oleic acid method has a 1x1 SrO termination.

2.3.2 Mechanism of formation of STO-NCs beyond synthesis

After revealed the morphology of the as-synthesized STO-NCs above, it is necessary for us to clear the formation mechanism of these nanocuboids. To understand this, two coupled but different questions need to solve: what are the chemical reactions taking place during the formation of the SrTiO₃ and how does the microemulsion structure couple to the kinetics of growth?

The shape of a free nanoparticle is usually determined by the thermodynamic Wulff construction [64] which depends upon focused on energy minimization of total surface energy. The particle formed in a lamellar structure is not following such construction instead a kinetic process will be more precisely describing the situation. Turning now to kinetic Wulff construction[58], the kinetics can be described by a standard differential form:

$$\partial h(\hat{n}, t) / \partial t = v(\hat{n}, \frac{\Delta\mu(t)}{kT}) \quad (8)$$

Where $h(\hat{n}, t)$ is the length from some arbitrary origin to a facet whose normal is given by \hat{n} , t is time, $\Delta\mu(t)$ is the chemical potential difference between Sr and Ti in solid SrTiO₃ and the water phase of the microemulsion as a function of time, T is the temperature, k is Boltzmann's constant, and $v(\hat{n}, \frac{\Delta\mu(t)}{kT})$ is the growth velocity for the facet. Note that the change in chemical potential implicitly depends upon the Sr and Ti concentrations in the fluid phase which is related to the activity according to the thermodynamics as the following,

$$\mu_i = \mu_0 + RT \ln a_i \quad (9)$$

And the activity (a_i) here is usually a strong function of the concentration which will be described by Henry's law or Raoult's law,

$$a_i = f(c_i) \quad (10)$$

Thus the chemical potential difference can be described as,

$$\Delta\mu = \mu_i - \mu_0 = RT \ln\left(\frac{f(c)}{f(c_0)}\right) \quad (11)$$

which may be inhomogeneous and vary with time as species diffuse through the micelle/reverse micelle/lamellar structures.

If the nucleation of a new step on a surface is slow (rate-limiting) and the concentration of reactants is homogeneous, the growth velocity can be written via a face-dependent term $w(\hat{n})$ leading to the standard Frank or kinetic-Wulff construction solution for the final shape [18, 65, 66]:

$$\partial h(\hat{n}, t \rightarrow \infty) / \partial t = \lambda w(\hat{n}) \quad (12)$$

with λ is a constant. This is similar to the thermodynamic Wulff construction, but the external shape is now determined by the slowest growing faces. Since these tend to be those of lowest energy, for SrTiO₃ the (100) type facets will dominate the growth shape, just as they dominate the thermodynamic shape. The kinetic-Wulff form assumes that arrival of new reactants is not rate limiting, and we argue that in the two-dimensional lamellar structure this is valid. This is not the case for the micelle or reverse-micelle cases where the oleic acid structures act as barriers to diffusion. Our interpretation is that in such a case the concentration of Sr and Ti in the liquid

phase is rate limiting leading to less regular diffusion-controlled shapes as seen in many other systems.[67, 68]

Different from the (100) growth of perovskite cubes or the irregular growth in micelles/reverse micelles, STO-NCs in the lamellar liquid crystal possess a unique growth mechanism-the direction normal to the lamellar is different. The chemisorption of the oleic acid on the (100) face is relatively strong and will hinder growth, albeit it is still much smaller than the energies involved in forming SrTiO₃ so will not prevent it. More importantly, as the particles enlarge in this direction they will elastically distort the lamellar nanostructure which will lead to an increasingly large energy barrier for growth. The thickness of three water layers (3×1.1 nm) and two oil layers (2×2.3 nm) is about 7.9 nm, very similar to the average 8 nm thickness of SrTiO₃ nanocuboids. Therefore, we can infer that one water layer is broken through and SrTiO₃ forms within the adjacent two water layers and the two oil layers.

Now we move to the reactions part. The hydrothermal synthesis of perovskite SrTiO₃ nanoparticles involves soluble Ti species in the solution and mineralization with Sr species under strongly basic condition[69-71], e.g. a formation pathways of SrTiO₃ has been proposed under hydrothermal conditions which use bulk TiO₂ as reactant. Bulk TiO₂ will dissolve in the solution and form soluble Ti species which will react with Sr species to form SrTiO₃. X-ray diffraction studies as a function of different reaction time have confirmed the gradual dissolution of TiO₂ with the nucleation and growth of SrTiO₃. [71] In our case, we use the metal alkoxide Ti(OBu)₄ instead of TiO₂ as the precursor for the Ti species. Briefly, Ti(OBu)₄ is first added into oleic acid and pure ethanol to form a mix solution. The hydrolysis of Ti(OBu)₄ is limited without water. Another solution which contains the Sr precursor (strontium acetate (Sr(Ac)₂) is then added to solution previous formed mix solution, leading to the coordination of Sr²⁺ with oleic acid at the

oil–water interface[72] with the simultaneous generation of amorphous gel from the hydrolysis of $\text{Ti}(\text{OBu})_4$. Finally, NaOH in water, a third solution, is added into the above mixture raising the pH to 13–14 where the added base can deprotonate the oleic acid to establish the lamellar structure, Figure 2.5. The lamellar distance d is ~ 4.5 nm at 18 °C, which is the sum of the oil layer of oleic and water layer. As the thickness of the oil layer and water layer is ~ 3.4 nm (two layers of oleic acid with chain length of 1.7 nm) and 1.1 nm respectively, Figure 2.6. During the synthesis, the lamellar distance d will decrease for an elevated temperature, e.g. $d \sim 3.4$ nm at 160 °C. The decrease of the lamellar distance d mostly results from the bending of the more elastic long chain of the oleic acid molecule instead of water. The cuboid shape with average thickness of 8 nm is formed at this temperature.

In summary, the STO-NCs shape are proposed following the reaction scheme as (1) coordination of Sr^{2+} with oleic acid and amorphous gel in basic conditions at room temperature, (2) formation of SrTiO_3 nuclei in the water phase (water layer) and (3) growth to STO-NCs. The proposed growth of SrTiO_3 nuclei to nanocuboids is summarized in Figure 2.6.

2.3.3 Influence of covered surfactant to surface properties

For most of microemulsion based synthesis, several organic solutions may be involved which potentially left the as-synthesized materials covered with carbon species. For the synthesis in this work, oleic Acid is used as the surfactant to control crystal growth and also to provide solubility which helps to organize the small oxide crystallites into a sufficiently ordered structure to generate a regular shape. However, such surfactants are toxic and lead to impurities in the final product and hamper the application of these nanocuboids used as substrates for new material

deposition (e.g. heterogeneous catalysts). The present monolayer of oleic acid on as-synthesized STO-NCs here is usually treated as surface contamination for new material deposition. The growth of new material on these supports is proved to be affected by these species.[73, 74] As a reference one monolayer of carbonaceous layer formed through Pt precursor dehydrogenation during Pt ALD process will prevent further Pt precursor adsorption and leads saturation of the ALD reaction.[75] Thus before new materials deposition, a treatment need to be investigated for surfactant removal.

2.3.4 Surfactant removal or replacement

There are several feasible methods have been developed by chemists for the purpose of surfactant modification or removal among which ligand modification (reduction, addition, and exchange) is a well-known method for tuning the surface properties of nanoparticles, e.g. Vo et al reported a completed exchange of oleic acid on TiO₂ nanorods using acrylic acid which shows excellent stability in polar media without agglomeration.[76] A simple acetic acid immersion treatment was introduced by Jung et al to reduce ligands on Ag nanoparticles in order to improve electrical performance and thermal stability.[77] However, all these methods are usually just reduce long chain ligands or replace them with short one which left the surface still covered with certain carbon layers. In order to prepare substrates that really clean and free of ligand (carbon contamination) for ALD deposition, a more efficient way is investigated in this work for ligands removal which use ozone bath at an elevated temperature. As confirmed with x-ray photoelectron spectroscopy (XPS) analysis, ozone treatment at 200 °C can remove nearly 97% carbon, Figure 2.7. Such removal is further supported by other evidence which is related to amorphous carbon fringes generated by high energy electron beam irradiation of appeared

carbon contamination on sample surface. As shown in Figure 2.8, the amorphous carbon fringe contrast after 5 min electron beam irradiation is significantly reduced compared to sample without any treatment.



Figure 2.1. Schematic diagram shows the procedure for Pt/STO-NCs TEM sample preparation on copper TEM grids.

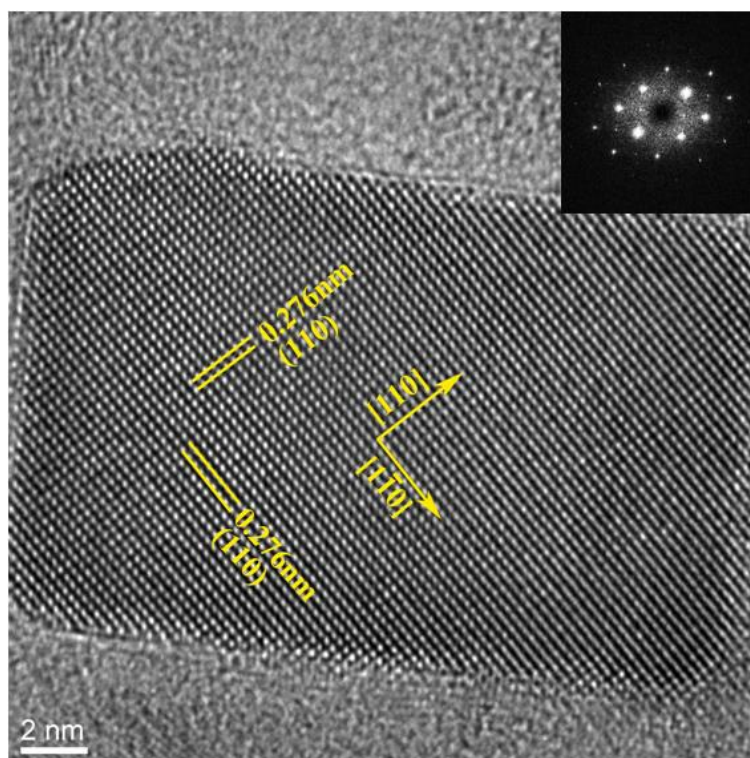


Figure 2.2. HREM image of a typical SrTiO₃ nanocuboid with a power spectrum inset.

Table 2.1. Results for the three dimensional analysis of the SrTiO₃ nanocuboids

No.	A(nm)	B(nm)	C(nm)	θ	φ	a (nm)	b (nm)	c (nm)	β	γ	Error	Ratio(A/B/C)
1	16.84	14.34	8.83	21.2°	21.2°	15.7	13.5	3.4	47°	82°	2.14E-06	1.90/1.62/1
2	19.83	11.56	9.17	16.6°	31.6°	19.0	10.0	5.0	65°	80°	8.60E-06	2.16/1.25/1
3	15.16	9.46	13.12	20.5°	19.3°	14.2	9.0	4.6	45°	83°	7.21E-06	1.60/1/1.39
4	14.24	14.56	8.99	23.1°	28.4°	13.1	13.1	4.6	54°	78°	2.34E-06	1.58/1.61/1
5	18.58	16.29	9.16	25.3°	22.4°	16.8	5.3	3.8	44°	79°	3.51E-06	2.02/1.77/1
6	14.79	15.61	9.07	17.6°	24.9°	14.1	14.3	4.0	57°	82°	5.11E-06	1.62/1.72/1
7	17.54	14.54	8.84	12.9°	21.3°	17.1	13.6	3.3	62°	85°	6.82E-06	1.98/1.64/1
8	14.73	16.96	8.20	20.6°	26.6°	13.8	15.4	3.9	57°	80°	6.39E-06	1.79/2.06/1
9	11.66	8.98	7.28	16.2°	26.7°	11.2	8.1	3.4	61°	82°	1.13E-06	1.60/1.23/1
10	19.88	13.04	7.77	16.5°	37.4°	19.1	10.6	4.9	70°	78°	7.48E-06	2.55/1.67/1
11	14.09	13.93	7.28	19.4°	27.9°	13.3	12.5	3.6	58°	80°	5.83E-06	1.93/1.91/1
12	13.40	13.69	8.05	17.2°	25.2°	12.8	12.5	3.6	58°	82°	2.93E-06	1.66/1.70/1

The experimentally measured lengths were a, b, c, and the projected angles γ between a and b as well as β between a and c. A least-squares fit was performed to obtain the true length, width and thickness of the nanocuboids A,B,C, as well as the two tilt angles θ & φ , with *a-priori* information that the nanoparticles were cuboids. The error in the table is the root mean square (RMS) error of the fit to a, b and c as well as the cosines of the angles.

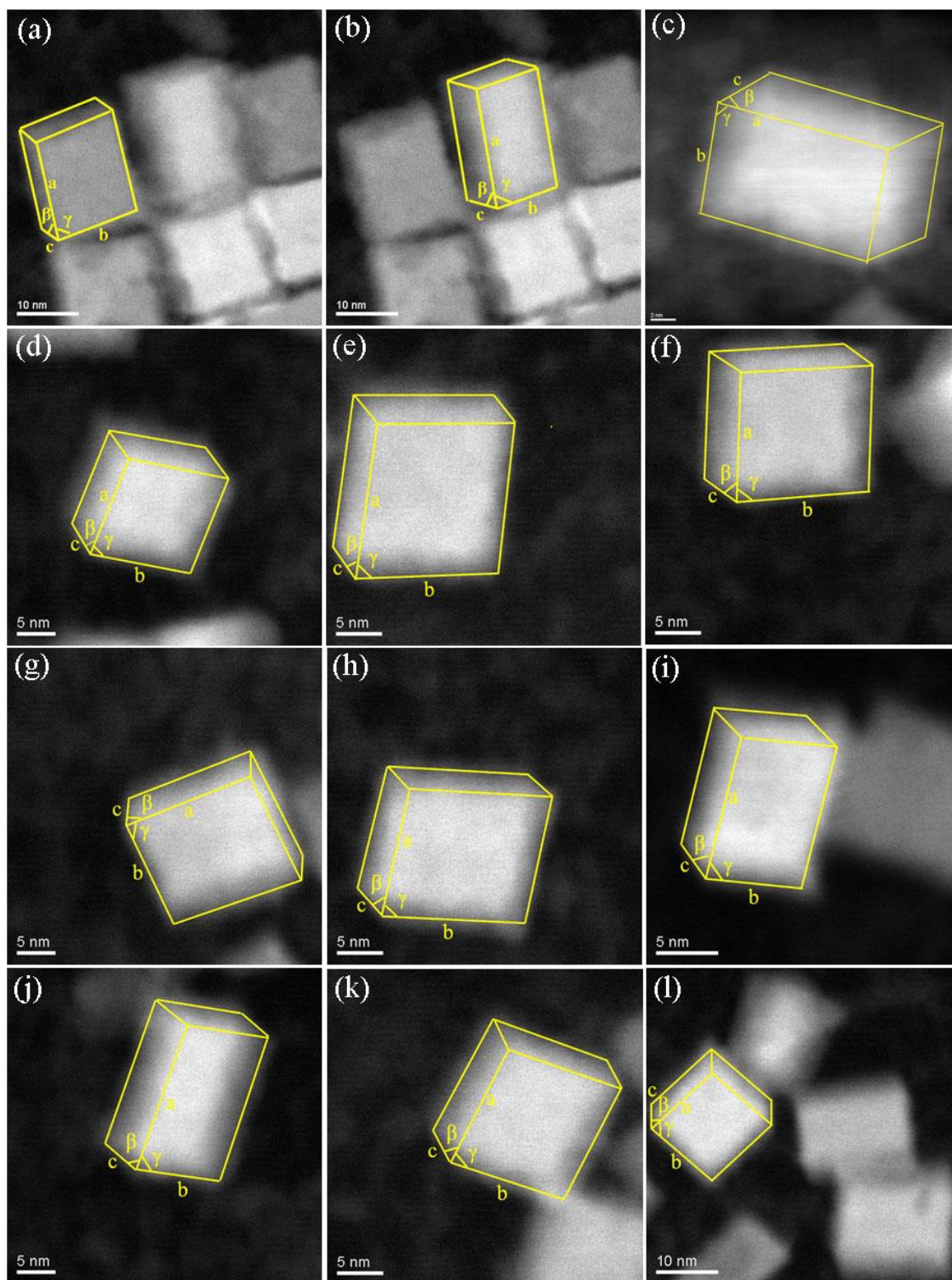


Figure 2.3. HAADF images of different SrTiO₃ nanocuboids. (a~l) are the nanocuboids 1~12 in Table 2.1

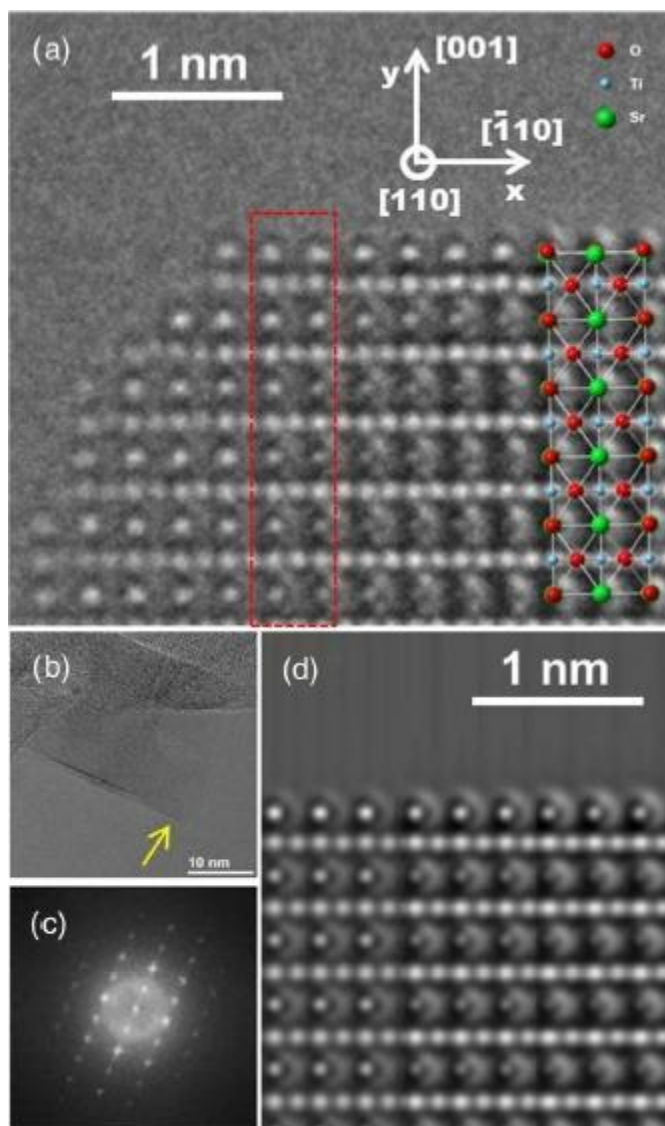


Figure 2.4. TEM images of STO-NCs with oleic acid synthesis. (a) Experimental HREM image of STO-NC along [110], where the bright spots can be interpreted as atoms. (b) Low magnification image of (a). (c) FFT image of (b). (d) Simulated HREM image of (a). In (a) the sample thickness and defocus are increasing from left to right. Therefore, (d) is generated using 3 images simulated with continual changing defocus and thickness, increasing from left to right.[1]

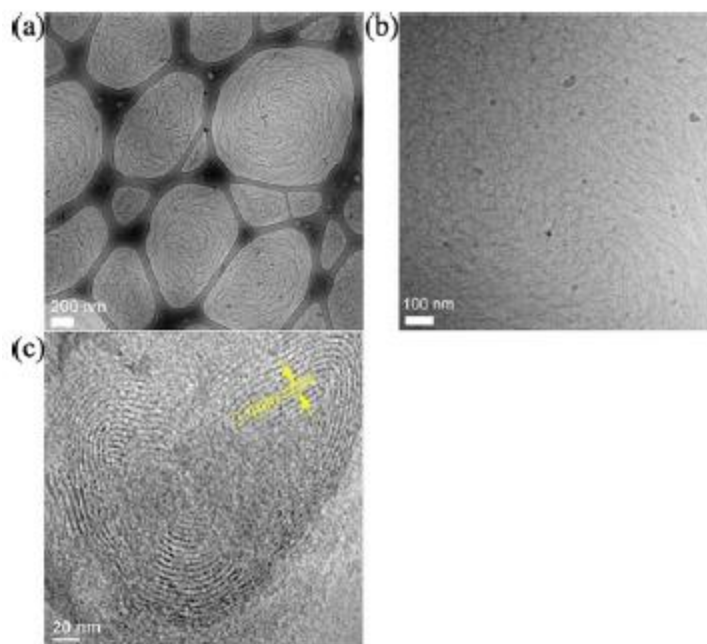


Figure 2.5. Direct observation of lamellar structure of oleic acid. (a,b) cryo-EM image of STO-NCs dispersed into oleic acid. (c) negative staining TEM image, showing the average 3.4 nm thickness of the double layer of oleic acid without water.

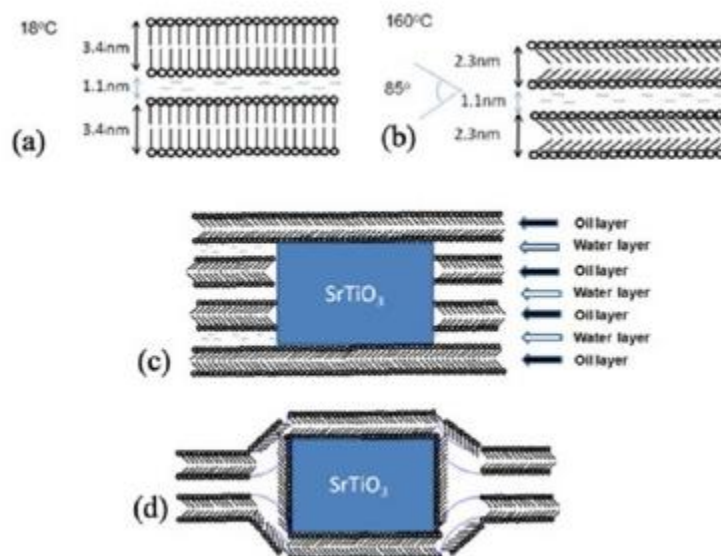


Figure 2.6. Schematic figure of the lamellar structure of oleic acid at different temperatures: (a) 18 °C, (b) 160 °C. (c,d) STO-NCs form three layers of water and two layers of oil, total thickness 7.9 nm, very similar to the 8 nm thickness of the synthesized STO-NCs. The reaction process is (1) coordination of Sr^{2+} with oleic acid and amorphous gel in basic condition at room temperature, (2) formation of SrTiO_3 nuclei in the water phase (water layer), and (3) growth to STO-NCs(blue color).

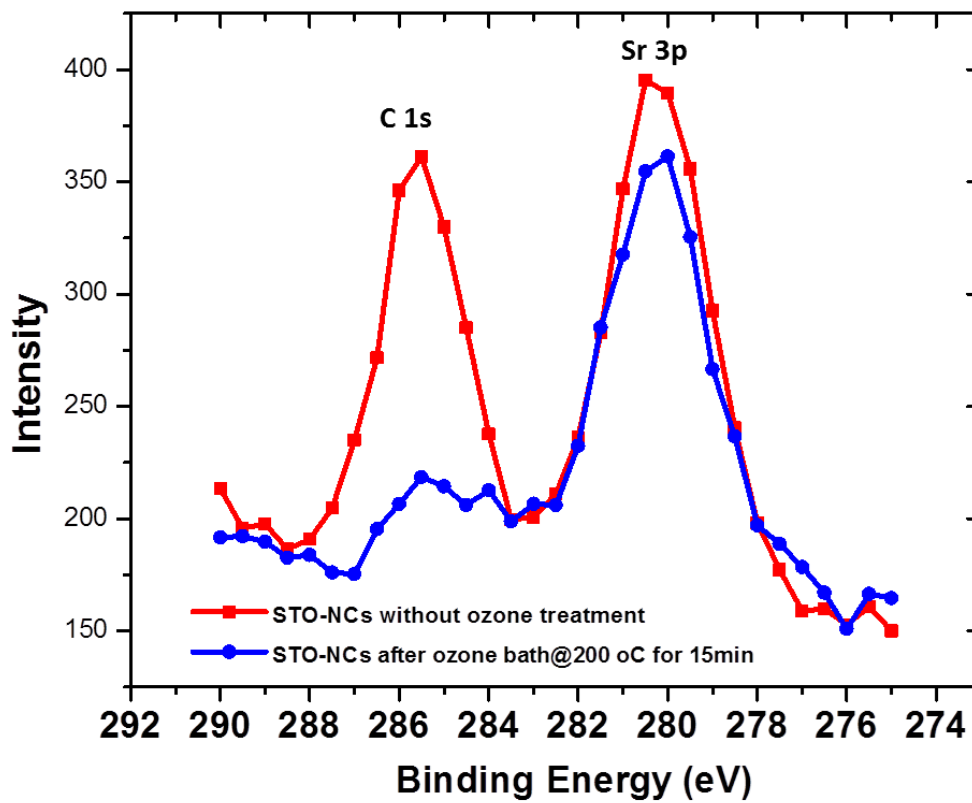


Figure 2.7. X-ray photoelectron spectroscopy (XPS) studies shows the removal of carbon species from STO-NCs after 15 min ozone bath at 200 °C.

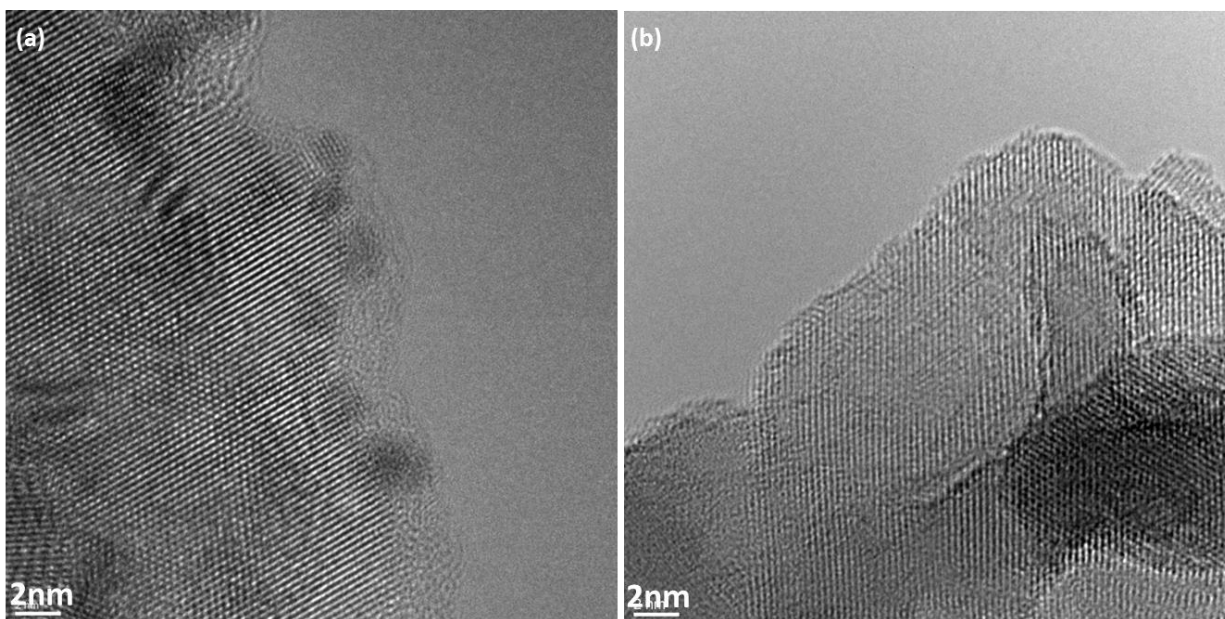


Figure 2.8. Amorphous carbon fringes generated by electron beam irradiation shows the contamination level of the sample (a) STO-NCs without ozone treatment shows clear amorphous fringes after 5 min beam irradiation (b) STO-NCs with ozone bath for 15 min at 200 °C didn't show any evidence of contamination after 5 min beam irradiation.

Chapter III:

**ALD Synthesis of Platinum Nanoparticles on Single-crystal
SrTiO₃**

3.1: Introduction

Fundamental understanding atomic layer deposition (ALD) of new materials on single crystal substrates will benefit developing and optimizing such technique for either thinnest and finest films or uniformly dispersed and ultrafine nanoparticles synthesis. Especially when ALD has become one of the most versatile and widely implemented techniques for either obtaining atomically smooth conformal thin films[78, 79] or atomic level controlled nanoparticle[13, 49] of inorganic and organic materials in an energy-efficient and environmentally friendly manner.[80-83] However, unlike ALD deposition of nanoparticles on nanostructured substrates for catalytic[13, 46, 84] and sensing[85, 86] application, initialize deposition on single crystal, e.g. single crystal strontium titanate (SC-STO), single crystal silicon, for electronic device via ALD is usually difficult. To date, rare work has described initial ALD deposition on single crystal materials. Developing research of ALD on SC-STO is worth as its broad range of technology application including dynamic random access memory[87, 88], field emission transistor[89, 90], modeling study of catalyst (e.g. photocatalytic water splitting[91-93]) and ferroelectric devices[94, 95]. More important, ALD deposited metal nanoparticles on SC-STO establishes a possible way to study and understanding structure-surface-chemistry relationship that relevant to heterogeneous catalysis.

On single crystal substrates, precursor-surface reaction is low. As single-crystal material usually with extreme low surface area comparing to nanostructured material with same mass, e.g. the surface area ratio between 1g SC-STO with a cubic shape ($\sim 2 \text{ cm}^2$) and BET surface area of 1g STO-NCs with a length of 60 nm ($\sim 20 \text{ m}^2$) [49] is about 10^{-5} . Carbon contamination yielded during sample transfer or sample processing in atmosphere or low vacuum environment will form carbonaceous layers which can further lower limited exposed surface and reduce effective

nucleation sites on the single crystal surface, e.g. 1 ng grapheme will generated 5×10^3 ML thick carbon layers on single crystal STO wafer with 2 cm^2 surface area but only form 0.05 ML on STO-NCs with surface of 20 m^2 . The carbon contamination will prevent precursor adsorption during ALD deposition.[75] Even precursor are successfully deposited, it might located on contamination layer instead of substrates. Thus direct ALD synthesis on SC-STO covered with carbon contamination is usually not successful within few cycles of deposition. Surface enhancement such as contamination elimination and surface hydroxyls group enriching is desired.

Standard cleaning procedures used by surface scientist to prepare clean and well order surfaces is usually started with ion sputtering and followed by annealing and a proper gas assistance may applied. Such treatment was reported effective for contaminations removal elsewhere.[96, 97] Ion sputtering, however, produces undesirable radiation damage at the surface and points defect even remaining after annealing.[98] Moreover, such techniques can't improve surface hydroxyl groups contrarily annealing process, which can easily target $\sim 700 \text{ }^\circ\text{C}$ for metal oxide[99, 100], will dramatically lower these species through thermal desorption ($< 400 \text{ }^\circ\text{C}$ [101, 102]). A treatment that can increase surface hydroxyl group but also efficiently to remove carbon contamination is imperative.

Wet chemical etching is one of key techniques for the manufacture in modern device technology, e.g. either KOH or Buffered $\text{NH}_4\text{F-HF}$ (BHF) etched Si will provide atomic flat and contamination free substrates for further microfabrication.[103] During the etching, hydroxyl ions OH^- from the etching solution play a central role. They substitute the surface-terminating hydrogen's and catalyse the removal of the surface atoms by weakening their back bonds. The evolution of such etching process is expected to be strongly correlated to the amount of OH species.[104] SrTiO_3 is one class of perovskite materials where the chemical stoichiometry is

governed by the formula ABO_3 . The crystal structure is cubic with the $Pm\bar{3}m$ space group (#221) and has a lattice parameter of 3.905Å. The unit cell in of $SrTiO_3$ is shown in Figure 3.1 where the origin is taken at the strontium atom. As in $\langle 100 \rangle$ orientation, the $SrTiO_3$ structure is comprised of alternating layers of SrO and TiO_2 with the distance of $a_{STO}/2$ ($a_{STO}=0.3905$ nm) as shown in Figure 3.1. The surface physical and chemical properties must be greatly influenced by the surface morphology and the ratio of these two kinds of terminated domains. The surface termination of $SrTiO_3$ has been studied rather extensively.[105, 106] Chemical etching is also applicable to such material as SrO is a basic oxide and TiO_2 is an acidic oxide, controlling the pH of the wet etch solution one should be able to prepare an atomically smooth and clean surface, e.g., Kawasaki et al.[106] succeeded to obtain a low contaminated smooth TiO_2 plane by treating the $SrTiO_3$ (100) substrate with a BHF solution. He concluded that the BHF solution selectively dissolved the SrO atomic plane to form an atomically smooth surface terminated by the TiO_2 atomic plane. More important, wet chemical etching is in a solution phase which has strong potential to improve surface hydroxyl groups than other methods.

3.2: Experimental

3.2.1 Sample preparation and wet chemical etching

The SC-STO wafers are usually prepared as follows: Starting with nominally pure (approximately 99.99%) $SrTiO_3$ powder as a starting material, a $SrTiO_3$ single crystal boule is grown by the Verneuil method.[107] The obtained single crystal boule is black at a glance. After annealing at about 1000K in a reducing gas atmosphere, the crystal boule becomes colorless transparent.[108] The annealed crystal boule is cut into several parallel plates followed by

mechanical polishing to optical flats, which is supplied to many workers as a substrate crystal for thin film deposition and as a specimen for different studies. The purity of starting material powder, the crystal growth apparatus, and the cutting and polishing processes usually depends on the crystal manufacture company. Such differences are thought to be the main causes for the observed specimen-dependent properties of real SrTiO₃ single crystals. As-received single crystal wafers used in this chapter are (100) oriented SC-STO substrates measuring 10mmx10mmx0.5mm from MTI Corp. (Richmond, California) with one (100) side EPI polished using CMP technology which yields less sub-surface lattice damage.[109]

In order for morphology analysis later, a selected as-received sample was mechanic polished and ion beam milled to be electron transparent for TEM analysis before any further processing. For composition analysis evolves with different treatment methods, we investigated two different types of SC-STO samples: as-received EPI polished SC-STO and prepared electron transparent TEM sample. Two chemical solutions are used in this work for SC-STO etching: formic acid mixed with hydrogen peroxide (FA-HP, formic acid Vol. ratio is 60%, hydrogen peroxide Vol. ratio is 30%, leftover is deionized water (18 MΩ/cm)). The other is buffered hydrofluoric acid/ammonium fluoride (BHF, Riddel-de Haen part no. 40207, pH~5) solution mixed with hydrogen peroxide (BHF-HP, BHF Vol. ratio is 66.6%, hydrogen peroxide Vol. ratio is 33.3%). The etching procedure is illustrated in Figure 3.2. Before etching, selected samples were quickly soaked in deionized water for 1 min and then subsequently etched using two solutions mentioned above with different duration. Right after etching, the substrates were rinsed in DI water for 1min and repeated 3 times. Finally all etched samples are dried with high purity nitrogen flow before further analysis and treatment. It is also expected that etching will recover

the surface from non-stoichiometric surface of TEM sample due to mechanical polishing and ion beam milling.

3.2.2 X-ray photoelectron spectroscopy (XPS)

Two interested composition, e.g. carbon and hydroxyls group, is analyzed using XPS (model ESCALAB 250Xi, Thermo Scientific, UK), Figure 3.3. XPS is an inherently surface sensitive method for examine chemical species and their bonding states. XPS data was collected in the analytical chamber using monochromated Al K- α X-ray source and a 180 °C double focusing hemispherical analyzer. The X-ray source irradiates the sample with 1486 eV incident X-rays. Electrons ejected from the sample were collected and their kinetic energy (KE) was measured by the hemispherical analyzer. The electron orbital binding energy (BE) is then determined from the photoelectron effect:

$$BE = h\nu - KE - \phi \quad (1)$$

The work function (ϕ) was accounted for by normalizing each scan to the known SrTiO₃ Ti-2p_{3/2} peak energy of 458.8 eV. The surface sensitivity is due to the small mean free path of photoelectrons, which are reabsorbed by the sample if they originate more than a few nanometers below the surface. Surface sensitivity can be enhanced by using a smaller angle θ between the sample surface and the detector, as the penetration depth is relative to $\sin(\theta)$. For this work an angle of $\theta = 45^\circ$ is used.

To check for all elements, a survey scan from 0-1400 eV was conducted with energy step of 0.4-0.5 eV. Each region of interest (O 1s, C 1s, Ti 2p, Sr 3d) was scanned in more detail with a 0.1 eV step size, averaging over 5-10 repeat scan. During operation, an electron flood gun was running simultaneously in order to minimizing surface charging. The binding energy shift due to

residue charging was shifted by an amount aligned with the highest point in the SrTiO₃ Ti 2p_{3/2} peak with a binding energy of 458.8 eV. Collected XPS peaks were then deconvoluted after a Shirley background subtraction from recorded peaks using Gaussian-Lorentzian curves which were optimized with constrain of peak positions.

The main feature of interest was a high binding energy shoulder of the O 1s peak, which can indicate the presence of hydroxyl group on the surface, and C 1s peak. Hydroxyl groups, however, are not the only possible source of such a high binding energy shoulder e.g. in TiO₂ rutile, the presence of Ti³⁺ also leads to a high binding energy shoulder on the O1s peak. It is therefore important to make sure that the sample is not reduced before attributing the O1s high binding energy shoulder to the presence of hydroxide. The oxidation state of titanium can be easily seen in XPS by looking at the Ti 2p region at ~460 eV. The Ti⁴⁺ Ti 2p_{3/2} peak in SrTiO₃ normally is present at 458.8 eV. If any Ti³⁺ is present, it would cause a low binding energy shoulder. The Ti_{2p3/2} peak was therefore checked for such a shoulder. Hydroxyls group intensity is determined using a peak ratio of high binding energy shoulder (OH shoulder) (531.9 eV) and oxygen peak (529.7 eV). Carbon contamination is characterized using a ratio between C1s (285.2 eV) and Sr 3p (279.3 eV) peak, Figure 3.4.

3.2.3 Transmission electron microscopy sample preparation and image recording

Transmission electron microscopy (TEM) is commonly used for structural characterization of a range of technologically important materials. For the study here, TEM analysis was performed on JEOL 2100F and Hitachi H8100 operated at 200 keV accelerating voltage and a base pressure of $\sim 1 \times 10^{-1}$ torr. The samples were prepared by standard solid-state TEM sample preparation methods following the procedure as shown in Figure 3.5a: single crystals wafers

SrTiO₃ were first cut into three millimeter discs using a rotary cutter (Figure 3.5b) and an abrasive slurry. Then the discs were mechanically polished to a thickness of approximately 100 μm, and the center were further thinned to a thickness of less than 25 μm using a Gatan Dimple Grinder (Figure 3.5c). Samples were then ion milled using Ar⁺ ions in a Gatan Precision Ion Polishing System (PIPS, Figure 3.5d) to electron transparency. An initial high energy of 8 kV was used for the Ar⁺ ions to quickly thin the sample, which was gradually decreased to the minimum possible value as the samples became thinner in order to minimize the damage from ion-milling. Below a minimum energy, which varied somewhat depending on the condition of the PIPS, the ion guns may stop fire. Thus the minimum energy used was not constant among samples, but was generally in the range of 2.5 – 3.0 kV.

3.2.4 Platinum ALD

Platinum ALD here was accomplished using alternating exposures to (methylcyclopentadienyl)trimethylplatinum (MeCpPtMe₃, Sigma-Aldrich 99%) and water at 250 °C using 120 standard cubic centimeters per min (sccm) of ultrahigh purity (99.995% pure) nitrogen purging gas pass through the ALD reaction chamber which makes the chamber holds at a steady state pressure of ~ 1 torr, Figure 3.6. During the MeCpPtMe₃ exposures, a 5 sccm of N₂ was passed through a stainless steel bubbler containing the MeCpPtMe₃ heated to 50 °C, and the N₂ was diverted to bypass the bubbler after the exposures. Each Pt ALD cycle consisted of a 300 s exposure to MeCpPtMe₃, a 600 s N₂ purge period, a 120 s exposure to H₂O, and a final 600 s N₂ purge period. After ALD deposition, sample was directly transferred for TEM and XPS analysis without any further treatment.

3.3: Result and discussion

3.3.1 Carbon removal and hydroxyl group enrichment on SC-STO (100) surface

The result corresponding to different treatment is summarized in Figure 3.7. The result indicates that annealing (240 min, 700 °C in air) is helpful for contamination removal but will lead hydroxyl intensity decrease meanwhile, e.g., removal of 17% contamination on as-received EPI polished SC-STO will also yields a 15.6% hydroxyl group loss and on TEM sample the lost ratio of carbon and hydroxyls is 30% and 23.4% respectively. Figure 3.7 also indicates that procedures of mechanic polish of ion beam milling used for TEM sample preparation will increase surface carbon contamination (+12.1%) and hydroxyls (+51.1%) simultaneously. The behavior of simultaneously removal and increase of carbon and hydroxyls from STO surface suggests that partial of the changed hydroxyl groups are located on varied carbon contamination. Such hypothesis is further supported by continuous two different wet chemical etching at room temperature, e.g., initial 20 min BHF-Hydrogen Peroxide removes 47.3% carbon and 63.7% hydroxyl groups or Formic Acid- hydrogen peroxide etching removes 39.4% carbon and 59.1% hydroxyls. Following 20 min etching with these two solution behaviors differently comparing to initial 20 min, carbon will continuously decrease while hydroxyl groups start increase. The increased hydroxyl intensity during this 20 min is generated direct on STO surface. Continuous etching (>40 min), BHF-HP can further remove carbon contaminations and increase surface hydroxyls. However, FA-HP is saturated for both hydroxyl enriching and carbon removing after 40 min etching. BHF-HP etching of SC-STO is considered as combination of following two processes: BHF-HP etching of SrO layers [106] and hydrogen peroxide oxidation removal of carbon.[110] As demonstrated by Kawasaki et al that SrO is a basic oxide which can be easily removed by PH controlled BHF etching and left the surface TiO₂ rich.[106] Meanwhile,

hydrogen peroxide is a source of highly reactive hydroxyl radical which generated through photolysis, $\text{HOOH} + h\nu \rightarrow 2 \cdot\text{OH}$. [110] Hydroxyl radical will worked as a strong oxidant to degrades and decompose carbon layer from surface. [111] With increase of TiO_2 layer after SrO removal, photon generation of radicals will contribute for carbon removal which through combination of hydroxyl group in solution with photon generated hole on TiO_2 surface, $\text{OH}^- + h \rightarrow \cdot\text{OH}$. [112, 113] Hydrogen radicals generated through this process may become dominated for carbon removal with hydrogen peroxide consuming through either carbon removal reaction, decomposition ($2\text{HOOH} \rightarrow 2\text{H}_2\text{O} + \text{O}_2 - 98.2\text{kJ/mol}$) or vaporization. The surface hydroxyl groups increase during late BHF-HP etching is due to new created TiO_2 surfaces. Such surface is photoinduced hydrophilicity and OH group is generated through photochemical reactions. [114] During FA-HP etching, hydrogen peroxide plays an essential role of carbon removal. As exhaustion of hydrogen peroxide around 40 min etching, carbon removal is stopped which explained saturated removal of carbon in Figure 3.7. The carbon removal by wet chemical etching is a kinetic process and depends on etching temperature. [115] Higher temperature will yield a higher rate comparing to room temperature. Figure 2 shows the BHF-HP etching result under room temperature and 45 °C which suggests that higher solution temperature will yield higher removal rate. Kinetically removal of carbon species can be described by Arrhenius relation,

$$K = t \exp\left(-\frac{E_a}{kT}\right) \quad (2)$$

where K is etch rate, E_a is activation energy, k is Boltzmann constant and T is etching temperature in Kelvin. Data presented in Figure 2 suggests activation energy for removal of carbon contamination is about 0.27 eV (26 kJ/mol).

3.3.2 Morphology and composition study of SC-STO before ALD

Transmission electron microscopy (TEM) of JEOL-JEM 2100F operated at 200 keV and XPS was applied here for morphology and composition analysis of as-prepared and BHF-HP etched (40 min at 45 °C) SC-STO TEM sample before platinum ALD, as shown in Figure 3.8. High resolution transmission electron microscopy (HRTEM) indicates as-prepared TEM sample is suffers from lattice damage caused by ion beam damage during sample preparation which we believe the surface is kind of off stoichiometry. Inserted diffraction pattern shows the surface is without any reconstruction and with pure 1x1 termination. HRTEM of Figure 3d shows elimination of surface damage owing to BHF-HP etching. Two interested composition (e.g. carbon, hydroxyl) on two samples also shows apparent difference; As-prepared TEM sample covered with much more carbonaceous layers than BHF-HP etched one. Hydroxyl group on BHF-HP etched TEM sample is slight lower (30%) due to carbonaceous layer removal as part of hydroxyl groups are sit on it. However, the OH spices on the STO surface are believed to be increased according to previous analysis.

3.3.3 Study of deposited Pt nanoparticles on SC-STO substrates with different treatment

Both types of substrate are used for Pt ALD deposition which was accomplished using alternating exposures to MeCpPtMe₃ and water as discussed above. Figure 3.9 a,b shows HRTEM images of 3 cycles Pt deposition on as-prepared and 5 cycles deposition on BHF-HP etched SC-STO TEM sample respectively. In order to distinguish Pt nanoparticles from STO background in HRTEM recording, the beam is tilted off low index zone axis on purpose. The image clear shows Pt nanoparticles on both substrates as discrete nanoparticles with average size ~ 1.9 nm which is similar to the Pt particles deposited on STO-NCs as will be discussed in

coming chapter with same deposition condition. However, negligible amount of Pt nanoparticles are found on as prepared SC-STO substrates comparing to BHF-HP etched one. XPS results in Figure 3.10 shows deposited Pt on BHF-HP etched SC-STO are basically Pt⁰ (~ 88.5%) with only a small portion of Pt⁴⁺ (~11.5%). As really low loading of Pt are presented on as-prepared TEM sample, the noise to signal ratio is relative high which made it difficult to identify the chemical state of the particle. However, with HRTEM analysis we can distinguish lattice fringes of deposited nanoparticle which suggests that both deposited nanoparticles are metallic may with small portion of PtO_x at interface or surface. Quantitative analysis according to XPS studied results of Pt deposited on both types of SC-STO is summarized in table 3.1. All data presented in Table 3.1 is calculated based on XPS peak area ratio of according elements with sensitivity factor counted in. The result suggests that BHF-HP improved average Pt deposition amount per cycle by a factor of 10. As BHF-HP etching improves surface from two aspects: First, BHF-HP etching creates a surface covered with far less carbon contamination which even remains 60% less carbonaceous layer after 6 cycles deposition than as-prepared TEM sample after 4 cycles deposition. In addition, BHF-HP etching enriches surface hydroxyl group directly on STO surface which makes the surface more reactive for Pt precursor adsorption especially during the 1st cycle deposition.

3.4: Conclusion

In summary, we successfully improved Pt ALD on single crystal STO by using wet chemical BHF-HP etching. By using TEM and XPS, we proved that more Pt can be deposited using ALD on BHF-HP etched surface than one without any treatment. As BHF-HP etching efficiently removes carbonaceous layer and increase surface hydroxyl groups on STO surface. Pt

ALD deposition on such surface will benefit Pt precursor adsorption which yields higher nucleation density through further surface reaction. Such treatment can be potentially expanded for surface improvement of other substrates material before ALD deposition, e.g. silicon, barium titanate and titanium dioxide. However, composition of etching solution may vary considering different properties of target material.

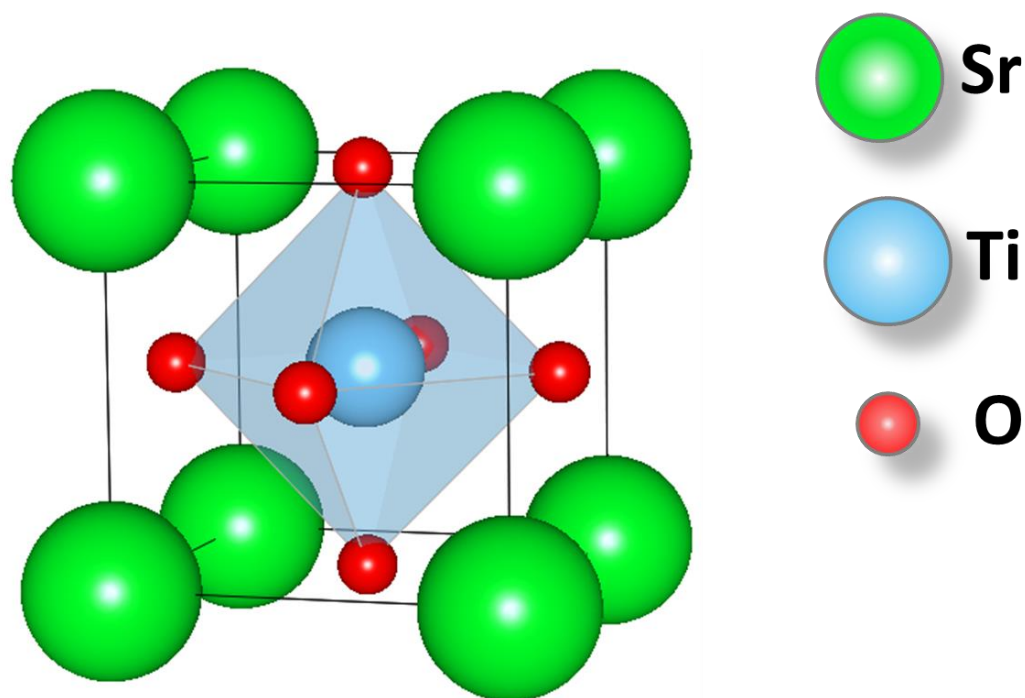


Figure 3.1. Crystal structures for SrTiO₃ (b). The respective lattice constants are 0.3905 nm. The space group of SrTiO₃ is $P\bar{m}3m$ (#221).

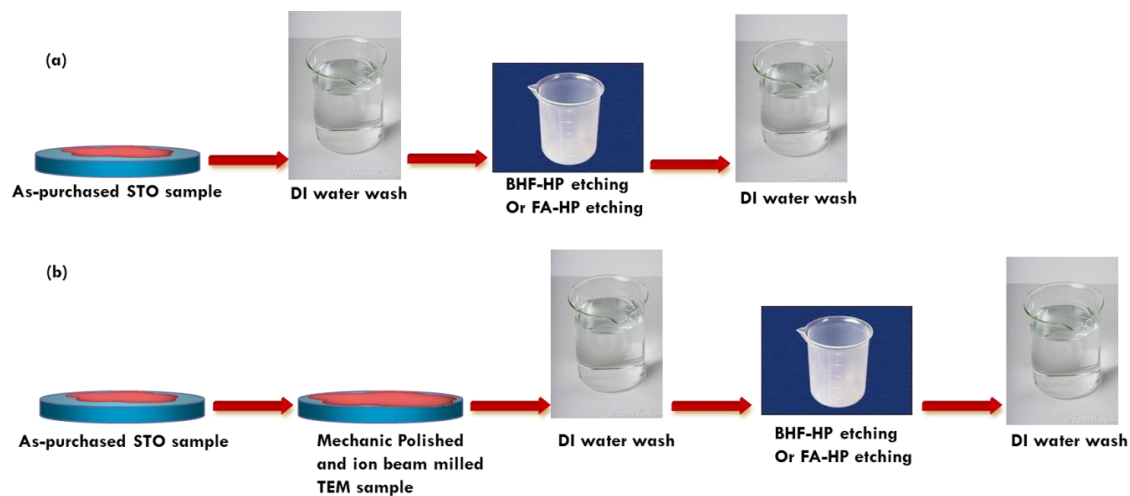


Figure 3.2. Diagram shows etching procedure of different sample (a) as-purchased EPI polished sample (b) mechanic polished sample.



Figure 3.3. X-ray photoelectron spectroscopy ESCALAB 250Xi at Nuance Center Northwestern University.

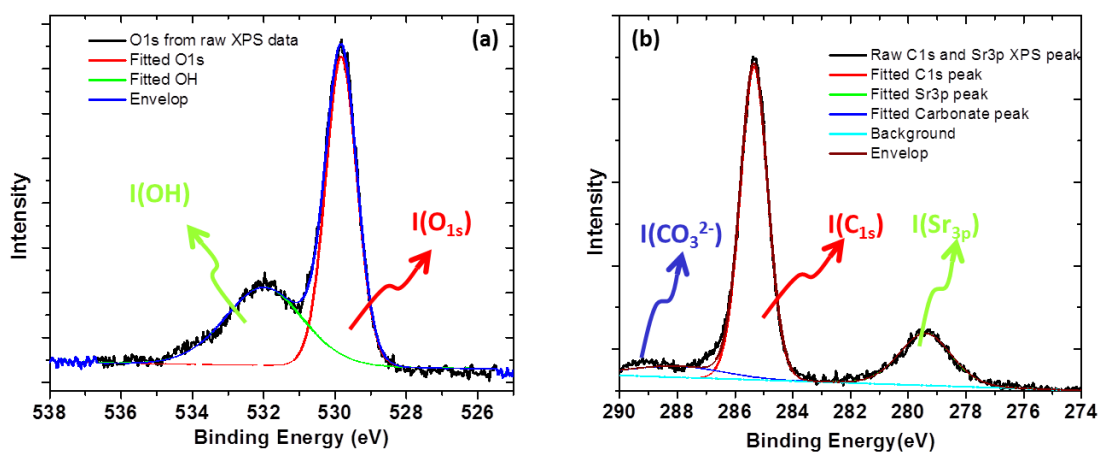


Figure 3.4. (a) O 1s core level XPS peaks of SC-STO with Gaussian profiles denoted as O1s and OH, respectively; (b) C 1s and Sr 3p_{1/2} XPS peaks of SC-STO with Gaussian profiles denoted.

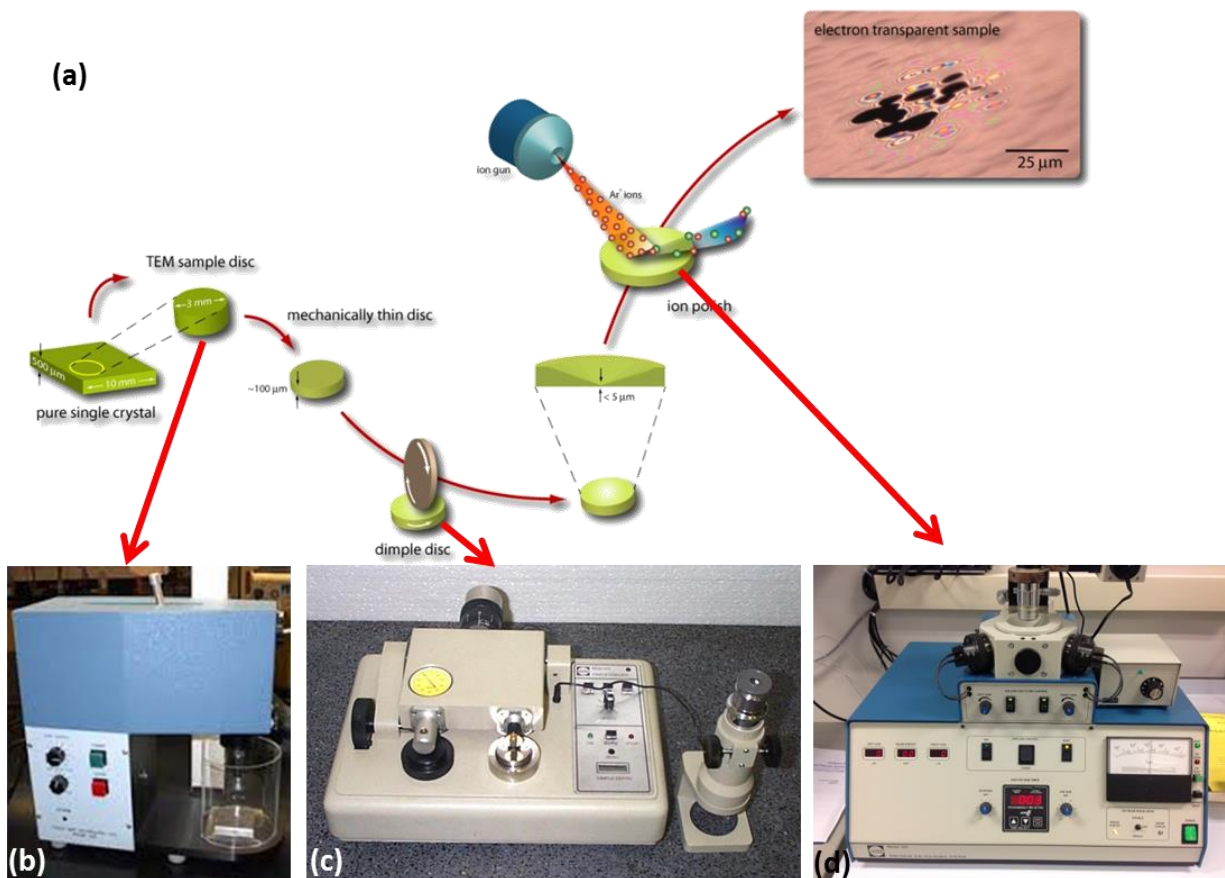


Figure 3.5. (a) Schematic diagram shows the procedure of single crystal strontium titanate TEM sample preparation. (b) Image of a rotary cutter (c) A Gatan Dimple Grinder (d) A Gatan Precision Ion Polishing System.

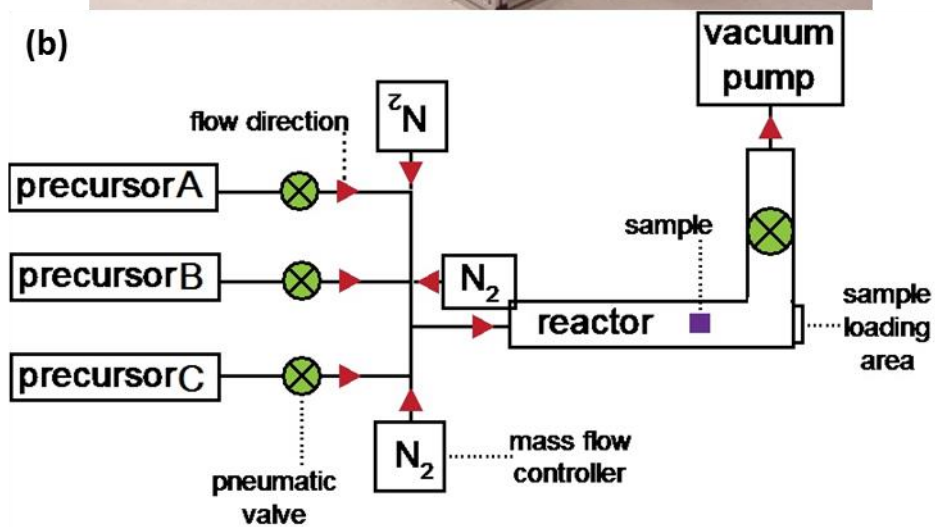
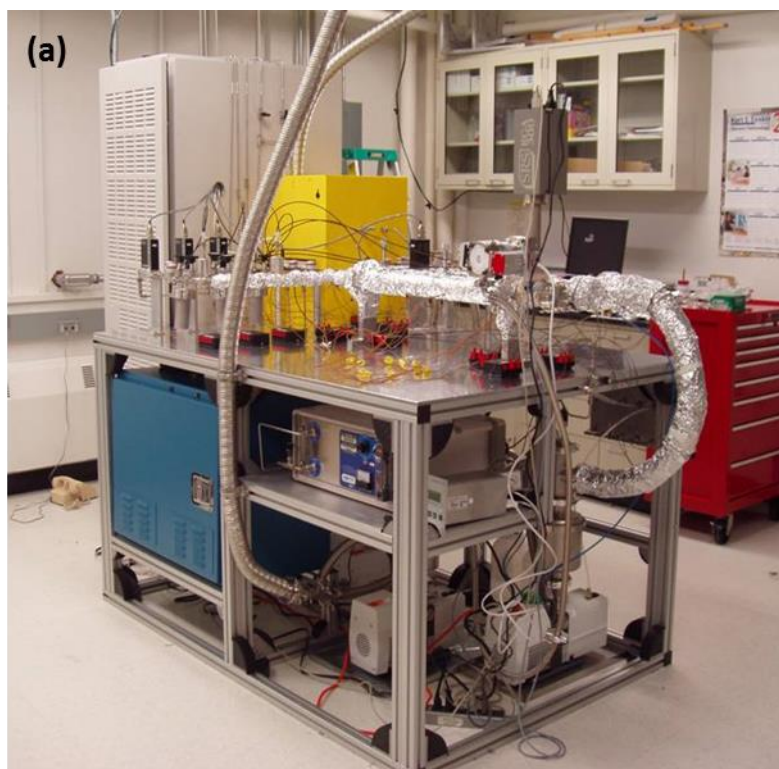


Figure 3.6. (a) A photograph of atomic layer deposition equipment used in this work. (b) Schematic diagram of all connected components of the ALD system.

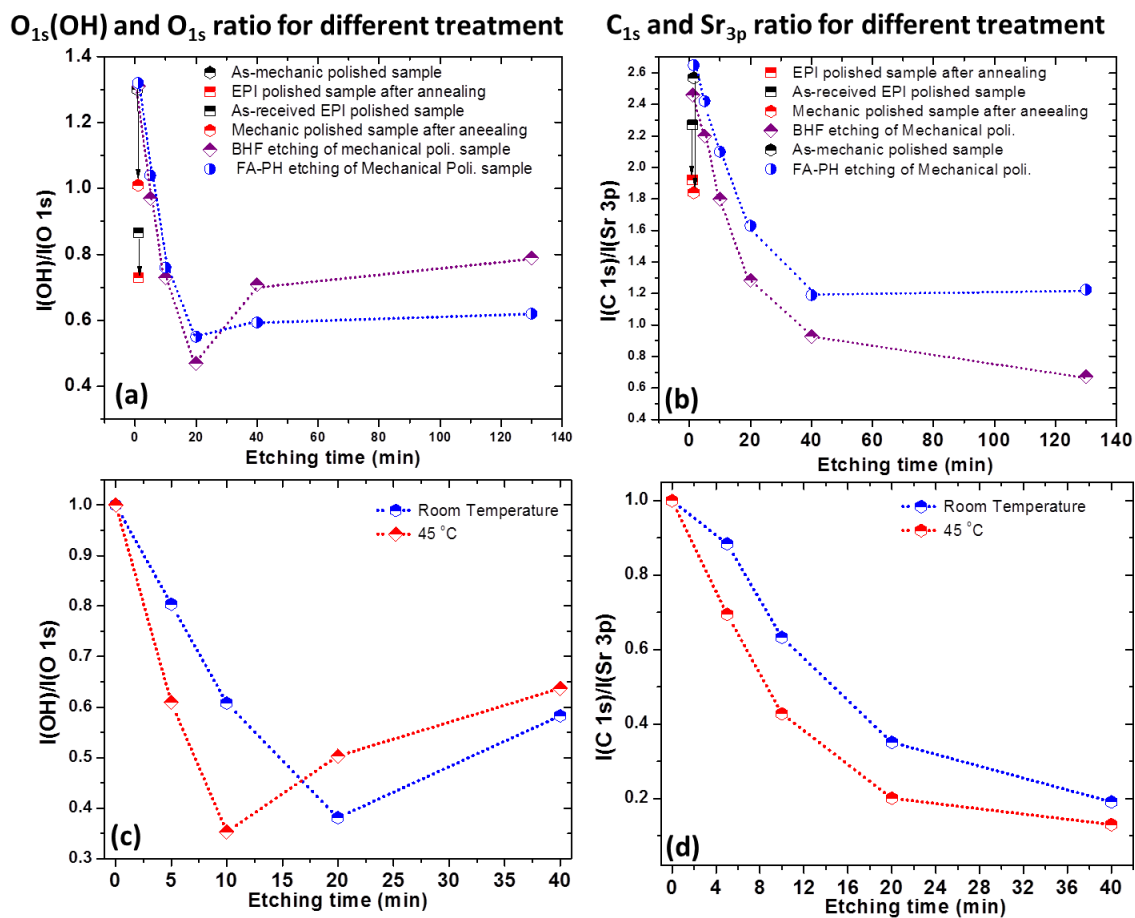


Figure 3.7. Surface composition evolution of carbon and OH species with different chemical etching. (a) OH species changing with FA-HP and BHF-HP etching. (b) OH species changing with FA-HP and BHF-HP etching. (c) (d) Carbon and OH on SC-STO with BHF-HP etching at elevated temperature.

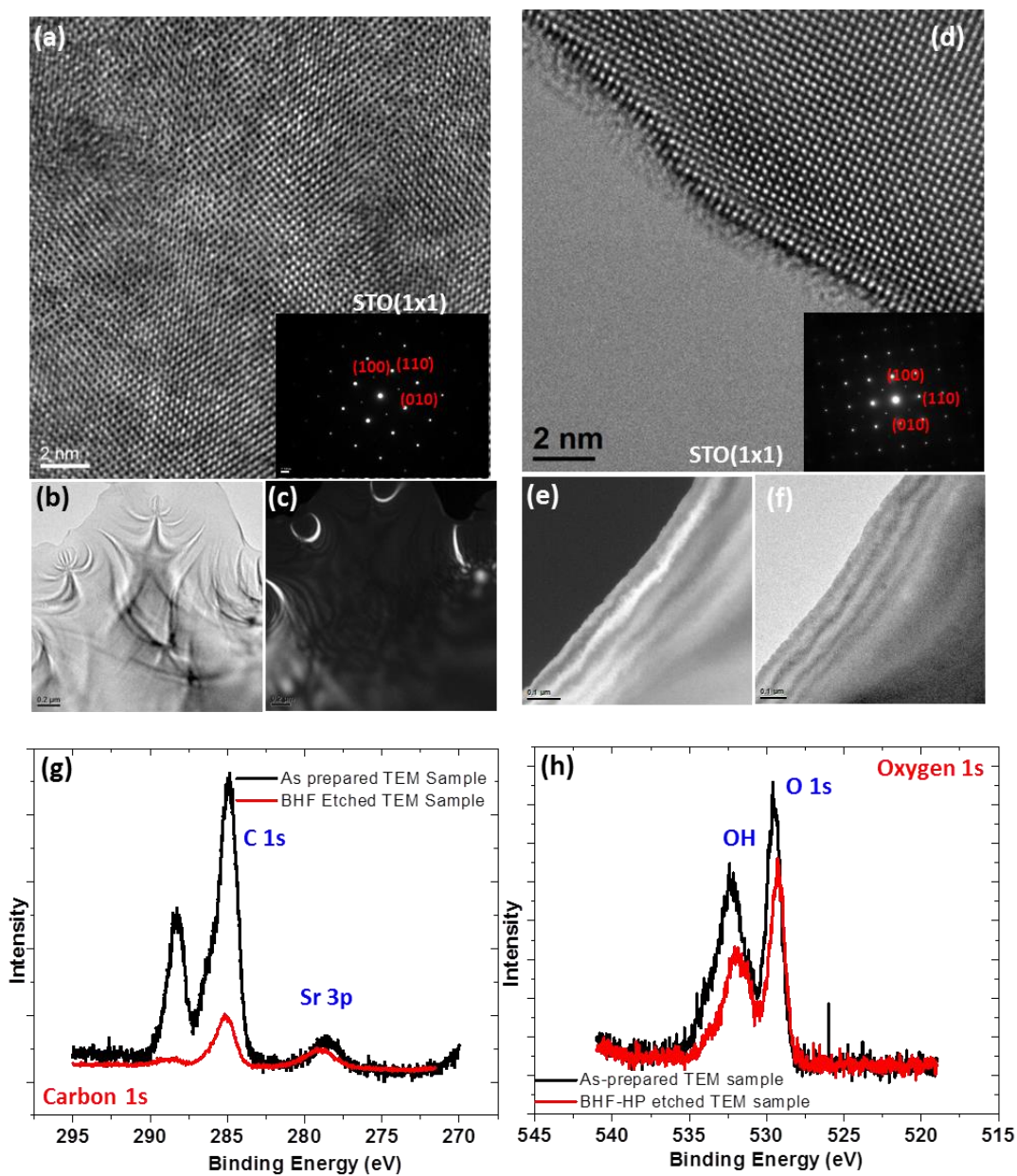


Figure 3.8. HRTEM, dark field and bright field image of as-prepared SC-STO TEM sample (a),(b),(c) and BHF-HP etched SC-STO TEM sample (d),(e),(f), inserted image in (a)(d) is diffraction pattern of corresponding sample. (g) (h) is XPS C1s and O 1s peak of two types of TEM sample.

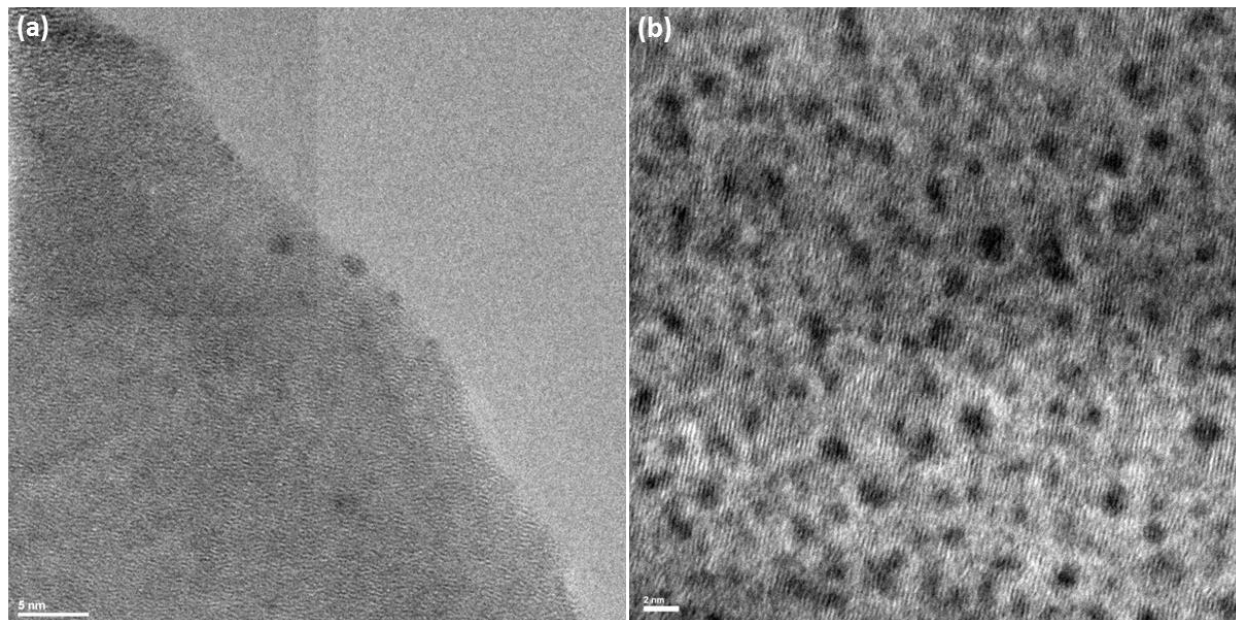


Figure 3.9. HRTEM of Pt/SC-STO (a) Pt deposited on as-prepared TEM sample. (b) Pt deposited on BHF-HP etched SC-STO TEM sample.

Table 3.1. Summary of XPS analysis of Pt deposited on two type of SC-STO sample

	BHF-HP etch sample	As-prepared
Pt 4f/Ti 2p	0.237	0.015
C 1s/Ti 2p	1.322	3.438
Ti 2p/Sr 3d	1.066	0.900

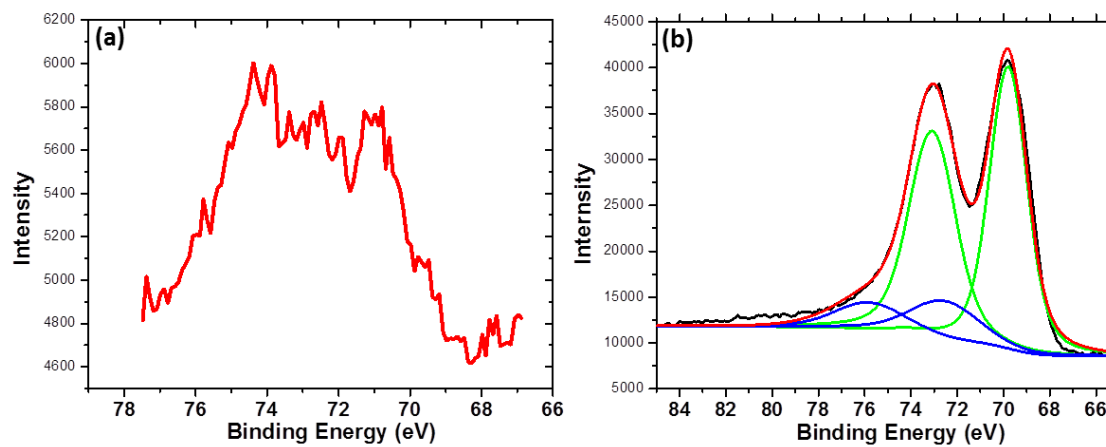


Figure 3.10. Pt 4f core level XPS peaks of (a) Pt/as prepared SC-STO TEM (b) Pt/BHF etched SC-STO.

Chapter IV:

**Controllable ALD Synthesis of Platinum Nanoparticles by
Tuning Different Synthesis Parameters**

4.1: Introduction

Nanometer-sized platinum nanoparticles supported on metal oxide surfaces can serve as effective heterogeneous catalysts for accelerating electrochemical [116-118] photochemical [119, 120] and thermal processes[121, 122]. Engineering the size, dispersion, shape and exposed surface of these nanocrystals is important. Numerous attempts of the size, shape and orientation controlled synthesis of Pt nanocrystals have been reported since the pioneering work of El-Sayed et al. in 1996;[13, 49, 123, 124] and a number of size and structure sensitive reactions have been described. For example, Feliu et al. reported shape dependent methanol and formic acid electrooxidation on preferentially oriented Pt nanoparticles.[125] Zaera et al. described tuning the selectivity of isomerization reactions by controlling the particle shape of Pt.[126] and Somorjai et al. demonstrated the shape effects of Pt nanocrystals on benzene hydrogenation selectivity.[127] Croy et al. mentioned that decomposition of methanol is size dependent of Pt nanoparticles supported on nanocrystalline anatase TiO_2 . [128] Well-controlled synthesis of nanocrystals is critical to correlate interested properties such as size, shape, composition and exposed surfaces to catalytic performance. However, with traditional preparation techniques including impregnation, ion-exchange, and deposition-precipitation, the metal nanoparticles usually lack atomic-level control of the catalyst composition and surface structure, yielding relatively large metal clusters with a broad size distribution, extreme low loading and undetermined exposed surface.[129-132]

Finer platinum nanoparticles can be deposited by physical vapor deposition (PVD) [133] and chemical vapor deposition (CVD)[134] techniques. Particles deposited by CVD usually are even more uniform than these deposited by PVD and therefore CVD is preferred when uniform

distributed particles are needed. Precursors such as CpPtMe_3 (Cp=cyclopentadienyl)[135], MeCpPtMe_3 , [136, 137] $\text{Pt}(\text{acac})_2$ (acac=acetylacetonate)[138], and $\text{Pt}(\text{hfa})_2$ (hfa=hexafluoroacetylacetonate)[139] are, for example, available for CVD of platinum thin films among which MeCpPtMe_3 is most widely studied CVD precursor because of its low melting point of 30 °C.[140] Although CVD has been shown to be capable of producing high quality platinum film and particles, atomic layer deposition (ALD) would be even more attractive alternative as it could show significant advantages over size, density, composition controlling. These properties gain increasing importance especially when ALD is used for heterogeneous catalyst synthesis. [49, 50, 141]

As discussed in Chapter I, ALD is a developed from chemical vapor deposition, wherein thin films are grown via a sequence (usually binary) of self-limiting chemical reactions between precursor vapors and the surface.[36, 82, 142] The self-limiting character of the reactions makes it possible to achieve uniform and precise controlling over deposition on high surface area or porous solids.[143-145] Hence, the design and synthesis of advanced nanoscale catalysts become possible through independent control over the structure and composition of the underlying support, the catalytically active sites and the protective over layer.[50, 141] ALD has proven successful for the controlled synthesis of supported monometallic catalysts.[145] More advantages of this technique for nanometallic catalysts have been discussed extensively.[13, 146, 147] The specific ALD processes in this chapter are for low cycles (< 15) of Pt deposition onto STO-NCs.[59] The synthesis of Pt on the STO-NCs is of particular interest as such system has been extensively studied as model catalysts, e.g. for fuel production.[91, 148, 149] Recently, ALD Pt/STO nanocubes have shown favorable results as a combustion catalyst.[150] The

success of the Pt/STO system in these applications also lies in the STO support. Due to comparable band gaps, STO acts as a UV photocatalyst similar to TiO_2 [151], in which photons generate electron–hole pairs that catalyze reactions to produce fuels such as hydrogen or methanol. The analysis based on this specific system can be translated to similar systems (e.g. Pd/STO-NCs, Pt/Barium titanate nanocubods (BTO-NCs) and Pd/BTO-NCs) and provides a basic understanding of these types of processes.

The aim of this Chapter is to investigate how will specific ALD parameters influence Pt nanoparticle size, density, loading, chemical state and exposed surfaces. Variables of interest include ALD method, reaction temperature, number of cycles, reagents and support. Lu et al. observed differences between ALD methods for controlling particle size and density after several cycles of ALD.[50] In this part, three ALD methods will be investigated for Pt nanoparticle synthesis: 1) traditional AB-type, 2) ABC-type and 3) static ABC-type ALD. The impact of reaction temperature, number of ALD cycles performed, and precursor identity on particle formation have also been extensively discussed in the literature [146, 152, 153], as these factors play a critical role in the deposition process. The reaction temperature determines how the precursor fragments, the extent of which influence the quantity of carbonaceous material that remains after the purge period. The number of ALD cycles impacts the particle size through diffusion controlled growth. The choice of both A and B precursors has also proven to impact particle synthesis.[150, 154] Aaltonen et al. stated that A precursor such as $\text{Pt}(\text{acac})_2$ is not thermal stable and may destroyed the self-limiting mechanism.[79] Setthapun et al. demonstrated that the Pt nanoparticle had a higher percentage of PtO_x when oxygen is used as the B precursor but more metallic when hydrogen is used.[150] More importantly, the proper selection of the B

reagent can alleviate steric hindrance effects by efficiently eliminating residual surface hydrocarbons before subsequent precursor exposures, which results in more absorbed precursor molecules and a higher growth rate.[153] Understanding the impact of the substrate on nanoparticle growth is also desired, as it has been proven by many early catalytic studies that support materials play a very important role in the selectivity and reactivity of the catalyst. Change of the support can alter the chemisorption and catalytic behavior dramatically.[5-7, 155-158] Catalyst support materials are generally selected for their high surface area, as well as thermal, chemical, and mechanical stability. Recent synthesis of high surface area oriented STO-NCs opens up new possibilities for catalyst supports.[25, 59, 159] According to Lin et al's recent work, STO-NCs prepared through hydrothermal synthesis have primarily low energy (100) facets exposed. The difference of synthesis conditions results in different surface termination which provides possibility of facilitating the study of Pt nanoparticle formation on these two different surfaces.[1] [160]

4.2: Experimental

4.2.1 Morphology and surface structure of two types of STO-NCs

Two types of STO-NCs are employed as supporting substrates in this study, both of which are synthesized using hydrothermal treatment. One is well discussed in Chapter II and TEM characterized shows these cuboids are single crystalline with narrow size distribution (~20 nm) and the (100) surface primarily exposed, Figure 4.1.[25, 59] The other type is well studied and discussed by Federico et al. [25] and Lin et al.[1] which is similar in several aspects as the first

one such as single crystalline, narrow size distribution and (100) surface exposed. However, obvious differences in properties such as particle size, Brunauer–Emmett–Teller (BET) surface area, porosity and termination, are also observed from these two types of STO nanocuboids. More specifically, STO-NCs reported by Federico et. al using acetic acid [25] during synthesis is porous with 20 m²/g BET surface area and TiO₂-rich reconstructed termination[1], while the other one are nonporous with 70 m²/g BET surface area and terminated with (1x1) SrO, Figure 4.1.[1] For both types of substrates, compared to normal single-crystal substrates with far lower surface area[161] or high surface area supporting materials with amorphous shape or undetermined exposed surface[147]. Considering STO-NCs are both prepared using hydrothermal methods which involves two organic metal precursors and organic solutions (e.g. acetic acid) or surfactant (e.g. oleic acids) which might made the product be covered with certain amount of residue carbon species, e.g. a full layer of oleic acid ligands is presented on STO-NCs with oleic acid synthesis as discussed in Chapter II. Thus all used STO support was pretreated with ozone for 15 min in the ALD reaction chamber at 200 °C to remove any carbon contamination before ALD. Such treatment is proved to be effectively for carbon removal (section 2.2.4, Chapter II). In the following discussion, we will refer these two types of STO nanocuboids as STO-NCs (OA) and STO-NCs (AA) for they are prepared with assistance of oleic acid (OA) and acetic acids (AA) respectively.

4.2.2 Platinum ALD deposition

Pt depositions on STO-NCs after ozone bath as described above were accomplished in the same viscous flow reaction chamber as described in Chapter III, which is with a base pressure of 0.3 torr. An ultrahigh purity (99.999%) nitrogen (N_2) flow of 125 sccm increases the chamber pressure to 1 torr during deposition. To accomplish different types of ALD deposition here, metal precursor and reagents such as $MeCpPtMe_3$ (Sigma - Aldrich 99%), titanium tetraisopropoxide (TTIP, Sigma - Aldrich, 97%), trimethyl aluminum (TMA, Sigma - Aldrich, 97%), oxygen and water doser are used. All necessary precursor bubblers are heated to an appropriate temperature in order to achieve sufficient vapor pressure and reasonable dosing times, e.g. $MeCpPtMe_3$ \sim 0.08 torr @ 50 °C, TTIP, TMA \sim 69 torr @ 60 °C and water \sim 25 torr @ room temperature. The STO substrates are first loaded and uniformly spread in a stainless steel tray (Figure 4.2a) which was then covered by a stainless steel mesh before transferred to the ALD reactor. The stainless steel mesh can easily be access by the ALD precursors.

First deposition strategy is called traditional ALD which is a two-step process with each step separated by N_2 purging. This ALD process consists of alternating A/B precursor doses; $MeCpPtMe_3$ was used for precursor (A) and oxygen or water was used for precursor (B). This method will also be referred to as AB type ALD in this study. During deposition, a 5 sccm N_2 flow was passed through the bubbler to assist in the transport of $MeCpPtMe_3$ to the reaction chamber. The timing sequence is expressed as t_1 - t_2 - t_3 - t_4 , where t_1 is the $MeCpPtMe_3$ precursor dose time and t_2 is the purge time, t_3 is the water or oxygen dose time and t_4 is the second purge time. The specific times used here were 300s-600s-120s-600s. In order to increase Pt nanoparticle loading without changing particle size, the newly developed ABC-type ALD method was also performed. This method consists of three alternating precursors, A, B and C,

which were MeCpPtMe₃, TTIP(or TMA) and water, respectively.[50] The timing sequence used here was t₁-t₂-t₃-t₄-t₅-t₆, where t₁, t₂ are the time length for the MeCpPtMe₃ precursor dose and subsequent purging time; t₃, t₄ are the TTIP (or TMA) dose and the following purging time; t₅, t₆ are the water dose and final purging time, which were 300s-600s-60s-600s-120s-600s in this experiment.

For Pt deposition with these precursors, static ABC-type ALD is similar to ABC with a related dosing sequence. The major difference between these two processes is that regular ABC-type has a continuous 125 sccm N₂ flow through the reaction chamber with slight pressure fluctuation in the thermal reaction chamber during the entire operation while during static ABC-type the exhaust valve is closed and only a N₂ flow of 5 sccm is used to transport the Pt precursor, Figure 4.2b. During static ABC-type ALD the reaction chamber is a closed system with significant pressure changes after Pt precursor exposure compared to the other two methods even with the same precursor dosing duration. For example, after a 300 s dose the reaction chamber pressure increases significantly from 0.32 torr to 4.1 torr, Table 4.1. Discussion of Pt deposited by these three methods will be saved for later.

4.2.3 Characterization

The size, dispersion and morphology of Pt nanoparticles were determined with high-resolution and scanning transmission electron microscopy (HREM and STEM) by JOEL 2100 operated at 200kV. The TEM samples were prepared by dripping some as-synthesized Pt/STO

dispersed in ethanol onto the surface of a lacey carbon film supported on a copper grid as described in Chapter II. The Pt weight loading was determined using inductively coupled plasma atomic emission spectroscopy (ICP-AES) (Varian VISTA ICP-AES). These samples were prepared by dissolving 5 mg of Pt/STO in a mixture of 1 mL of nitric acid with 3 mL of hydrochloric acid for 48 hours to form a clear light yellow solution, Figure 4.3. Chemical composition and state of the different elements of Pt/STO were characterized using XPS (model ESCALAB 250Xi, Thermo Scientific, UK). A monochromatic Al Ka (1486.6 eV) anode was used under UHV conditions with a base pressure of 6.5×10^{-10} torr. The experimental resolution was less than 0.1 eV and a low energy electron flood gun was also used here during data acquisition to reduce binding energy shifts caused by charging.

4.3: Results and discussion

4.3.1 General morphology and structure of Pt/STO-NCs

Figure 4.4 of the Pt coated STO-NCs shows that the ALD deposited Pt as small, well dispersed nanoparticles. The TEM imaging of the 5 cycles Pt coated on STO-NCs (oleic acid) revealed the size and density of nanoparticles are similar to the 5 cycles of Pt deposited on STO-NCs (acetic acid) at 200 °C using MeCpPtMe₃ and H₂O. HAADF imaging was also employed to further assess the size distribution, density of Pt nanoparticles deposited with different cycles and ALD temperatures. As-deposited Pt nanoparticles in this studies exhibit very narrow size distribution, with sizes ranging from 1 to 3 nm, depending upon number of ALD cycles and reaction temperature, and remarkable uniform dispersion over the surface of the oxide support,

e.g. one Pt ALD cycle on STO-NCs (oleic acid) at 200 °C led to particles of 1.5 nm diameter, while 15 Pt ALD cycles produced platinum particles of 2.41 nm diameter. No significant agglomeration of the metal particles was observed for all commenced number of cycles in this work. HREM images indicate that the main phase of present platinum nanoparticles are metallic. As the lattice fringes of metallic Pt (PDF No. 04-0802, space group $Fm\bar{3}m$, $a \approx 3.92 \text{ \AA}$) and STO (PDF No. 84-0444, space group $Pm\bar{3}m$, $a \approx 3.90 \text{ \AA}$) are close and STO can be terminated with either SrO or TiO_2 , epitaxy or non-epitaxy between STO and Pt can depend on STO support surface termination, e.g. strong epitaxy on TiO_2 termination and non-epitaxy on SrO terminated surface, is not surprising.[45]

4.3.2 Size measurement from HAADF images depends on probe size

The Pt particle size through ALD deposition in this work is typical around 1~3nm, so the role of electron probe size (~0.2–1.5 nm) on the size analysis of the HAADF images needs to be taken into account. To begin quantitative analysis of the individual nanostructure sizes of HAADF image, we need first consider all the contributions that give rise to the final observed spatial resolution, which requires determination of the contributing factors, including vibration, TEM alignment, focus and electron probe size, a final measured size will be a function of these factors,

$$\text{Measured size} = F(\text{vibration, probe size, focus, Real size}) \quad (1)$$

In above equation, the probe size usually depends upon alignment of the microscope as well as other operational factors such as focus, source coherence, demagnification, aperture size and more all of which we assume are tuned to acceptable levels. The contribution from vibration is from the environment surrounding the TEM and cannot be avoided; however it is normally small ($< 0.2\text{nm}$) compared to the probe size in our experiments. For fully incoherent imaging, which requires a large inner and outer collection angle, the image of a nanoparticle will be the convolution of the probe and the intensity across the particle,

$$\text{Measured size} = \text{Probe size} * \text{Real size} \quad (2)$$

A series of HAADF images of Pt/STO-NCs deposited with 1 cycle ALD at $300\text{ }^{\circ}\text{C}$ were taken with different probe sizes, shown in Figure 4.5a-e, and summarized in Figure 4.6a. The sizes of Pt NPs were measured based on the full width of line intensity profile across Pt NPs on STEM-HAADF images (\sim average of 80 measurements), which is usually determined by the background locally; in the case that NPs were not round, the size was based on the average of the largest and smallest measured diameters. If the probe is substantially smaller than the particle, to a reasonable approximation the apparent size of a particle will be the sum of the true size and some constant multiplier of the size “p” reported by the microscope for the probe size. As shown by Figure 4.6a, the measured particle size is linearly depended on the probe size with a constant multiplier factor of ~ 0.46 . Similar analysis on other samples as shown in Figure 4.6b, e.g. Pt/STO-NCs prepared with 1 cycle ALD deposition at $200\text{ }^{\circ}\text{C}$, $215\text{ }^{\circ}\text{C}$, $250\text{ }^{\circ}\text{C}$, suggests that this relationship is solely TEM dependent. A linear fit of all plotted data in Figure 4.6b suggests that the relationship between the probe size and measured particle size is,

$$M(p)=0.46p+R \quad (3)$$

with $M(p)$ is measured particles, p is probe size and R is real size. From the equation above, the real particle size can be determined with a known electron probe size. All particle diameters plotted in the following work which is real size determined using equation 3.

4.3.3 Temperature dependence of Pt ALD synthesis

The temperature dependence of the Pt ALD process is studied by depositing a single cycle of $\text{MeCpPtMe}_3/\text{H}_2\text{O}$ on SrO terminated STO-NCs(OA) within the temperature window of 125 °C-300 °C using different ALD methods. Figure 4.7 shows a series of High Angle Annular Dark Field-STEM (HAADF-STEM) images of Pt/STO-NCs deposited at 200 °C, 250 °C and 300 °C using AB-type ALD, suggesting Pt nanoparticles were uniformly dispersed on STO-NCs with a narrow size distribution of ~1-2 nm for all temperatures studied. The temperature influence of the ALD process affects the combustion of precursor fragments at the start of MeCpPtMe_3 adsorption, growth of Pt nanoparticles by altering the net Pt deposition.[136] As reported by Mackus et al., activation of the adsorption of the MeCpPtMe_3 precursor is not the limiting factor during the reaction.[153] The precursor absorbs onto the substrate through ligand exchange between surface hydroxyl groups and methyl ligands of MeCpPtMe_3 . Higher reaction temperatures lead to a higher percentage of decomposed and combusted ligands, resulting in more net Pt single atoms on the STO-NC surface. These single atoms are not energetically stable and continuous surface nucleation process quickly takes place. As the nucleation process will consume Pt atoms around the newly formed Pt nucleus which makes the Pt concentration below

the minimum requirement for nucleation, thus nucleation stops whereas growth continues. The growth process is denoted by diffusion of Pt atoms that originate relatively far from the cluster to the cluster surface. It has been mentioned by Zhou et al, the diffusion of Pt atoms is sufficiently activated at ALD reaction temperature to allow for Pt atom transport to larger clusters.[162] We expect that the final Pt particle size after one complete cycle will increase with increasing ALD reaction temperature for increased net Pt deposition. As shown in Figure 4.8, the results (averaged result of ~80 measurement) presented are obtained based on the HAADF images of Pt/STO-NCs (Oleic Acid) synthesized under the corresponding reaction temperatures. The results show that particle size increase with ALD reaction temperature in the temperature range investigated which is consistent with the discussion above.

Platinum particle density (number of Pt particles per unit area) was measured by counting the number of particles in a selected area as illustrated in Figure 4.9a, with the measured results (averaged result of ~20 measurement) plotted as a function of temperature in Figure 4.9b. During a measurement of nucleation density, sample tilting effects are avoided by measuring nanocuboids right-aligned along the $\langle 100 \rangle$ zone axis in a selected HAADF-STEM image. Measured nucleation density is divided by 2 considering Pt particles were uniformly deposited on the top and bottom surfaces, Figure 4.9c. As shown in Figure 4.9b, particle density also increases with reaction temperature which is strongly determined by nucleation density after Pt precursor deposition. As reaction temperature increased, more precursor ligand fragments are eliminated and steric hindrance effects are alleviated which allows more MeCpPtMe₃ molecules to be adsorbed, resulting in more Pt atoms on STO surface after further ligand removal.[150] Nucleation density will increase when more Pt atoms are presented on surface as nucleation rate

will increase. Over the course of the investigated temperature window, 125 °C to 300 °C, the nucleation density increased about 13%.

As Pt particle size and nucleation density vary with ALD reaction temperature, Pt loading which is determined by these two factors will also be expected to be temperature dependent. As indicated by ICP-AES analysis shown in Figure 4.10, altering the reaction temperature will change the Pt loading. When the reaction temperature was low, 125 °C, a relatively low loading of 1.94% (27.7 ng/cm²) was observed after a single cycle ALD. For temperatures above 150 °C, the Pt nanoparticle loading was found to be roughly linear with increasing reaction temperature up to 275 °C. A similar behavior was previously reported by Mackus A. J. M. et al. for Pt ALD conducted in a temperature range between 150 and 450 °C.[152] Temperature above 300 °C is not further investigated, as it is beyond our ALD safety operation limit.

Additional HAADF-STEM and HREM images of Pt/STO-NCs synthesized using ABC-type and static ABC-type ALD suggest that the temperature dependences of particle size and particle density are similar to AB-type ALD for a single cycle of deposition, Figure 4.8 and 4.9. However, nanoparticles acquired by static ABC-type ALD are found to be slightly larger than those formed with the other two methods at the same ALD reaction temperature. This is likely due to a “CVD process” taken place during the Pt precursor exposure in a close pump environment which yields more net Pt deposition.

4.3.4 Dependence of size and density of Pt nanoparticles on number of cycle and ALD method

In the following, the influence of number of ALD cycles on obtained Pt nanoparticle size, nucleation density and weight loading are discussed. Pt/STO samples were prepared on oleic acid synthesized STO-NCs [59] using different ALD methods at 200 °C and 300 °C with single and multiple cycles. The effect of temperature, number of cycles and type of ALD method were investigated and the results are compiled in Table 4.2. The nanoparticles synthesized with 1, 5 cycles of traditional AB-type ALD at 200 °C, 300 °C were 1.51 nm, 1.80 nm and 1.78nm, 2.25 nm in diameter respectively implying that Pt particles grow with increasing number of ALD cycles. Increase in size of Pt particles per cycles is determined by net Pt deposition during that cycle as will be discussed in section 4.3.7. Once a Pt atom is deposited during a continuous cycle, it may diffuse over the SrTiO₃ surface and attached to a nanoparticle surface formed during previous ALD cycles.[162] Meanwhile as shown in Figure 4.12, the nucleation density was negligibly increased with number of ALD cycles, indicating that no new nucleation and coalescence processes take place during Pt precursor exposure in each new ALD cycle.

However, for Pt nanoparticles prepared using ABC-type and static ABC-type ALD, STEM images show the cycle dependence is different and nucleation of new particles dominates instead of particle growth as in traditional AB-type ALD. As detailed by Lu J. L. et al., the increase in the Pt nucleation density of continuous cycles is caused by the creation of new nucleation sites on the STO surface during the BC portion of the ABC-type ALD process (or static ABC) before the next Pt precursor dose.[50] Platinum precursor exposed to the freshly regenerated supporting surface will behave similar to the 1st cycle. As a result, the number of particles per unit area increases compared to previous cycles which is illustrated by increased nucleation density and slightly increased particle size in Table 4.2. In the case of static ABC-type ALD, the reactions

taking place during each cycle are a combination of traditional AB-type and ABC-type ALD. Similar to ABC-type ALD, a fresh surface with surface hydroxyl groups is generated prior to the Pt precursor dose which leads to new Pt particle growth. However during the dose the reaction chamber is isolated from pumping, particle growth will take place besides nucleation due to a “CVD process”. As a result both particle size and nucleation density will increase with increasing number of cycles increase.

The cycle dependence of three ALD methods at elevated reaction temperature of 300 °C is comparable to the dependence at 200 °C. However, impacts of reaction temperature on the synthesis need to be considered. As discussed in section 4.3.3, ALD accomplished at higher reaction temperature will yield larger particles and slightly higher nucleation density. Dependence of number of cycles for the three ALD methods at higher reaction temperature was also summarized in Table 4.2. This shows particle size and nucleation density of Pt nanoparticles prepared at 300 °C are comparable to these prepared at 200 °C but with particle size and density larger than the one at 200 °C.

4.3.5 Influence of supporting material on the structure and loading of ALD formed Pt nanoparticle

In this section, we focus predominantly on the influence of the substrate on the synthesized Pt nanoparticles by using two types of STO-NCs as supporting substrates. As shown in Figure 4.12, Pt/STO samples synthesized under the same conditions (200 °C, 1 cycle AB-type ALD) have differences in color implying difference in Pt loading on these two types of STO-NCs. A

quantitative ICP-AES study corroborates that the one that is light grey in color has a lower loading, 0.56% (MeCpPtMe₃ and H₂O), and the darker sample has a higher loading of 3.76% (MeCpPtMe₃ and H₂O). This difference in loading is believed to be caused by more than the difference in BET surface area. As normalized by surface area (STO-NCs(OA) ~70m², STO-NCs(AA) ~20m²), the Pt loading on oleic acid STO in a unit area is still 1.85 times higher than loading on acetic acid STO, which implies that the surface termination will also affect Pt loading.

The structure and growth orientation of Pt nanoparticles on the two STO-NCs are also different due to different surface terminations. As shown in the HREM image of Pt on STO-NCs(OA) and STO-NCs(AA) in Figure 4.13, the obtained Pt particles on both types of substrates are metallic with their lattice fringes aligned depending on the termination. For example, on the SrO terminated surface (oleic acid synthesis STO-NCs), Pt grows in a direction mix of <100> and <111>, Figure 4.13a. However, Pt deposited on acetic acid STO-NCs only grows in direction of <100> according to Enterkin J. A.'s work, Figure 4.13b.[13] The determination of Pt growth orientation on surface termination of STO-NC substrates can be understood in terms of an associated balance of chemical bond strength and particle surface energy across the interface.[105] In the case of Pt on TiO₂-terminated STO with acetic synthesis, epitaxial orientations minimize this as a higher degree of chemical bonding exists when Pt grows in (100). On the SrO terminated surface, as a mismatch of lattice fringe exists between the Pt and SrO terminated surface, bonds between Pt and STO surface are weaker which leads to growth of Pt with a mix of <100> and <111> direction. The shape of Pt particles is also determined by surface termination determined and can be predicted by Winterbottom construction, Figure 4.13c.[163] This theory describes how the interface free energy will determine the Winterbottom shape of the

particles. With different termination present, the corresponding interface free energy is believed to cause the difference in the shapes of particles. The Wulff shape[64] will be truncated at a plane, the location of which is determined by the difference between the interfacial energy and the substrate free energy which varies due to surface termination. More details will be discussed in chapter VI.

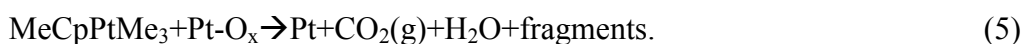
4.3.6 Role of reagent in ALD process

Pt ALD is often performed using oxygen at 300 °C to decompose the Pt precursor.[79, 153, 164] Other reagents have also been investigated for the synthesis, the purpose of which is either to reduce, oxidize or provide new nucleation sites on the supporting material for the next metal precursor dosing.[150] Water and oxygen are found to effectively help the deposition of Pt particles in this work according to ICP-AES and XPS studies. ICP-AES analysis suggests a Pt weight loading of 8.3% (water) and 14.8% (oxygen) for 6 cycles ALD synthesis at 250 °C on SrO terminated STO-NCs(AA), which indicates that oxygen are more effectively for Pt deposition than water. XPS analysis also shows a similar phenomenon for Pt deposited on TiO₂ rich terminated STO-NCs, as shown in Figure 4.14. A higher I(Pt 4f)/I(Ti 2p) peak ratio (after adjustment with the appropriate Scofield factor), except for the 1st cycle, was found for Pt/STO-NCs prepared using oxygen, as opposed to water under the same synthesis conditions. Figure 4.15 shows XPS Pt 4f peaks of as-synthesized Pt/STO-NCs (AA) using water or oxygen as the B reagent (6 cycles at 250 °C) which demonstrates obvious change in chemical state. For either synthesis, the XPS Pt 4f peaks shows coexistence of three components Pt(0), Pt(II) and Pt (IV).

Pt(0) and Pt(II)+Pt(IV) percentage according to XPS peak fitting, calculated as $I(\text{Pt}(0))/(I(\text{Pt}(0))+I(\text{Pt}(\text{II}))+I(\text{Pt}(\text{IV})))$ and $I(\text{Pt}(\text{II})+\text{Pt}(\text{IV}))/I(\text{Pt}(0)+I(\text{Pt}(\text{II}))+I(\text{Pt}(\text{IV})))$ respectively, was plotted as a function of the number of ALD cycles in Figure 4.16, which indicates that Pt ALD using oxygen yields more oxidized Pt than water after the same number of ALD cycles. Pt²⁺ and Pt⁴⁺ shoulder presents in Pt 4f XPS peaks are contributed by two sources: PtO_x monolayer formed on the particle surface and Pt-O bonds presented at the interface between the metal and oxide support, as Pt ALD usually start with ligand exchange of Pt precursor and surface hydroxyl groups.[105, 165] When particle size increase, surface to volume ratio decreases, e.g. for a hemispheric particle with a diameter of 1.0 nm the surface to volume ratio is 9 nm⁻¹; As size increases to 2 nm, surface to volume ratio decreases to 4.5 nm⁻¹. Thus, an increase in particle size should result in a decrease in the total amount of oxidized Pt, which is only formed at the particle surface or interface. As shown in Figure 4.16, the percentage of oxidized platinum decreases with number of ALD cycles, with a corresponding increase in the particle size.

For Pt ALD using oxygen as a B reagent, the amount of adsorbed oxygen that resides at the STO-NC surface after the O₂ pulse is an important parameter of the process because residual oxygen affects the nature of the reaction during the MeCpPtMe₃ pulse and the amount of adsorbing precursor molecules. The presence of oxygen atoms on the oxide surface during the MeCpPtMe₃ pulse leads to combustion of ligands during the precursor exposure. If ligands are eliminated before next precursor exposure, steric hindrance effects are alleviated and more MeCpPtMe₃ molecules can adsorb, resulting in a higher growth rate. Surface science results suggest that combustion of ligands takes place above roughly 300 K when oxygen and

hydrocarbons are both present at the surface which is the case at the start of the MeCpPtMe₃ pulse.[166] This condition is easily met for typical Pt ALD reaction conditions (125 °C - 300 °C). The reaction mechanism of this type of Pt ALD, which relies on autocatalytic oxidation of MeCpPtMe₃, is reported by Hiratani et al. in Pt chemical vapor deposition[136],



In equation (1), Pt-O_x represents molecular O₂ or dissociated O atoms on the Pt surface. The activation of the oxygen by dissociation into atomic oxygen on the Pt surface should not be difficult for oxygen can easily be dissociated at temperatures > 120 K as pointed out by Gland et al.[167] Formed Pt-O_x will react with adsorbed MeCpPtMe₃ precursors in an oxidative decomposition reaction (eq 2), resulting in CO₂ and H₂O reaction products, and possibly some hydrocarbon fragments.

Several studies have suggested that surface hydroxyl groups are involved in the reaction of Pt ALD.[168-170] Thus water can be used as second reagent for the ALD process in order to regenerate hydroxyl groups on the oxide surface. As pointed out by Christensen et al., the proposed mechanism for this reaction begins with the preferential adsorption and reaction of MeCpPtMe₃ with surface hydroxyls through ligand exchange between the methyl groups of the MeCpPtMe₃ molecule and hydroxyl groups.[150] The elimination of ligands is accomplished through thermal decomposition instead of oxidative decomposition as in the case of O₂. However, thermal decomposition process is not as efficient as the oxidation and elimination of ligands when oxygen is used. As a result, more carbonaceous layers will present on STO surface. Such

hypothesis is supported by XPS analysis of C1s level of as-synthesized Pt/STO-NCs(AA) prepared using water and oxygen. As shown in Figure 4.17, C1s/Sr 3p ratio was greater when H₂O was used as the B reagent than when O₂ was used even with other synthesis conditions held the same. When water is exposed to the STO surface partially covered with Pt nanoparticles, hydroxyl groups interact with these Pt nanoparticles and have a tendency on Pt to combine to produce a water molecule and a O²⁻ anion through Bronsted acid/base reactions ($\text{OH}^+\text{OH}^-\rightarrow\text{O}^{2-}+\text{H}_2\text{O}(\text{g})$).[171] O²⁻ generated here might involve ligand oxidative combustion. However, this effect is still very weak compared to directly using oxygen as the oxidant.

4.3.7 Pt nanoparticle formation through nucleation and diffusion controlled growth process

Fundamental understanding the process of Pt nanoparticle formation on a substrate will benefit us a lot, e.g. helping us precisely control particle size, density and composition. As supported by lot of recent work and some classic theories[49, 50, 161], ALD deposited nanoparticles are formed through two processes: nucleation and growth. For this section, we will investigate these two processes through a series of HAADF images using Pt/STO-NCs(OA), which can be generalized for other system. We will first discuss the nucleation process starting with the initial surface reaction. As discussed previously in section 4.3.3, to initiate Pt ALD on an oxide substrate, two requirements need to be satisfied: (1) adsorption of the Pt precursor MeCpPtMe₃, and (2) elimination of the precursor ligands.[150] When the Pt precursor was initially introduced to the ALD reaction chamber the MeCpPtMe₃ can absorb onto a clean surface by ligand exchange between surface hydroxyl groups and the methyl ligands of the

precursor.[172] The limiting step in the deposition is the elimination of the remaining precursor ligands which is more difficult than adsorption, usually done by thermal decomposition or oxidation and following purged by applied N₂ flow. Once ligands are eliminated, the adsorbed precursor is reduced to single Pt atoms.[173] However, single atoms are not energetically stable on a surface and result in subsequent surface nucleation which leads to formation of an initial morphology of Pt nanoparticle on the oxide surface. To determine experimentally how the Pt particle size depends on the amount deposited in the initial half-cycle, Pt ALD with different precursor dosing times was conducted for 1st-half reaction which only includes precursor dosing and purging at 200 °C. Particle size as a function of Pt precursor exposure time is shown in Figure 4.18 for samples removed immediately from the reaction chamber and then analyzed. The results indicate after 0.5 s precursor dosing, Pt particle with average size 0.69 nm will be formed suggesting that nucleation process accomplishes in less than 0.5 s with critical nucleation size (r_c) less than 0.35 nm (~ 7 Pt atoms). According to classical nucleation theory, Gibbs free energy change due to heterogeneous nucleation of a new phase with radius R for a truncated sphere with a contact angle theta is as shown in Figure 4.19:

$$W(r) = \left(\frac{4}{3} \pi r^3 \Delta G_V + 4 \pi r^2 \gamma_{pg} \right) \frac{2 - 3 \cos \theta + \cos^3 \theta}{4} + E_d \quad (6)$$

ΔG_V is enthalpy of formation per unit volume for Pt clusters from adsorbed atoms me, γ_{pg} ($184 \times 10^{-6} \text{J/cm}^2$)[174] is interfacial energy between Pt-Gas and E_d is energy change if nucleation takes place at a defect site, e.g. point defects such as surface vacancy, which is a more energy favorable as reported by Giordano et al and Haas et al.[175, 176]. If we assume a hemisphere ($\theta = 90^\circ$), then

$$W(r) = \frac{2}{3} \pi r^3 \Delta G_V + 2\pi r^2 \gamma_{pg} + E_d \quad (7)$$

According critical nucleation radius, with $\left. \frac{dW}{dr} \right|_{r_c} = 0$,

$$r_c = \frac{2\gamma_{pg}}{|\Delta G_V|} \quad (8)$$

As the nucleation start after Pt precursor adsorption and ligands elimination where Pt-O-X-STO will be formed, and final present state of Pt atoms on a substrate is in metallic form, thus the enthalpy of formation per unit volume is $(H_V - H_{adh})/V_m$, where V_m ($9.09 \times 10^{-6} \text{ m}^3/\text{mol}$) is molar volume of Pt. H_V [177] and H_{adh} [178] is enthalpies of sublimation and adhesion for Pt on STO (Figure 4.20). $H_V - H_{adh}$ is in the range 110 – 150 kJ/mol for silver based on the extrapolation of the particle size-dependent heat of adsorption measured for silver on $\alpha\text{-Al}_2\text{O}_3$ and MgO.[179] Assuming that this difference is also appropriate for Pt, this equation suggests that the critical nucleation size (radius) for Pt ALD ran at 200 °C is 0.2 - 0.3 nm (1 - 4 atoms) which is in reasonable agreement with the measured particle size after dosing for 0.5 s.

After nucleation, a depletion boundary forms around Pt nuclei as illustrated in Figure 4.21. Concentration of Pt atoms around formed Pt nucleus reduces below the minimum concentration for nucleation, whereas nucleation stops and the growth continue. Figure 4.18 shows that particle will further grow from 0.69 nm to 1.39 nm with Pt precursor dosing (0.5 s - 2 s), which suggests that there was a growth process after nucleation for the 1st cycle synthesis. During multiple cycle ALD synthesis after 1st one, the dominated process take place is growth of particle formed from previous cycles. There was no secondary nucleation or coalescence of previously formed

particles as suggests by almost steady particle density shown in Figure 4.11. As point out previously, the growth of particle is contributed by diffusion of Pt atoms that original far from the nuclei. The immigration distance of Pt atom on the STO surface during the ALD time scale is much larger than the nuclei distance ($\sim 5-10$ nm). Consider a particle of diameter d in which the atomic spacing is a , and assume no wetting of the support. The particle diffusion coefficient can be expressed as follows[180],

$$D_p = \frac{1}{6} \Gamma_p \alpha_p^2 \quad (9)$$

Where Γ_p is the particle jump frequency and α_p the particle jump distance. The particle jump frequency is simple the product of the atomic jump frequency Γ_s , and the number of atoms on the particle surface, i.e. $\pi d^2 / a^2$. Since $\Gamma_s = 4D_s / a^2$, where D_s is the surface self-diffusion coefficient, the express for Γ_p is

$$\Gamma_p = \frac{4\pi d^2 D_s}{a^4} \quad (10)$$

Now if a single atom jumps a distance a , this effectively results in the particle jumping a distance given by $a/(\text{total number of atoms in the particle})$ giving

$$\alpha_p = \frac{4a^4}{\pi d^3} \quad (11)$$

Substituting equation (12) and (11) into equation (10) gives the expression for the particle diffusion coefficient

$$D_p = \frac{24}{\pi} \left(\frac{a}{d}\right)^4 D_s \quad (12)$$

This indicates the strong dependence of D_p on atomic diameter a and particle diameter d for spherical particles. The expression can be used to calculate values of D_p for a range of diameters, and this to determine average particle migration distance in a given time. Here, and throughout the rest of this discussion, the parameters used will be those relating to platinum. The surface diffusion coefficient of platinum D_s , at the temperature T is given by relation,

$$D_s = D_{s0} \exp(-Q/kT) \quad (13)$$

The particle diffusion coefficient of a single Pt atom on the substrate can be induced from equation (14) and (13) as,

$$D_p = \frac{24}{\pi} D_{s0} \exp(-Q/kT) \quad (14)$$

Where D_{s0} is a frequency factor and Q is the activation energy. These parameters have been determined for bulk platinum using a variety of techniques; it is reasonable to assume that the surface diffusion rates on small particles will not differ greatly from these. Thus Blakely and Mykura[181], using the multiple scratch method, found that $D_{s0}=4 \times 10^{-3} \text{ cm}^2\text{s}^{-1}$ and $Q=1.79 \times 10^{-19} \text{ J/atom}$, producing a value for D_s at $600 \text{ }^\circ\text{C}$ of $1.4 \times 10^{-9} \text{ cm}^2\text{s}^{-1}$. The distance that a particle will migrate on a substrates in a time scale t is described by[180],

$$L = (D_p t)^{1/2} \quad (15)$$

The migration distance during ALD deposition ($t \sim 300\text{s}$) under different reaction temperature is summarized in following Table 4.3, which suggests that the immigration distance is larger than 10 nm. Thus during ALD time scale, single Pt atom can accomplish traveling from original adsorbed sited to particle surface to contribute for particle growth.

Figure 4.22 indicates that particle size are influenced by both reaction temperature and number of ALD cycles. As increase of size during 1st cycle behavior very distinguish from continuous cycles, thus we split the discussion into two parts: 1st cycle deposition and multiple cycle synthesis after 1st. The size of the Pt nanoparticles after the first complete ALD cycle is mainly dependent on the amount of Pt deposited and slightly on particle density, both of which are alternated with reaction temperature. The statement of particle size determined by net platinum deposition is supported by two analyses: Figure 4.18 implies that particle size increase with Pt precursor dosing time, as varies of which will alternate net Pt deposition. During initial stage ($\sim 5\text{s}$) of precursor exposure before adsorption are saturated, increase of Pt precursor time will increase net Pt deposition. A larger size in formed Pt nanoparticle with higher net Pt deposition suggests that particle size is strongly related to net Pt deposition. A direct evidence is also provide here that particle size of formed Pt nanoparticles are strongly related to net Pt deposition, which relies on comparing total mass in particle form with ICP-AES measured total mass. As shown in Figure 4.8, ICP-AES measurement of total Pt loading with ALD reaction temperature suggests that Pt weight loading increase with reaction temperature in the investigated range of 125 – 300 °C from 1.94% to 7.53%. On the other hand, total mass contained in measured Pt nanoparticle on 1 g STO-NCs (OA) can be calculated based on measured particle size and particle density as,

$$wt\% = \frac{2}{3} \pi R^3 \rho_N S \quad (16)$$

Where R is particle radius and ρ_N is particle density in a unit area measured from HAADF images. S is BET surface of used STO-NCs (OA) ($\sim 70 \text{ m}^2/\text{g}$). The Pt loading approached by two ways are plotted in Figure 4.23, which demonstrates that all deposited Pt are present in nanoparticle form. Thus for the 1st cycle ALD deposition, increase in net Pt deposition will mainly increase particle size. As increase of ALD reaction temperature from 125 °C to 300 °C, particle density will only increases slightly ($\sim 13\%$) comparing to net Pt increase ($\sim 288\%$).

After considering particle formation during the 1st cycle, we turn to the case of a series of cycles after 1st one. The most outstanding difference of Pt synthesis during continuous ALD comparing to 1st one is increase rate per cycle. Figure 4.22 shows that Pt particle growth in size of the first cycle was significantly higher than that for subsequent cycles. This difference is likely due to a carbonaceous layer that partially covers the STO-NCs surface after the first cycle. Figure 4.24a shows the C1s/Ti2p ratio from XPS measurements of STO samples before and after 1,3 and 5 cycles of Pt ALD at 200 °C. An obvious increase of carbon was observed after the first Pt ALD cycle. The C1s/Ti2p ratio after 3 and 5 cycles of Pt ALD deposition is essentially the same as after the first cycle, which implies that the residual carbonaceous layer reaches a steady-state coverage ($\sim 0.78 \text{ ML}$) that is specific to the specific reaction temperatures and purge conditions after the initial Pt ALD cycle. The major source that contributes to this layer is ligands from previous cycles that have not been completely removed.[75, 182] We note that water, instead of oxygen which is most often used in Pt ALD[152, 174], was used here to generate hydroxyl groups on the oxide surface. As reported by Setthapun W. et al., these species

will be the active sites that react with the Pt precursor.[173] However, the removal of carbonaceous layers using water as the second reagent in ALD will not be as efficient as when using oxygen or ozone, which will lead to an oxide surface partially covered by carbonaceous layers. One monolayer of carbonaceous material on a support surface can hinder further deposition of MeCpPtMe₃ and decomposition of the ligands by blocking adsorption sites.[75] As a result, the net Pt deposition change during each continuous cycle is much low than the 1st one as shown in Figure 4.24b. For multiple cycle ALD deposition, particle density are negligibly changed which suggests a minimum secondary nucleation or particle coalescence during new cycle deposition, Figure 4.11. By using same equation of (5), total Pt mass in Pt particles is calculated and plotted in Figure 4.25 which suggests that all deposited Pt will appear in particles and particle size change in a certain cycle will solely determine by net Pt deposition as particle density barely varies with deposition cycles.

Ultimately, a hypothetical schematic representation of Pt nanoparticles formation from 1st cycle and Nth (N>1) cycle is shown in Figure 4.26 which based on all discussion above. Since several surface reactions may occur simultaneously, it became too complex to include all detail in few pathways. Instead, the expected sequence of surface reaction is discussed here. During 1st cycle, Pt particles are formed through two processes: nucleation and growth. For deposition after 1st one, there is no secondary nucleation and coalescence of previously formed particles. The dominated process takes place here is growth of previously formed particles. Although above growth mechanism was analyzed replies on Pt/STO-NCs system, the approaches can also be generalized for other ALD synthesis, e.g. Pd/STO-NCs, Pt/TiO₂, Pt/barium titanate nanocubes (BTO-NCs), as the surface evolution may be very similar.

4.4: Conclusion

The effects of different parameters, e.g. reaction temperature, number of cycles, substrate, reagents and type of ALD methods, to acquired Pt nanoparticles are investigated individually in this work. Particle size, density and loading vary with reaction temperature, number of cycles and type of ALD method. Pt growth orientation and shape can be changed by using different substrates. And changing the 2nd reagent can leads to different chemical states and compositions. Thus, differences in particle size, density, loading, chemical composition, growth orientation and thermodynamic shape of deposited Pt nanoparticles can be understood by taking these influences into account.

During the initial cycle of ALD the deposition process begins with nucleation followed by growth, both occurring on a fast time scale relative to the deposition time. The final size is temperature dependent which affects the net Pt deposition. For multiple cycles, the particle size increases with the number of ALD cycles and the increase in size per cycle also relies on net Pt deposition during that cycles. The increase in size per cycle is significantly lower than first cycle. This effect is likely due to carbonaceous material left on the surface from decomposition of the MeCpPtMe₃ ligands. The growth behavior can also be used to be explained for other similar system as Pt/BTO-NCs, Pd/BTO-NCs or Pt/TiO₂ etc., as the surface reaction takes place might be very similar.

This work also opens a way for better understanding of metal nanoparticle synthesis using ALD control of size, density, growth orientation etc. can be accomplished by tuning the different parameter discussed above. We expect that this work will help improve catalytic performance

when these particles are used for catalytic purposes, as selectivity and reactivity are often heavily dependent on catalyst size, shape, dispersion, exposed surfaces and chemical state.

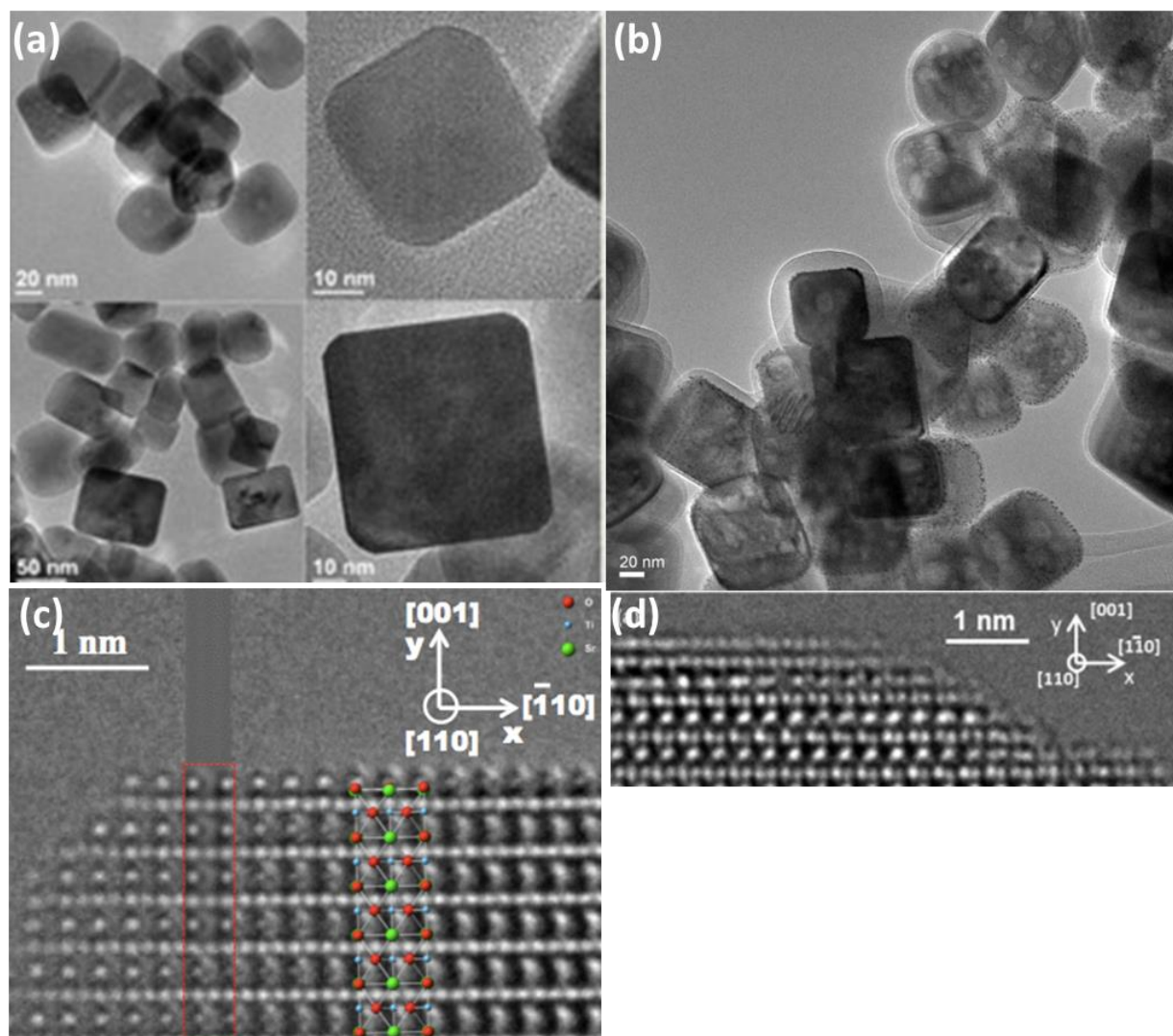


Figure 4.1. TEM images of STO-NCs with two different hydrothermal synthesis methods. (a), (c) STO-NCs with oleic acid synthesis which is described in Chapter II. (b),(d) STO-NCs with acetic acid synthesis as described by Federico et. al.

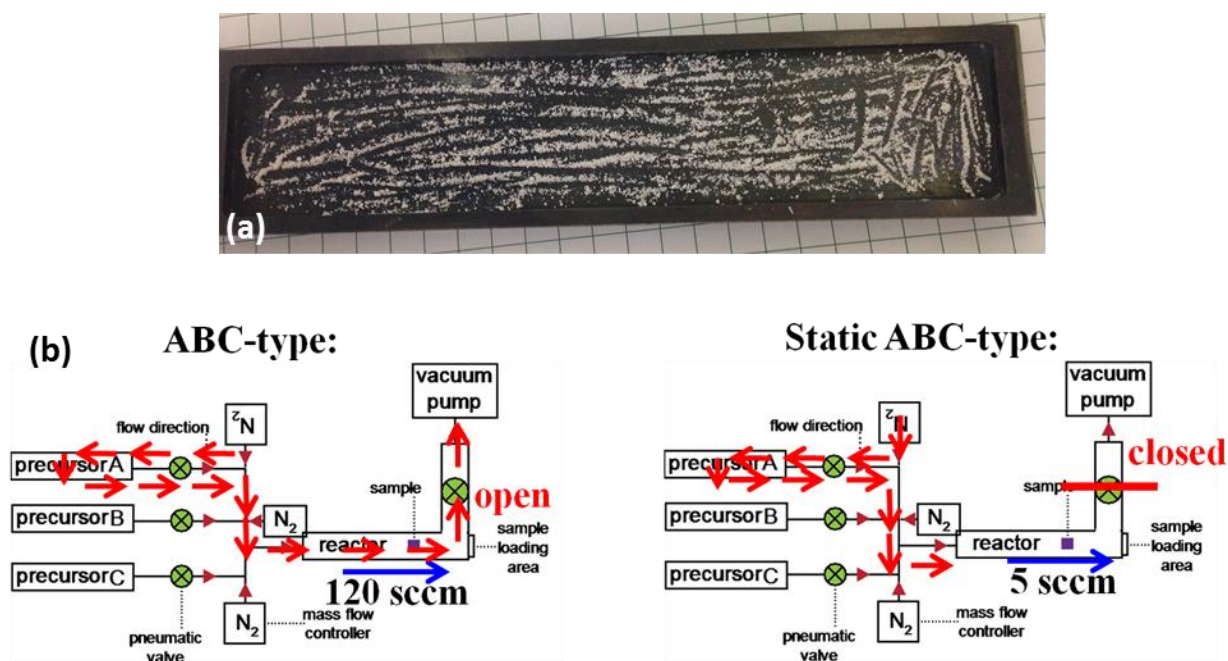


Figure 4.2. (a) Image shows STO-NCs substrates are well spread in a stainless steel tray before loaded into ALD reactor (b) Schematic diagram shows the N_2 flow route during Pt precursor deposition for ABC-type and static ABC-type ALD.

Table 4.1. Comparison between ABC-type and Static ABC type ALD

	N_2 flow	Exhaust valve	Pressure Variation
ABC-type	120 sccm	open	0.03 torr
Static ABC	5 sccm	closed	0.32→4.10 torr



Figure 4.3. A light yellow solution of 5 mg Pt/STO dissolved in a mixture of 1 mL of nitric acid with 3 mL of hydrochloric acid.

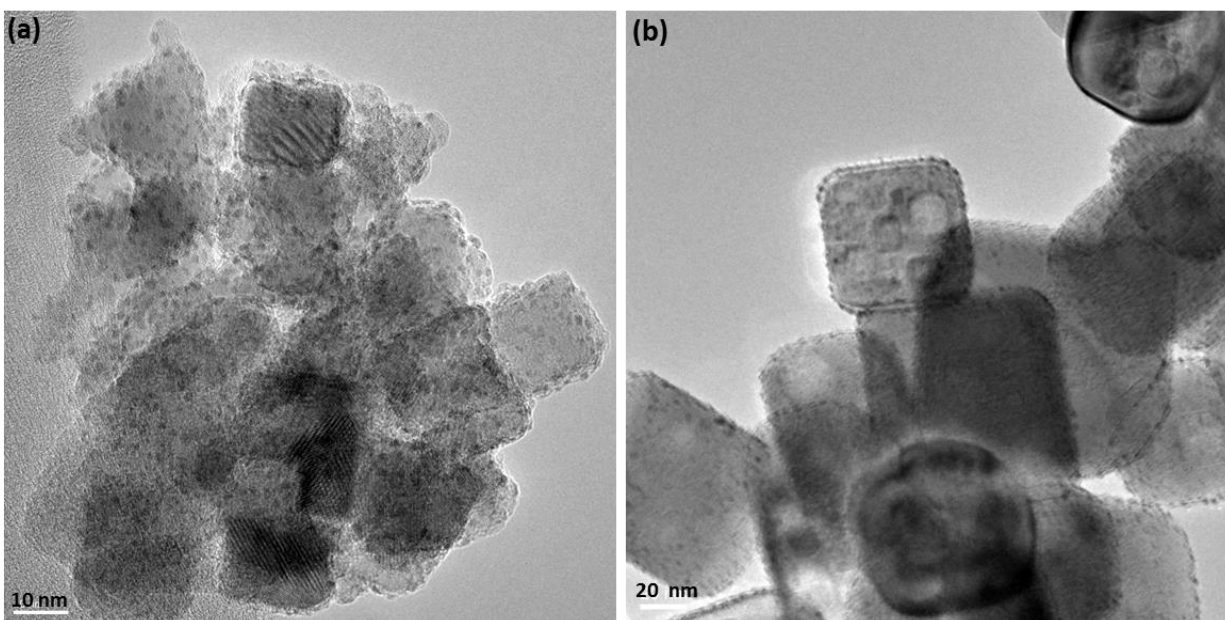


Figure 4.4. (a) A HREM image of Pt/STO-NCs (oleic acid) (b) TEM image of Pt/STO-NCs (acetic acid) obtained with 5 cycles at 200 °C using MeCpPtMe_3 and H_2O .

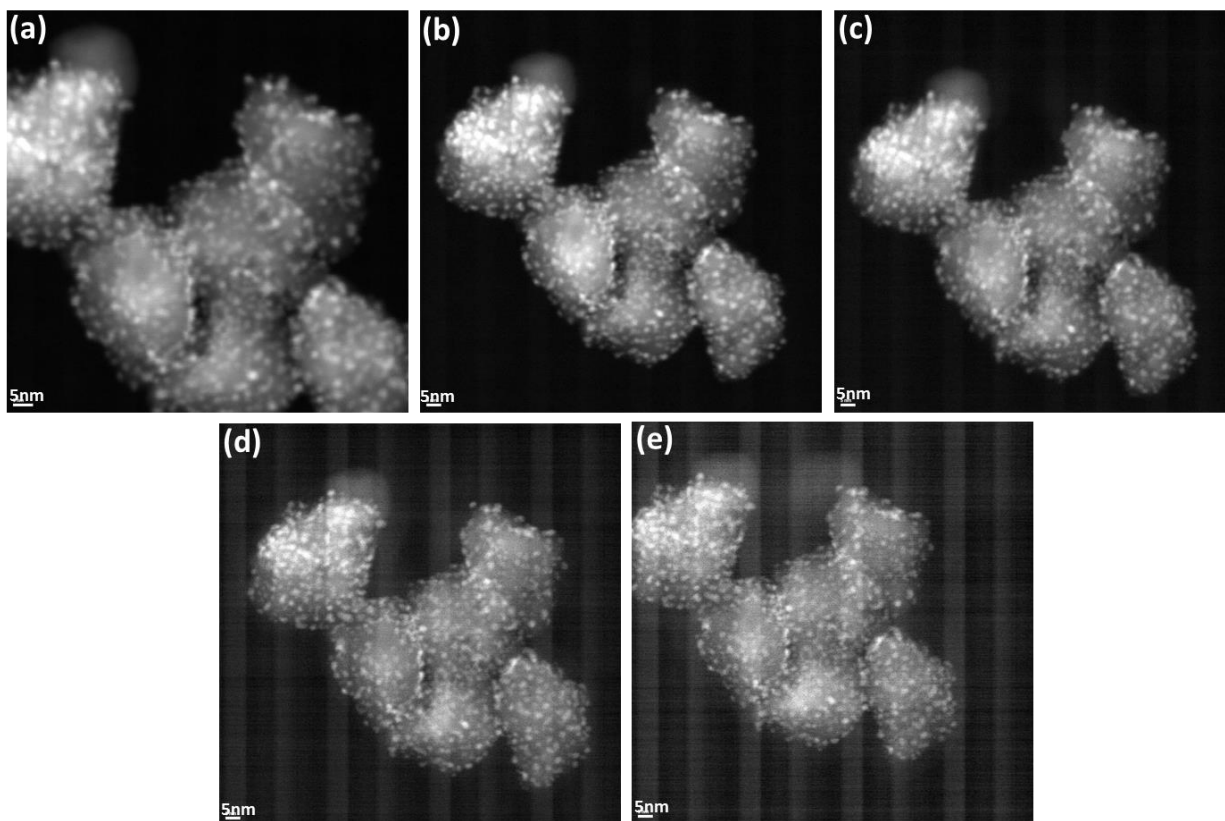


Figure 4.5. HAADF images of Pt/STO-NCs (1 cycle 300 °C) taken with a range of electron beam probe sizes (a) 1.5 nm (b) 1.0 nm (c) 0.7 nm (d) 0.5 nm (e) 0.2 nm.

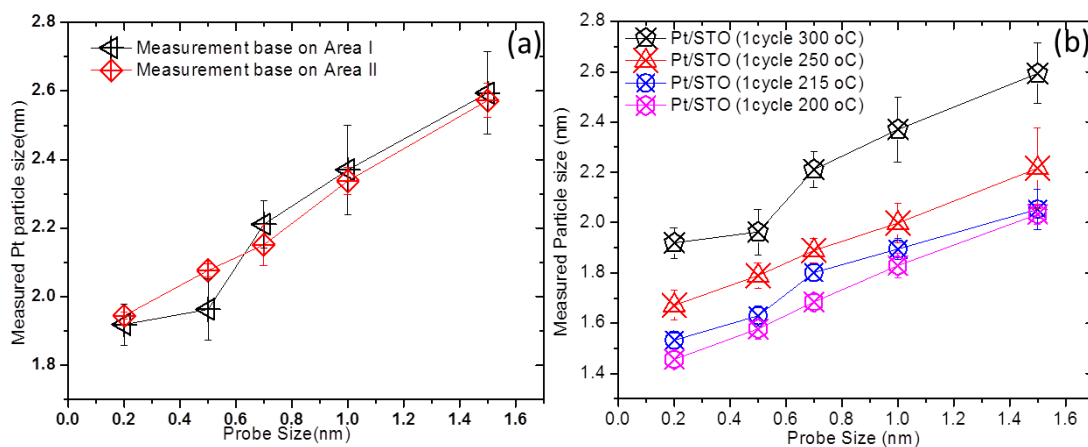


Figure 4.6. Measured nanoparticle size as a function of used electron probe size based on different samples (a) Pt/STO-NCs 1 cycle 300 °C (b) Series of Pt/STO-NCs synthesis with 1 cycle at different reaction temperature.

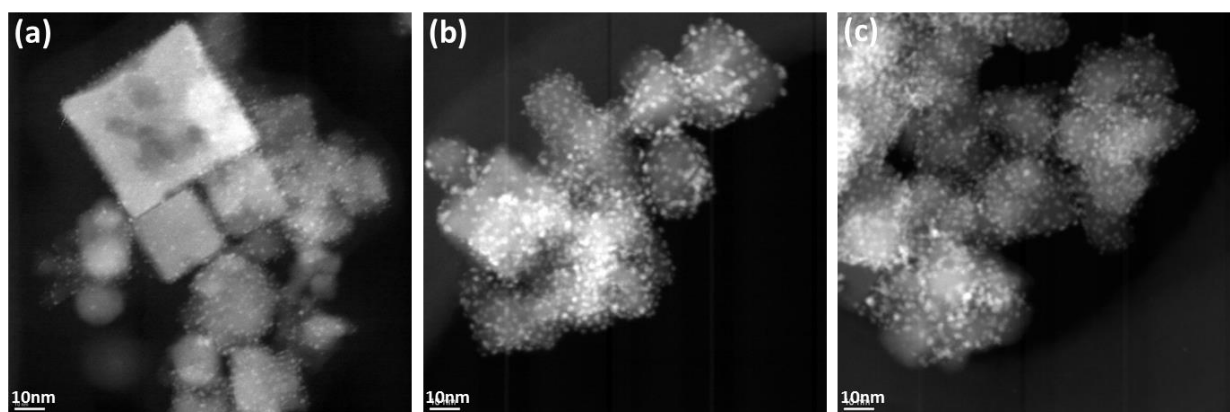


Figure 4.7. HAADF images of Pt/STO-NCs(OA) synthesized under reaction temperatures of (a) 200 °C (b) 250 °C (c) 300 °C.

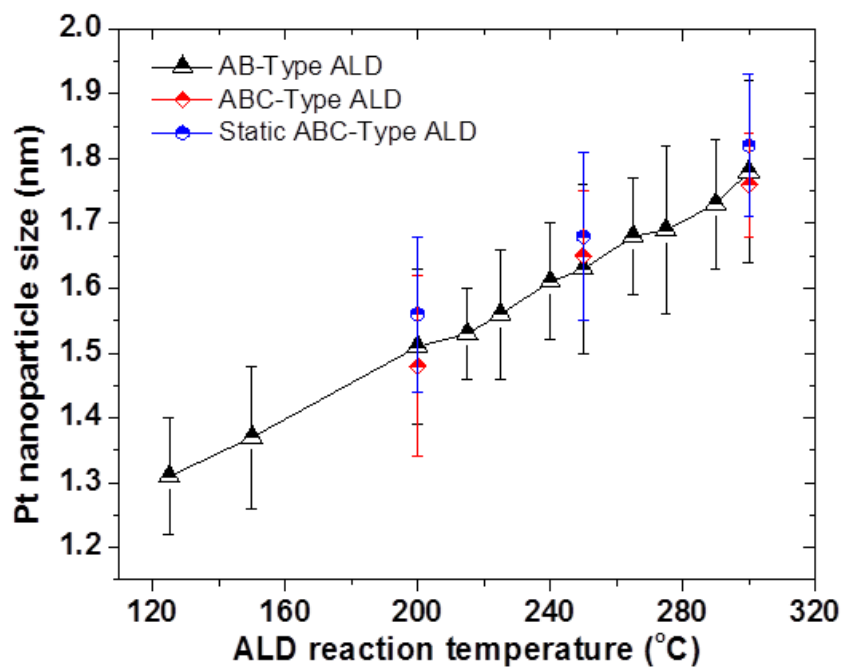


Figure 4.8. Pt particle size plotted as a function of ALD reaction temperature.

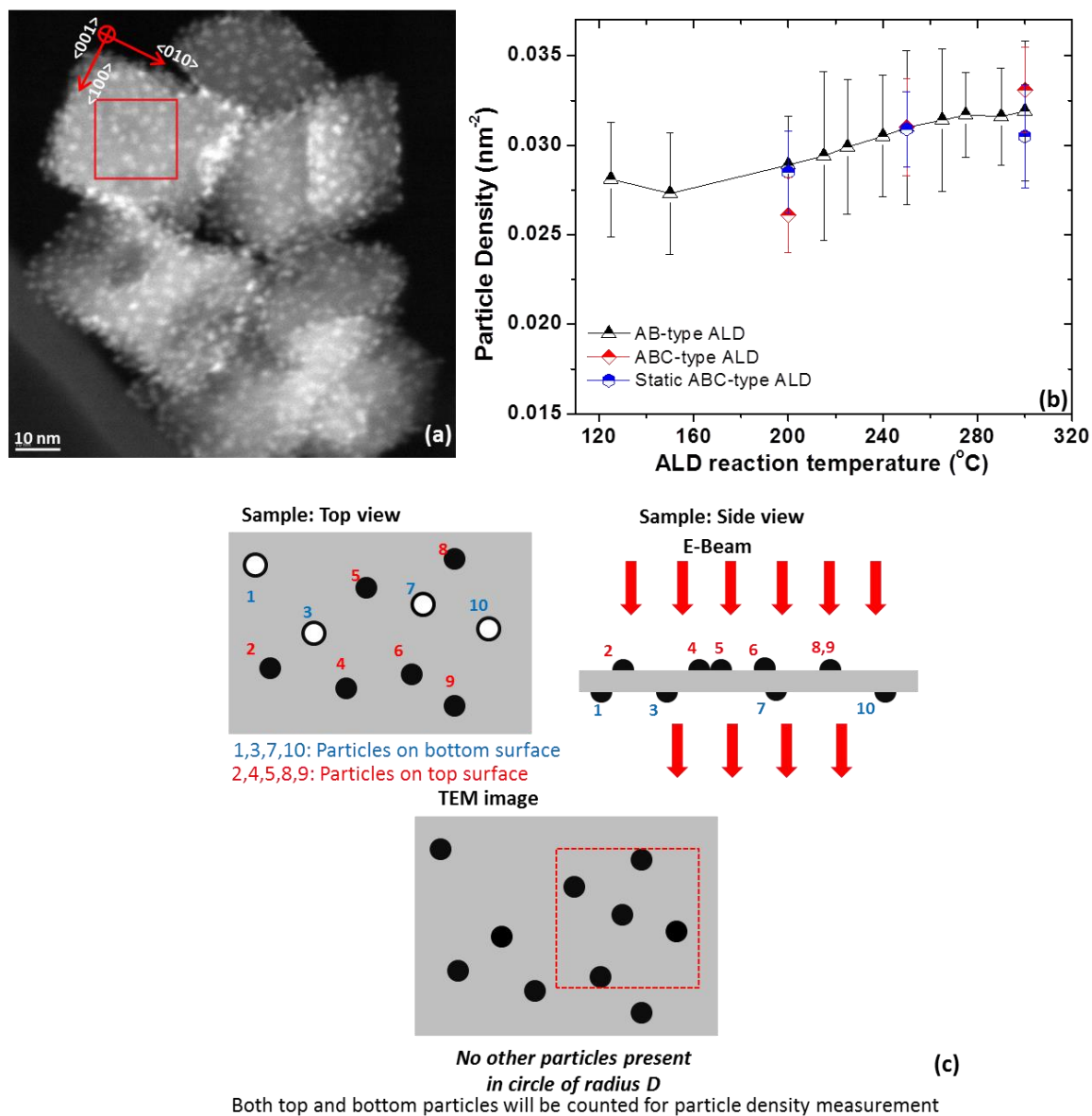


Figure 4.9. (a) Diagram shows definition of particle density, the image is HAADF image of Pt/STO-NCs (oleic acid) synthesized with 1 cycle AB type ALD at 300 $^{\circ}\text{C}$. (b) Pt particle density as a function of ALD reaction temperature. (c) Diagram illustrates that particles from both top and bottom surface will contribute the particle density measurement.

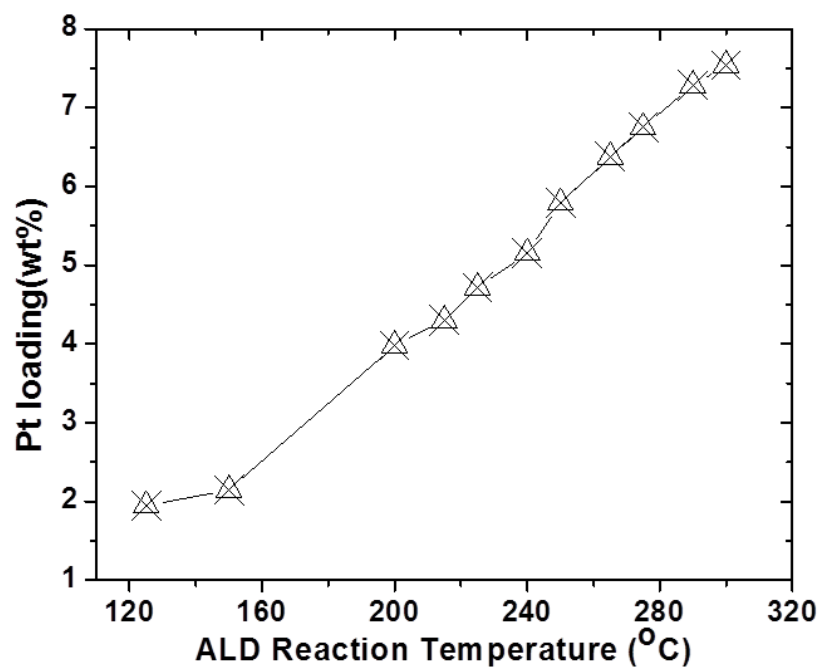


Figure 4.10. Pt weight loading as a function of ALD reaction temperature.

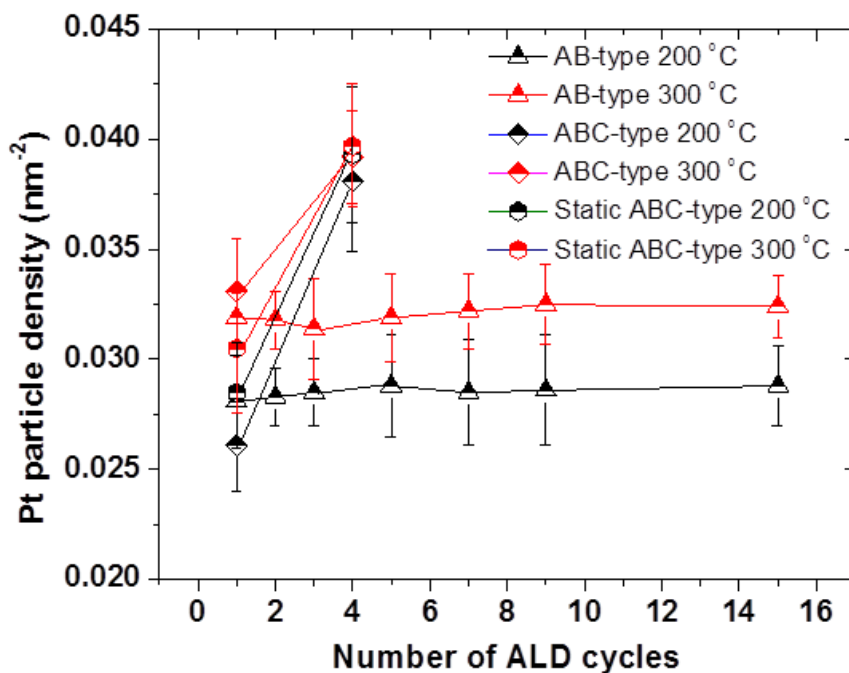


Figure 4.11. Pt particle density as a function of commenced number of ALD cycle under two different ALD reaction temperatures of 200 °C and 300 °C.

Table 4.2. Dependence of size and density of Pt nanoparticles on number of cycle and ALD method under two reaction temperatures of 200 °C and 300 °C.

200 °C						
# of cycles	AB-type ALD		ABC-type ALD		Static ABC-type ALD	
	Size(nm)	Particle density(nm ⁻²)	Size(nm)	Particle density(nm ⁻²)	Size(nm)	Particle density(nm ⁻²)
1	1.51	0.0281	1.48	0.0261	1.56	0.0285
4	N.A.	N.A.	1.51	0.0381	1.63	0.0393
5	1.80	0.0297	N.A.	N.A.	N.A.	N.A.
300 °C						
1	1.78	0.0319	1.76	0.0331	1.82	0.0305
4	N.A.	N.A.	1.83	0.0392	1.91	0.0397
5	2.25	0.0297	N.A.	N.A.	N.A.	N.A.

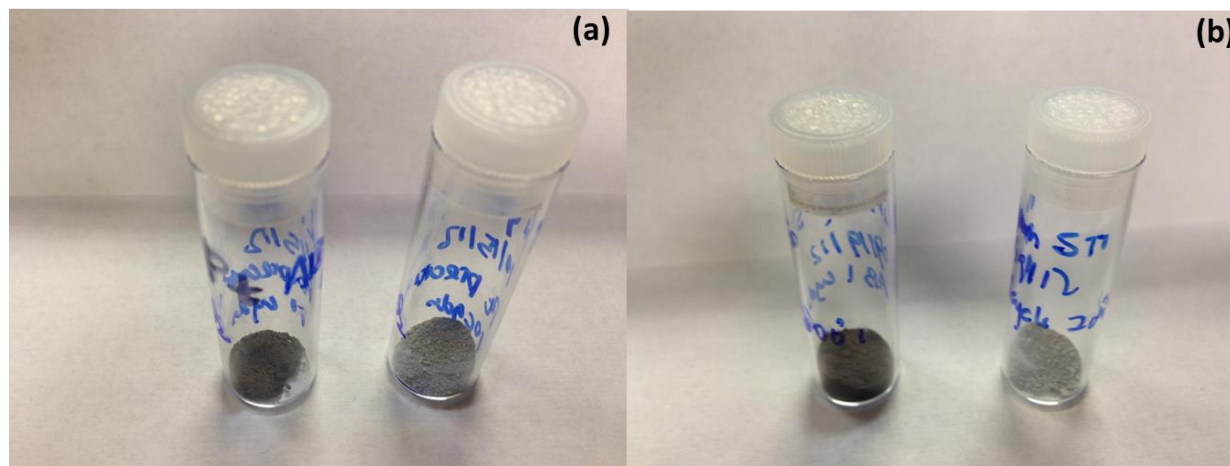


Figure 4.12. Images of Pt/STO-NCs synthesized using (a) MeCpPtMe₃ and H₂O (b) MeCpPtMe₃ and O₂. In each image, left and right sample are Pt deposited on oleic acid and acetic acid synthesized STO-NCs respectively.

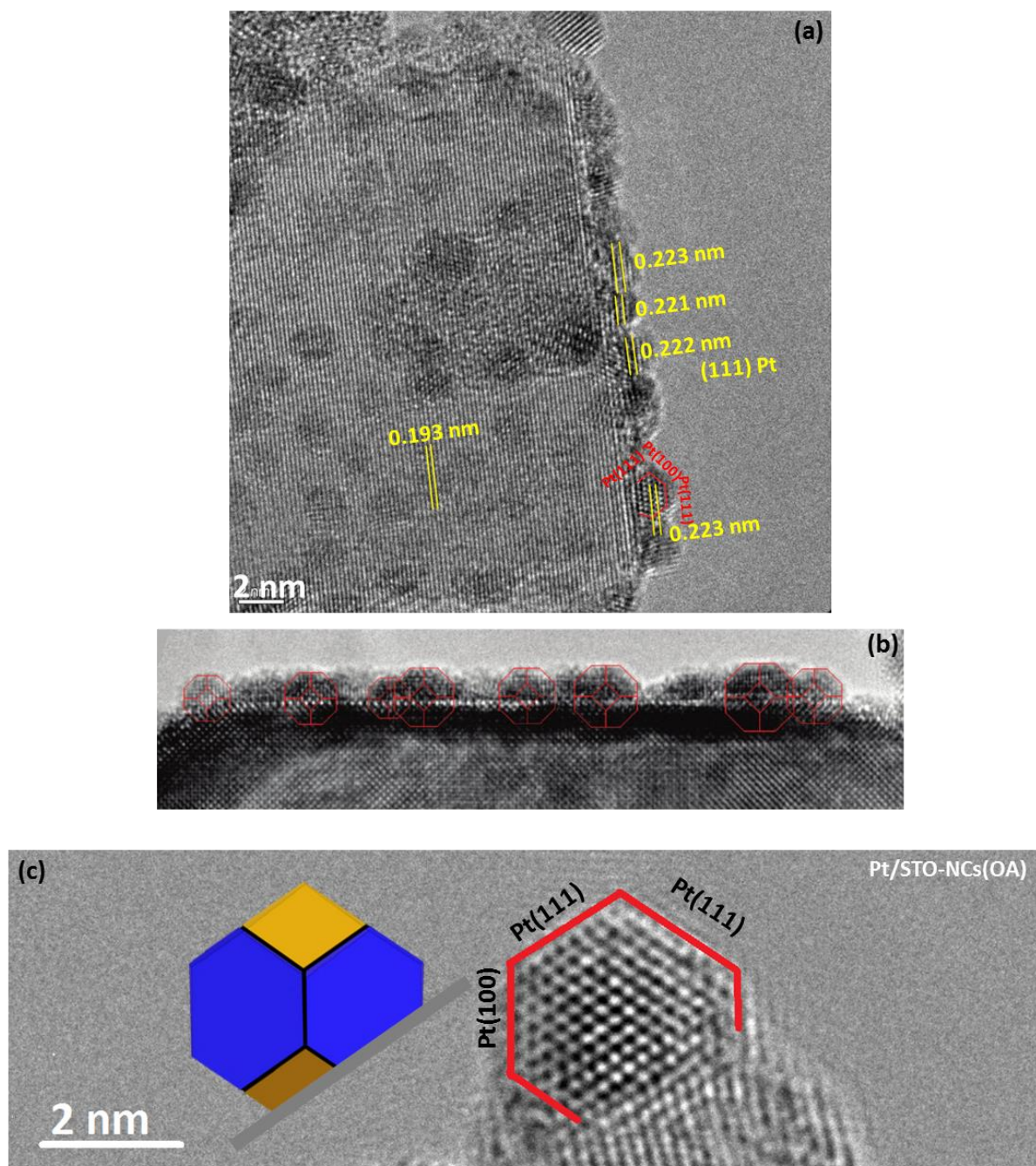


Figure 4.13. HREM image of Pt on (a) STO-NCs (OA) obtained by 10 cycles traditional ALD at 200 °C. (b) STO-NCs (AA)

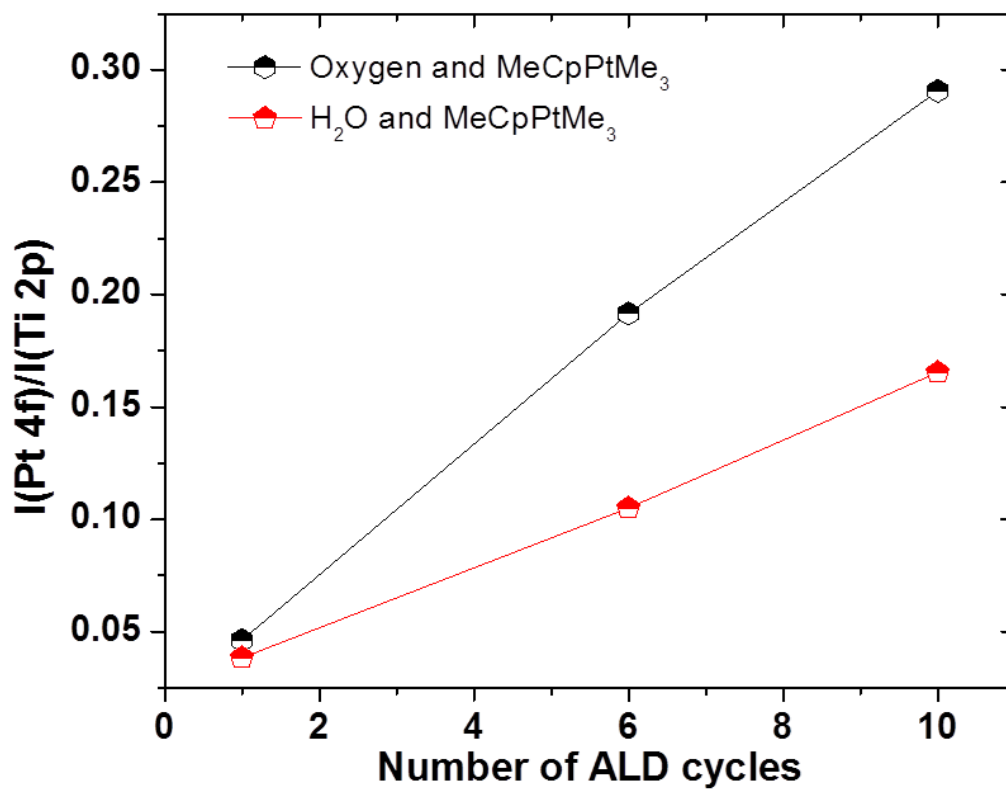


Figure 4.14. XPS studied Pt 4f/Ti 2p ratio synthesized using oxygen and water as a function a deposition cycles.

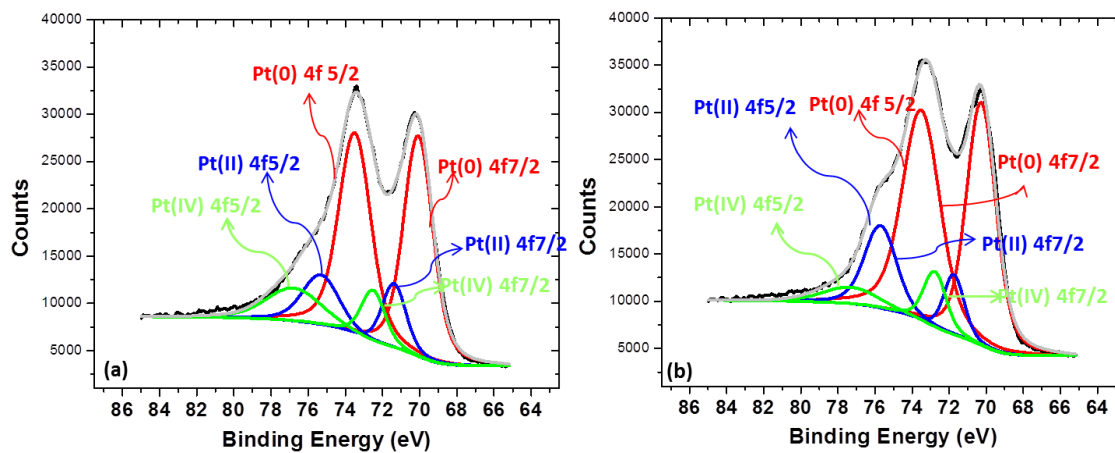


Figure 4.15. XPS Pt 4f spectroscopy of Pt/STO-NCs (Oleic Acid) deposited with 6 cycles AB type ALD at 250 °C (a) oxygen (b) H₂O.

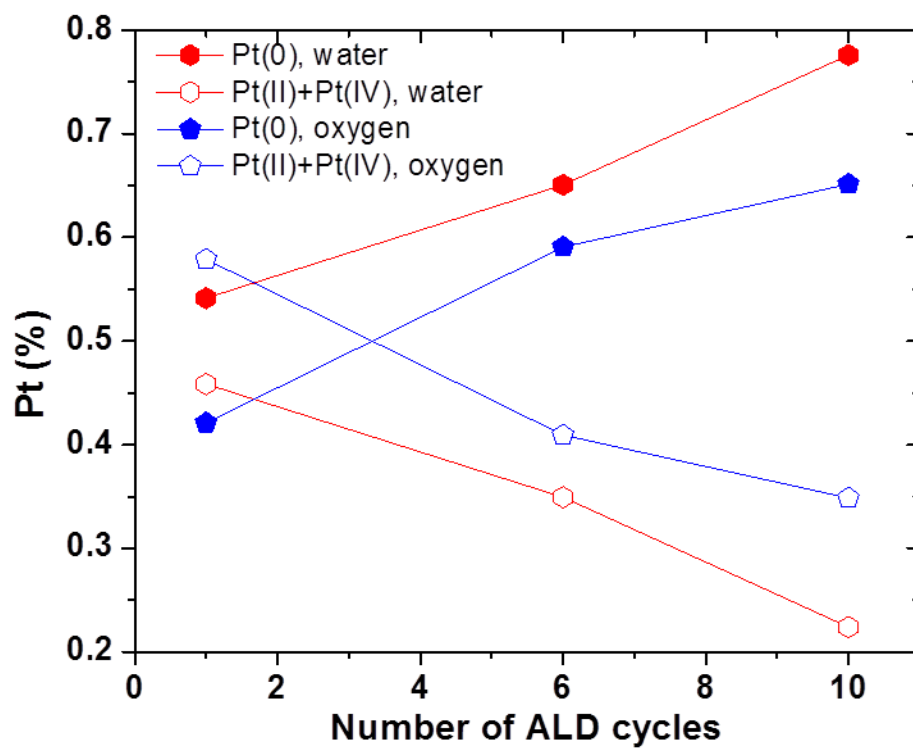


Figure 4.16. Pt(0) and Pt(II)+Pt(IV) percentage of Pt/STO-NCs deposited using water and oxygen as a function of number of ALD cycles.

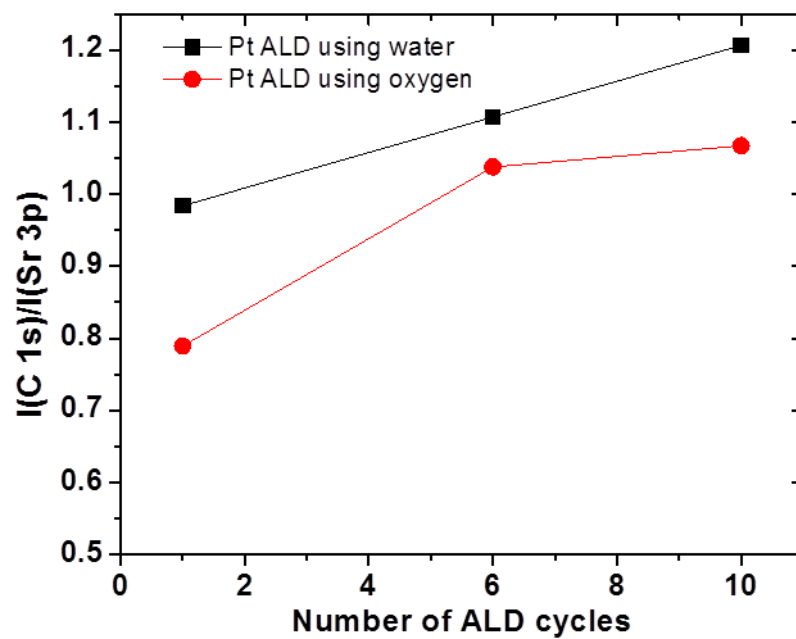


Figure 4.17. XPS I(C 1s)/I(Sr 3p) ratio of Pt/STO-NCs prepared using water and oxygen as B reagent.

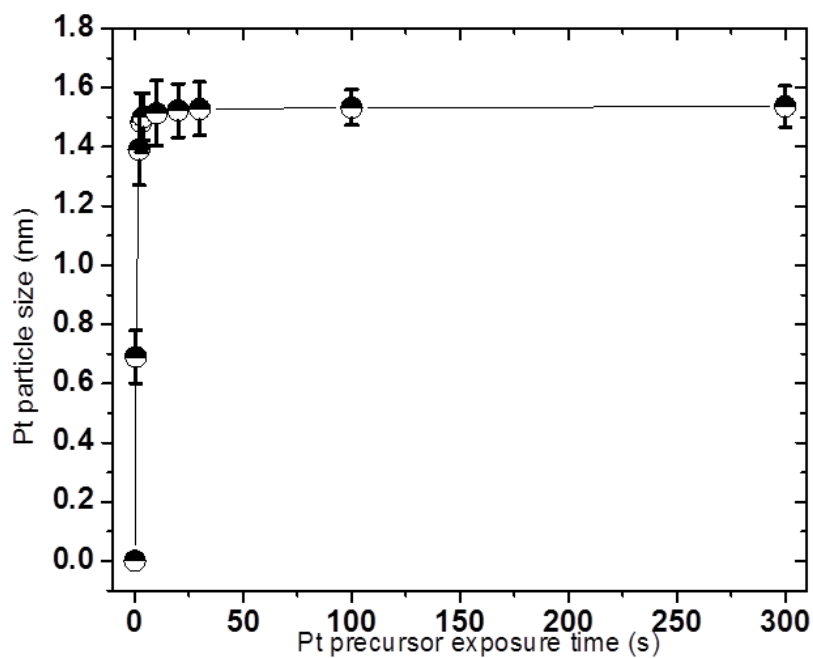


Figure 4.18. Measured Pt particle size depends on Pt precursor dosing time based on HAADF image measurement.

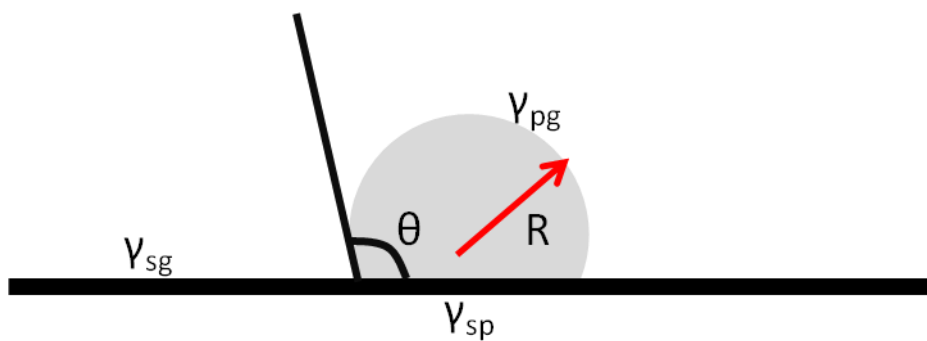


Figure 4.19. Schematic of nucleation process of a new phase on an substrates, γ_{pg} , γ_{sg} , γ_{sp} is interfacial energy between Pt-Gas, substrate-gas, substrate-Pt.

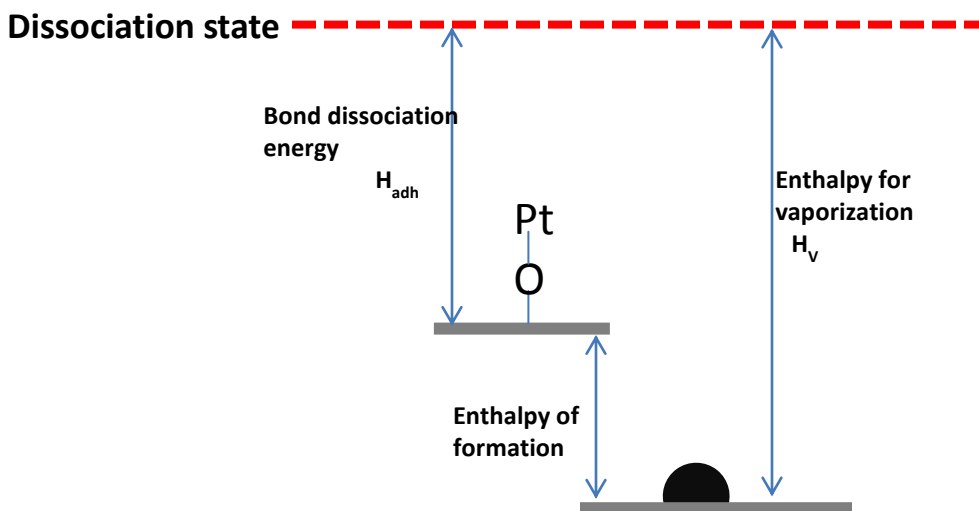


Figure 4.20. Diagram showing enthalpy of formation. Pt-O-X-STO is the Pt configuration after Pt precursor adsorption and ligands elimination.

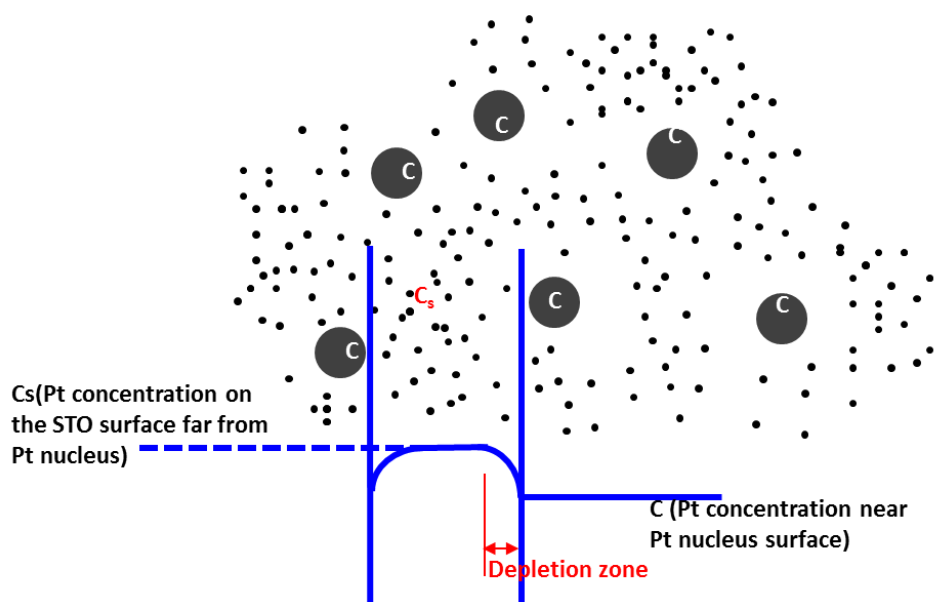


Figure 4.21. Schematic diagram showing the formation of a depletion boundary after nucleation during Pt ALD process.

Table 4.3. Migration Distance (300s) of single Pt atom on STO-NCs substrate under different reaction temperature

Reaction Temperature (°C)	Dp (nm ² /s)	Migration Distance (nm)
125	0.02	5.07
150	0.15	13.29
200	3.76	67.21
215	8.75	102.45
225	14.91	133.78
240	31.94	195.78
250	51.80	249.32
265	103.43	352.30
275	160.59	438.98
290	301.71	601.71
300	451.03	735.69

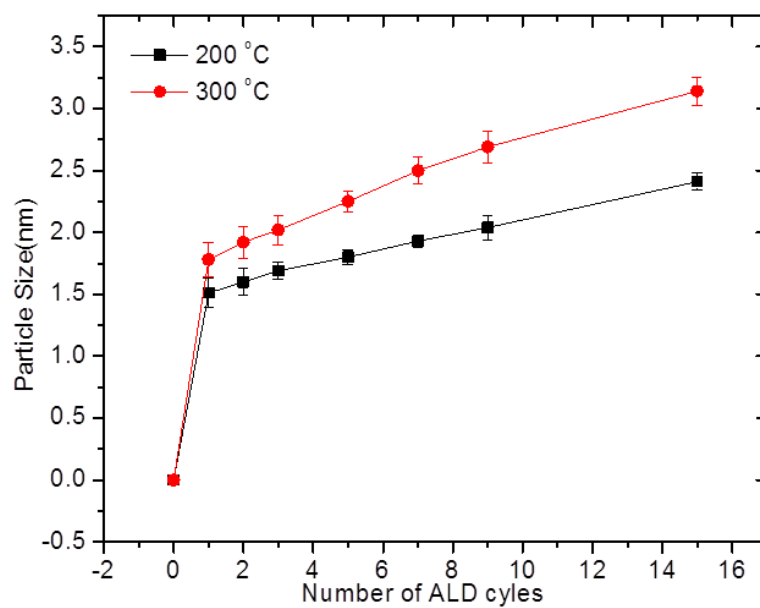


Figure 4.22. Pt particle size as a function of commenced number of ALD cycles measured based on HAADF image.

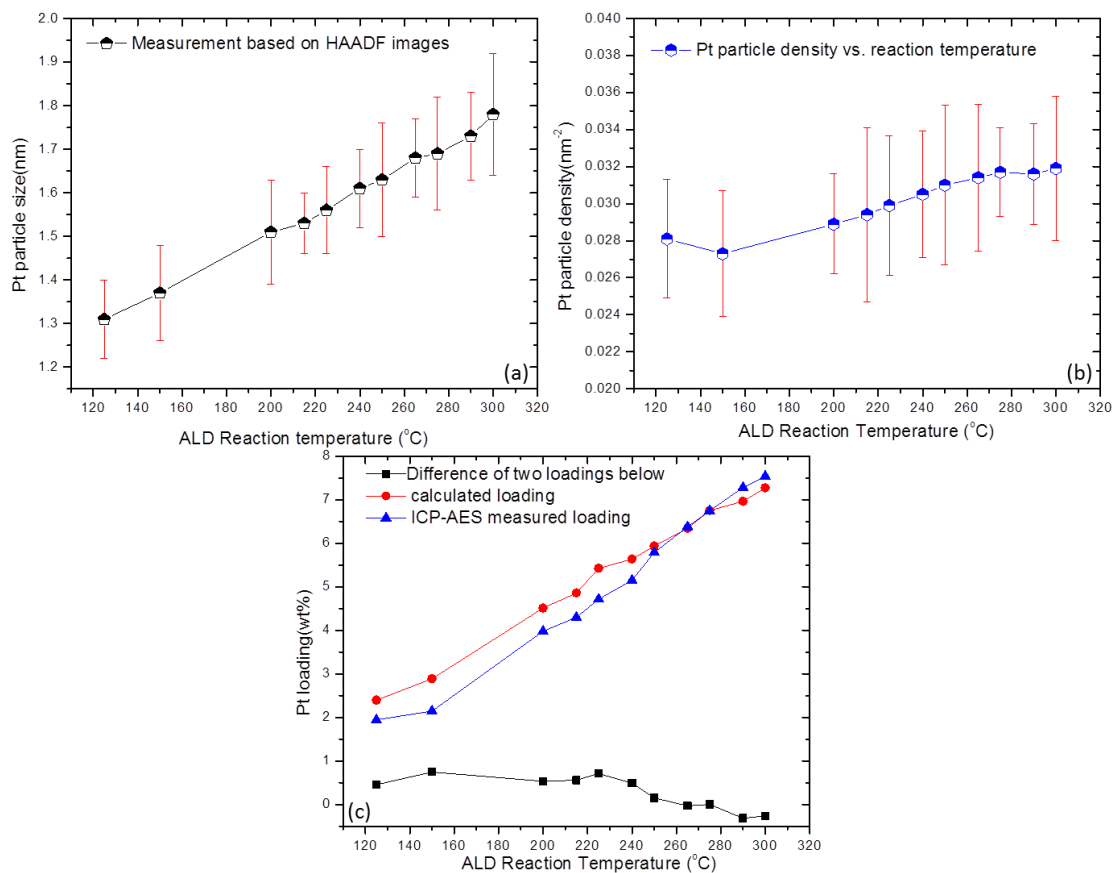


Figure 4.23. Platinum (a) particle size (b) Particle density as a function of ALD reaction temperature after single cycle synthesis. (c) Pt weight loading as a function of ALD reaction temperature. The black curve shows the difference between calculated and ICP-AES measured loading.

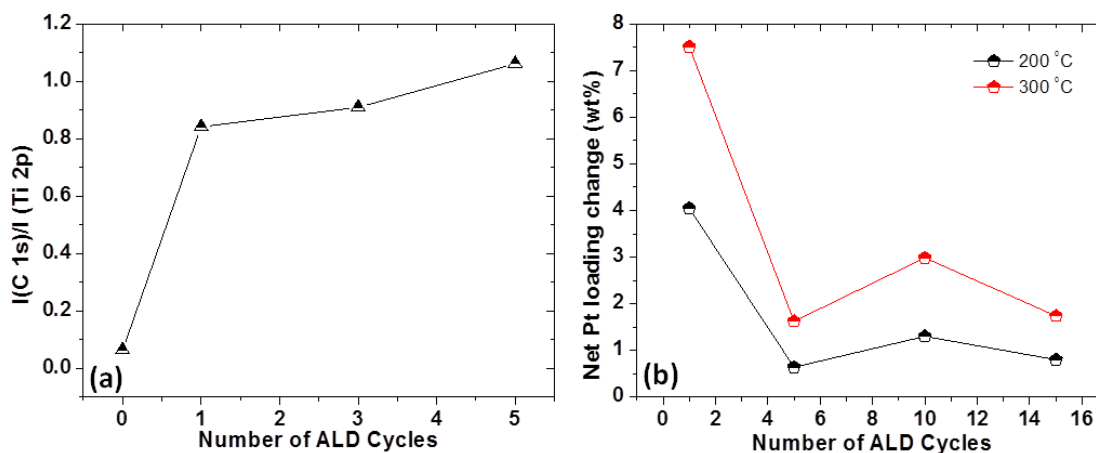


Figure 4.24. (a) C1s/Ti2p ratio from XPS data of Pt/STO-NCs deposited with different number ALD cycle. (b) ICP-AES measured net Pt loading change during a specific cycle.

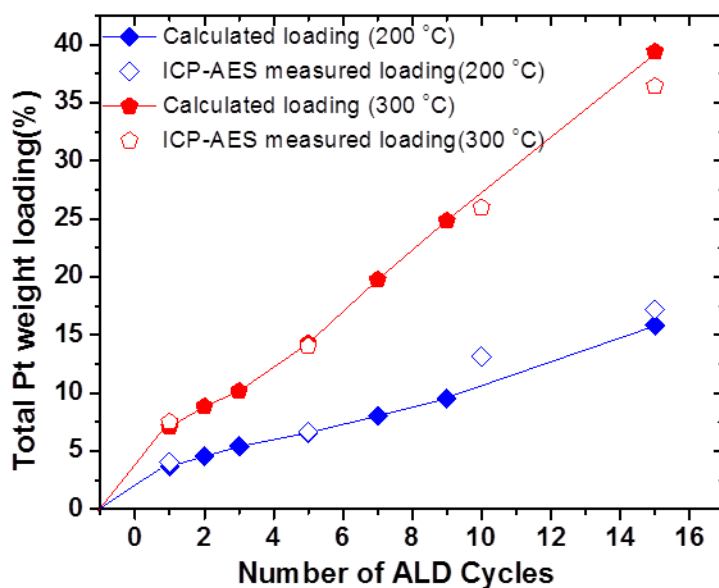


Figure 4.25. Pt loading as a function of number of ALD cycles at 200 °C and 300 °C from ICP-AES measurement. For comparison particle loading measured from HAADF is included.

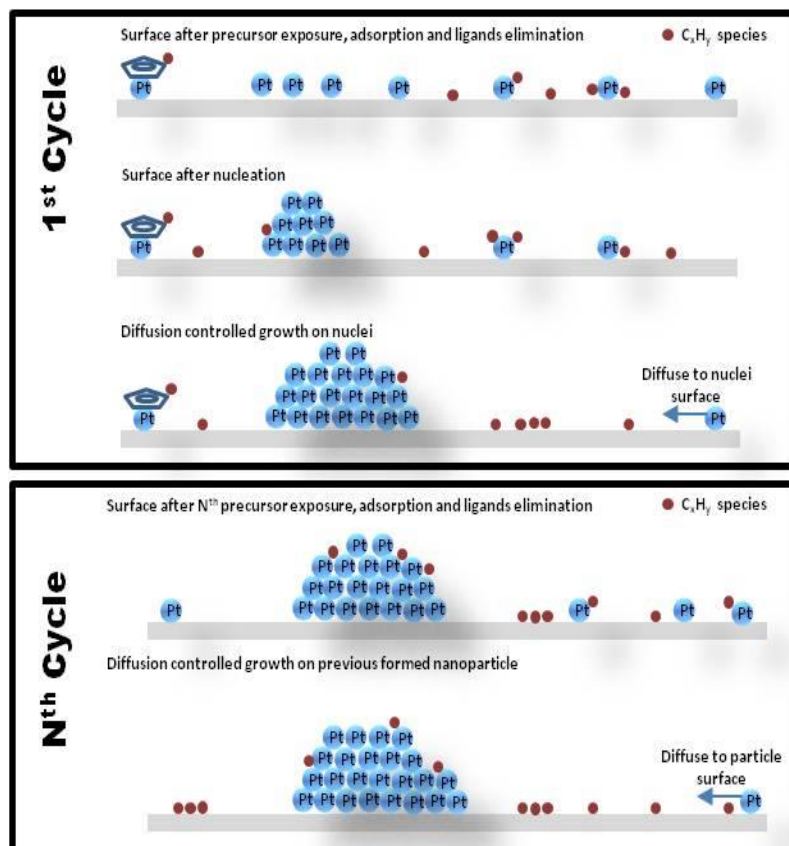


Figure 4.26. Schematic representation of Pt particle formation on oxide surface for 1st ALD and multiple cycles synthesis.

Chapter V:

**Winterbottom Shape Tailoring of Platinum Nanoparticles
on Perovskite Oxides $\text{Ba}_x\text{Sr}_y\text{TiO}_3$**

5.1. Introduction

For past decades, there has been an increased interest of perovskite oxides $Ba_xSr_yTiO_3$ ($x + y = 1$) because their scientific importance and widespread applications in electronics[183, 184], sensing[185, 186] and nonlinear optics[187-189], among which STO and BTO have been widely used as catalysts or catalyst supports, e.g. Enterkin J. A studied Pt/STO-NCs catalysts for hydrocarbon combustion of propane for automotive application, and indicates Pt nanoparticles on STO-NCs have a lower light off temperature, higher turn-over frequency and improved resistance to deactivation comparing to Pt/Al₂O₃. [190] Li et al. and Liao et al. successfully applied Ni based catalyst supported on BTO for CO₂ reforming of CH₄ and reported higher reactivity was achieved by add proper amount of MgO. [191] While Sulaeman et al. mention photocatalytic activity of STiO₃ and performance of photo-oxidative destruction of NO_x under visible light irradiation could be highly enhanced by an increase in Sr/Ti atomic ratio [192] In order for establishment of structure-surface-chemistry relationships that are relevant to heterogeneous catalysis when these oxides are used as catalyst supports, an extensive array of ultrahigh vacuum surface science techniques has been employed to understand, characterize and tailor the composition and atomic structure of these single oxides. [106, 193-199] However, the almost negligible surface area of these flat, nonporous single crystals, render difficult of practical catalytic application. This problem can be overcome by employing the preparation of oxide nanoparticles with controlled size, shape and exposed surface. [59, 200-202] Shape and exposed surface control of these nanocrystals is particularly important, as many of their physical and chemical properties are highly shape dependent, and the exposed surfaces determines the properties and possibility of the formation of functional nanostructures. The cubic or cuboids morphology is one of the best morphologies for the formation of a close-packed structure and

can provide larger interfaces between the contacted nanoparticles than other morphologies. More important, the cubic or cuboids shape allow the previous knowledge of single crystal surfaces to be directly applied to the understanding of support surfaces and the interface between catalyst and support.

With Sr totally replaced Ba in a perovskite structure of $\text{Ba}_x\text{Sr}_y\text{TiO}_3$, the unit cell decreases from 4.034 Å (BTO) to 3.905 Å (STO) while the substitution doesn't change their cubic structure.[203] More important, related properties such as band gap, surface free energy also shows difference with the substitution, e.g. BTO (100) surface has a band gap of 3.18 eV[204] and surface energy of $0.073 \text{ eV}/\text{Å}^2$ while STO (100) surface with a band gap of 3.75 eV[205] and surface energy of $0.090 \text{ eV}/\text{Å}^2$. The differences caused by ion substitution will also benefit us for engineering and tailoring new material deposited on these substrates, e.g. atomic layer deposition of metal nanoparticles might have different thermal dynamical Winter-bottom shape due to different interface energy.[45] In this Chapter, we present and discuss the results of platinum nanoparticles grown on BTO and STO substrates using ALD deposition. The difference in morphology (e.g. shape, size) of deposited Pt nanoparticles on such two types of substrates will be discussed in details. For our knowledge, this is first time Pt/BTO-NCs system has been studied. As will be discussed, the shape of platinum nanoparticles on these substrates is a thermodynamically stable. As such, we can expect this stable configuration to survive the rigors of catalytic condition for extended periods of time when these systems are using as catalysts. In effect we have engineered specific surfaces of the nanoparticles by controlling the shape of these particles with engineering of the support. This concept is general. In this chapter, methods are proposed through which this concept can be applied to create stable, predictable, face-determined catalysts.

5.2: Experimental

5.2.1 Substrates synthesis

The BTO or STO nanocuboids used in this work are synthesized following a sol-precipitation-hydrothermal treatment procedure same to that described in Chapter II.[59] All chemicals used here were of analytical grade and were used as received without further purification. More specific, 1.5 mmol $\text{Ti}(\text{O}i\text{Bu})_4$ was added to 52.5 mL ethanol and 7.5 mL oleic acid to form solution A, either 1.5 mmol $\text{Ba}(\text{Ac})_2$ (For BTO) or 1.5 mmol $\text{Sr}(\text{Ac})_2$ (For STO) in 15 mL water was used to form solution B depends on for BTO or STO synthesis, 1.2 g NaOH in 6mL water to form solution C. Solution B and C were successively added to solution A and mixed while stirring for a few minutes to form a solution of pH 13~14, and the resultant solution was sealed in a 125mL autoclave, then heated at 160 °C for 8hr.

5.2.2 Pt atomic Layer deposition

The Pt nanoparticles was deposited onto the STO-NCs (or BTO-NCs) using ALD as previously described. For this procedure, 15 mg of the STO-NCs (or BTO-NCs) were spread in a stainless steel tray which was covered by a stainless steel mesh to contain the powder while allowing easy access by the ALD precursors. Prior to ALD, all nanocuboids were pre-cleaned in situ using a 200 sccm flow of 10% ozone in oxygen at a temperature of 200 °C for 15 min. The Pt ALD was accomplished using alternating exposures to MeCpPtMe_3 (300 s) and H_2O (120 s) at different reaction temperature using a viscous flow ALD reactor with a constant 140 sccm flow of ultrahigh purity nitrogen (99.995%) carrier gas at a pressure of 1.0 torr. Nitrogen purge periods of 300 s were used between reactant exposures. A series of Pt/STO-NCs (or Pt/BTO-

NCs) samples were prepared using 1, 3, 5, 10 and 15 Pt ALD cycles over BTO-NCs (or STO-NCs). All power samples are carefully transferred to an analytical balance to measure the BTO mass before and after the Pt ALD in order to determine the Pt weight loading.

5.2.3 Pt nanoparticle characterization

HREM and images of BTO-NCs and STO-NCs were acquired before and after the Pt ALD using a JEOL JEM-2100F electron microscope operated at 200 kV. HAADF images are also recorded here for morphology study. The TEM samples were prepared by drying several drops of ethanol dispersed Pt/STO sample on the surface of a carbon film supported on a copper grid.

5.3: Results and discussion

5.3.1 General morphology and structure of BTO-NCs and STO-NCs

TEM images of the STO-NCs and BTO-NCs reveal general cuboids morphology, Figure 5.1. High concentration of these nanocuboids on copper grids shows single layer self-assembly arrays, Figure 5.1a (top row). Self-assembly of these particles is a natural and spontaneous process occurring mainly through interactions such as van der Waals, hydrogen bonding, hydrophilic/hydrophobic, electrostatic and metal-ligand coordination networks.[206, 207] Figure 5.1 also indicates that all nanocuboids are with high uniformity and with an average length/width aspect ratio of ~ 1.08 and ~ 1.40 respectively for BTO-NCs and STO-NCs. Both as-prepared STO-NCs and BTO-NCs have many excellent properties to be used as a catalysts support. As shown in Figure 5.2, these nanocuboids are nonporous, single crystalline with (100) facet mainly exposed and a narrow size distribution around 10 nm (BTO-NCs) and 20nm (STO-NCs).

5.3.2 Platinum nanoparticles deposited on BTO-NCs and STO-NCs

HAADF-STEM image showed that well dispersed platinum nanoparticles with uniform size distribution were formed both on STO-NCs and BTO-NCs, Figure 5.3a. Evolution in size of deposited Pt nanoparticles upon commenced number of ALD cycles is shown in Figure 5.3b, which behaviors similarly on two different substrates but with Pt deposited on STO slight larger than those deposited on STO. From HAADF image the platinum particles appear approximately circular and one cannot obtain directly information about their internal or external structure. In high-resolution imaging (Figure 5.4) of Pt nanoparticles on STO (Figure 5.4a) and BTO (Figure 5.4b), the Pt nanoparticle can be differentiated from lattice fringes of both Pt and STO-NCs (or BTO-NCs), which shows that the particles are metallic Pt with the lattice fringes of the platinum nanoparticles aligned with those of the strontium titanate or barium titanate. The (110) lattice fringe of STO (0.271 nm) and BTO (0.283 nm) are readily resolved. A lattice fringe mismatch was found on both types of substrate which suggests the growth of Pt on these two substrates is not epitaxy. The mismatch appears more frequently between Pt and BTO-NCs than STO-NCs. This is not surprising, as a lattice mismatch between Pt and STO (3.920 Å for Pt and 3.905 Å for STO) is only 0.4% comparing to 2.9% between Pt and BTO (4.034 Å for Barium titanate). The lattice fringes analysis indicates platinum nanoparticle grow in a direction mixed of $\langle 100 \rangle$ and $\langle 111 \rangle$ for both types of substrate, which implies that the STO-NCs were SrO terminated and BTO were BaO terminated instead of TiO_2 . [105]

5.3.3 Morphology and shape of platinum nanoparticles on BTO-NCs and STO-NCs

High-resolution imaging in Figure 5.5 shows the external shape of Pt deposited on two types of substrates, both of which has two types of low index (100) and (111) surface exposed.

The shape of the platinum particles on a substrate can be predicted by Winterbottom construction[163], a construction modified from Wulff construction.[64] The basis of Wulff construction theorem is that for a given volume, the equilibrium shape must be determined by minimizing the total surface free energy. The ensuing theorem states that the ratio between the real-space distance d_i from the cluster center to the facet plane i and the surface energy γ_i of this facet is a constant:

$$\frac{d_i}{\gamma_i} = c(\text{constant}) \quad (1)$$

This equation also states the length of a vector normal to a crystal face which connects that face with the origin is proportional to the surface free energy per unit area of that crystal face. As shown in Figure 5.6, varies in surface free energy ratio of exposed surface will change exposed surface ratio in a Wulff shape.

If the metal cluster is formed on a substrate, a metal-substrates interface is created. The free energy of the interface is given by the Young-Dupre equation[208]:

$$\gamma_{\text{interface}} = \gamma_{\text{substrates}} + \gamma_{\text{metal}} - \gamma_{\text{adh}} \quad (2)$$

Where $\gamma_{\text{interface}}$ is the interface energy, γ_{metal} , $\gamma_{\text{substrate}}$ is the free energy of the contact facet of the metal cluster and substrate, respectively. The equilibrium shape of a supported cluster can now found using a modified Wulff construction scheme, which is Winterbottom construction. We replace the free energy of the surface in contact with the substrate by an effective surface free energy γ' , which is the difference between the interface energy and the surface energy of the substrates:

$$\gamma' = \gamma_{\text{interface}} - \gamma_{\text{substrate}} \quad (3)$$

Then the height H of the supported cluster, relative to that of a free cluster will be determined by γ' . [163] For a cluster residing on a (111) facet (Fig. 5.7), the cluster will adopt its free-space form on the substrate if $\gamma' = \gamma_{metal}$. For smaller values of γ' the cluster gets truncated (Figure 5.7a), and for negative values of γ' , the height of the supported cluster becomes less than half the height of the free cluster, as illustrated in Figure 5.7b. The experimental value of the γ' can be derived from the observed, detailed morphology of the clusters in terms of the cluster surface energies using From Eqs. (2) and (3)

For Pt sit on either BTO or STO, the interface free energy is expressed as $\gamma_{interface} = \gamma_{STO(orBTO)} + \gamma_{Pt} - \gamma_{bond}$, where γ_{bond} is the free energy change per unit area associated with bonding across the interface, γ_{Pt} , $\gamma_{STO(orBTO)}$ is surface free energy of the relevant Pt face and STO (or BTO) substrates respectively. The Winterbottom shape of Pt which is truncated at certain position of a Wulff shape will be determined by $\gamma' = \gamma_{interface} - \gamma_{STO(orBTO)}$. The Pt shape with different $\gamma_{111} : \gamma_{100}$ ratio and γ' is shown Figure 5.8. Higher interface free energy and lower substrate free energy will cause less degree of truncation (Figure 5.8b). Upon discussion above, the shape of the Pt nanoparticles on STO (or BTO) is controlled generally by three factors: the interface free energy, the surface free energy of the support and the surface free energy ratio of exposed surface of Pt nanoparticles (e.g. $\gamma_{111} : \gamma_{100}$), changing these changes the ratio of exposed Pt (111) to Pt (100). The difference appears in shape of Pt nanoparticles supported on STO and BTO is the result of changing in these three parameters. A Winterbottom shape computing software developed by Zucker et. al., which relies on a new computational method to rapidly find equilibrium geometries, is used here to calculate the interface energy of Pt/BTO (or STO)

surface.[209] By given an experimental observation of the equilibrium shape with known exposed surface of a Pt particle, measuring the relative edge-lengths can be used to constrain the interface energy. Once all facet indices and orientation relationships are specified in the software, the interface energy sliders can be used to match the observed geometric parameters. Simulated shape presents in Figure 5.5 suggest that Pt/STO-NCs has a relative larger $\gamma_{interface} - \gamma_{STO}$ and $\gamma_{111}:\gamma_{100}$ ratio comparing to Pt/BTO-NCs. If we normalized all free energy with γ_{100} (e.g. $\gamma_{100}=1$), the simulation suggests $\gamma_{interface} - \gamma_{STO} = 0.6$, $\gamma_{111}:\gamma_{100} = 0.9$ for Pt nanoparticles sit on STO-NCs and $\gamma_{interface} - \gamma_{BTO} = 0.3$, $\gamma_{111}:\gamma_{100} = 0.84$ for Pt nanoparticles sit on BTO-NCs, which indicates smaller interfacial free energy between Pt and BTO surface caused by substituting Sr with Ba in a perovskite structure. In this work, all the analysis is confirmed by 5 measurements on different particles. The surface free energy ratio change of Pt (111) and Pt (100) on two substrates is potentially caused by adsorbed gas molecule or carbon contaminations.[210] The change of surface free energy due to these species can be expressed as,

$$\Delta\gamma = \frac{1}{A}(E_n^{ad} - E_n^{no-ad} - \frac{n}{2}E_{ad}) \quad (4)$$

Where E_n^{ad} and E_n^{no-ad} are the total energy of the system with and without the adsorption. E_{ad} is energy of single adsorbed molecules. A is the surface area occupied by these adsorbed molecules. As reported by Komanicky et. al., change of oxygen partial pressure will alter the exposed surface area apparently resulting in difference of Wulff shapes.[210]

5.4: Conclusion

Using TEM, we proved that Pt nanoparticles are successfully deposited on two types of perovskite nanocuboids with using atomic layer deposition. The morphology includes shape and size of deposited Pt particles shows difference on these types of substrates which is due to changing in substrates. As STO and BTO own different surface properties such as lattice spacing and surface free energy etc. Our analysis of platinum nanoparticles on STO-NCs and BTO-NCs has illuminated a method by which stable, high surface area, oriented catalysts can be created. Control of the support surface allows one to engineer such particles with precise control over what surface orientation is exposed, thus enabling precise modification of selectivity and yield for structure-sensitive catalytic reactions when used as catalyst. Such a method for controlling a nanoparticle catalyst surface can be applied to any catalytic system, not just platinum, and manipulated as discussed above while maintaining thermodynamic stability.

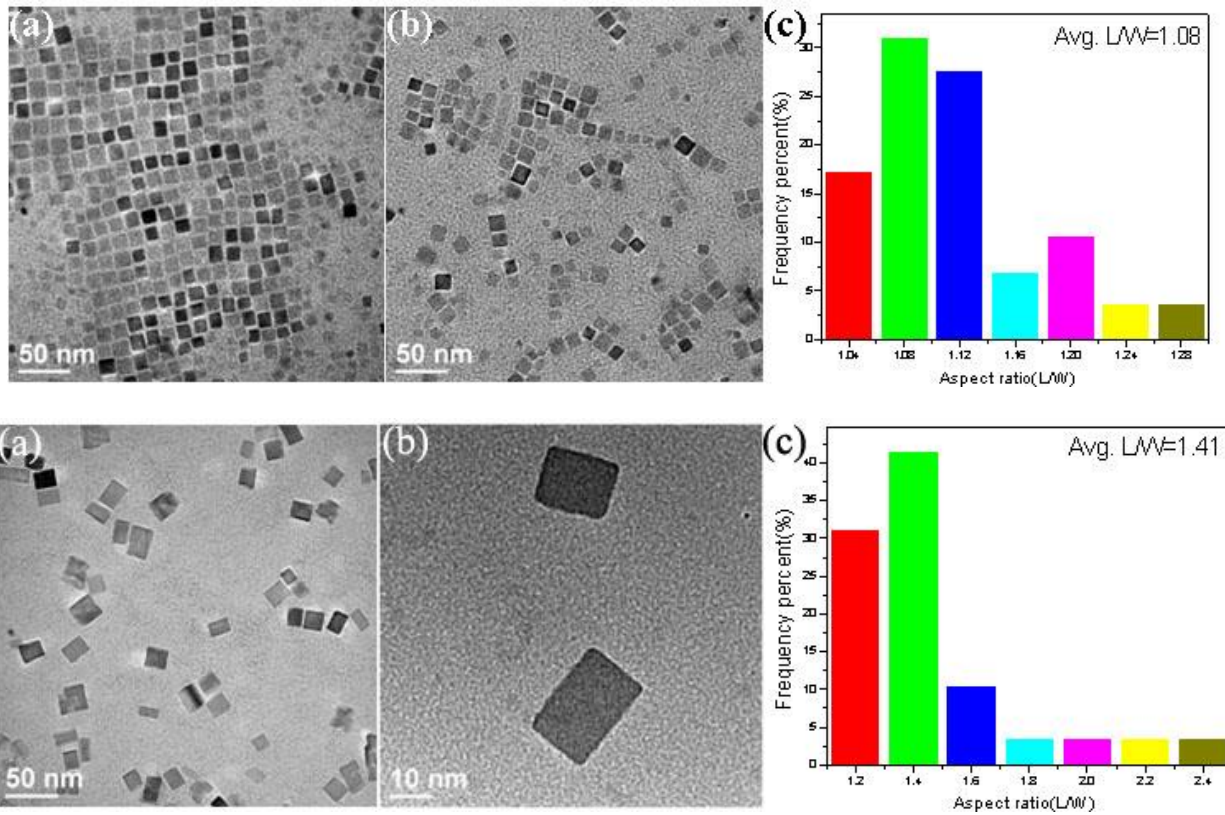


Figure 5.1. (a), (b) TEM images and (c) Aspect ratio (Length/Width: L/W) plots of BaTiO₃ (Top row) and SrTiO₃(bottom row).

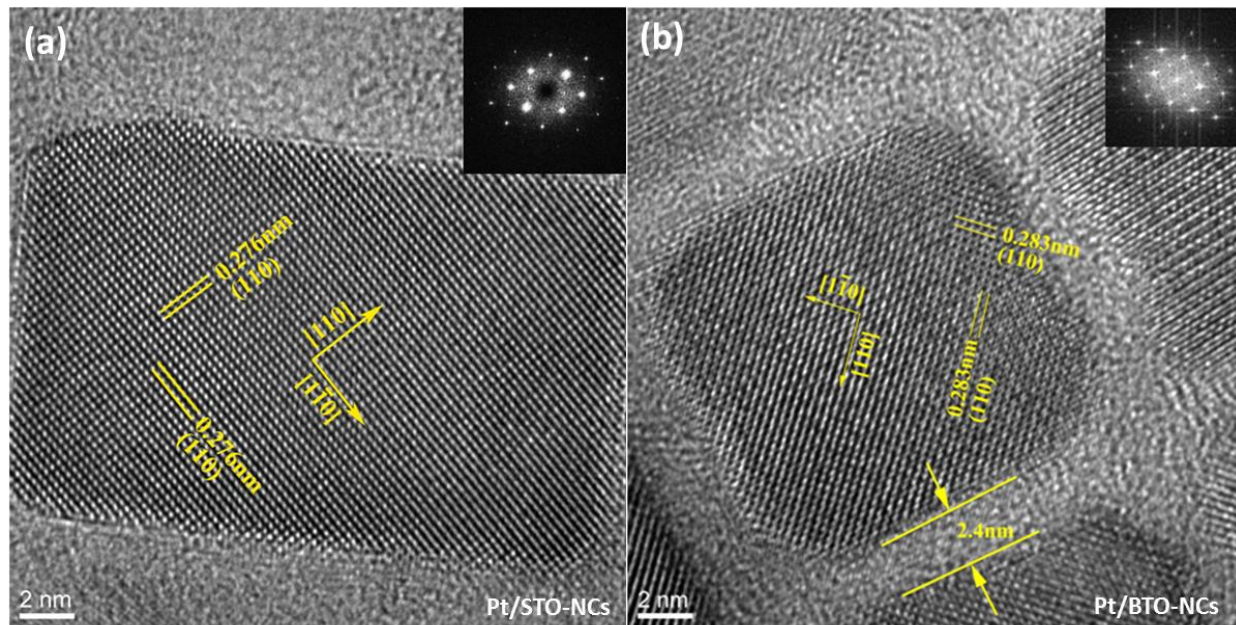


Figure 5.2. HRTEM images of (a) STO-NCs (b) BTO-NCs. The insert image is a live FFT image of corresponding HRTEM images.

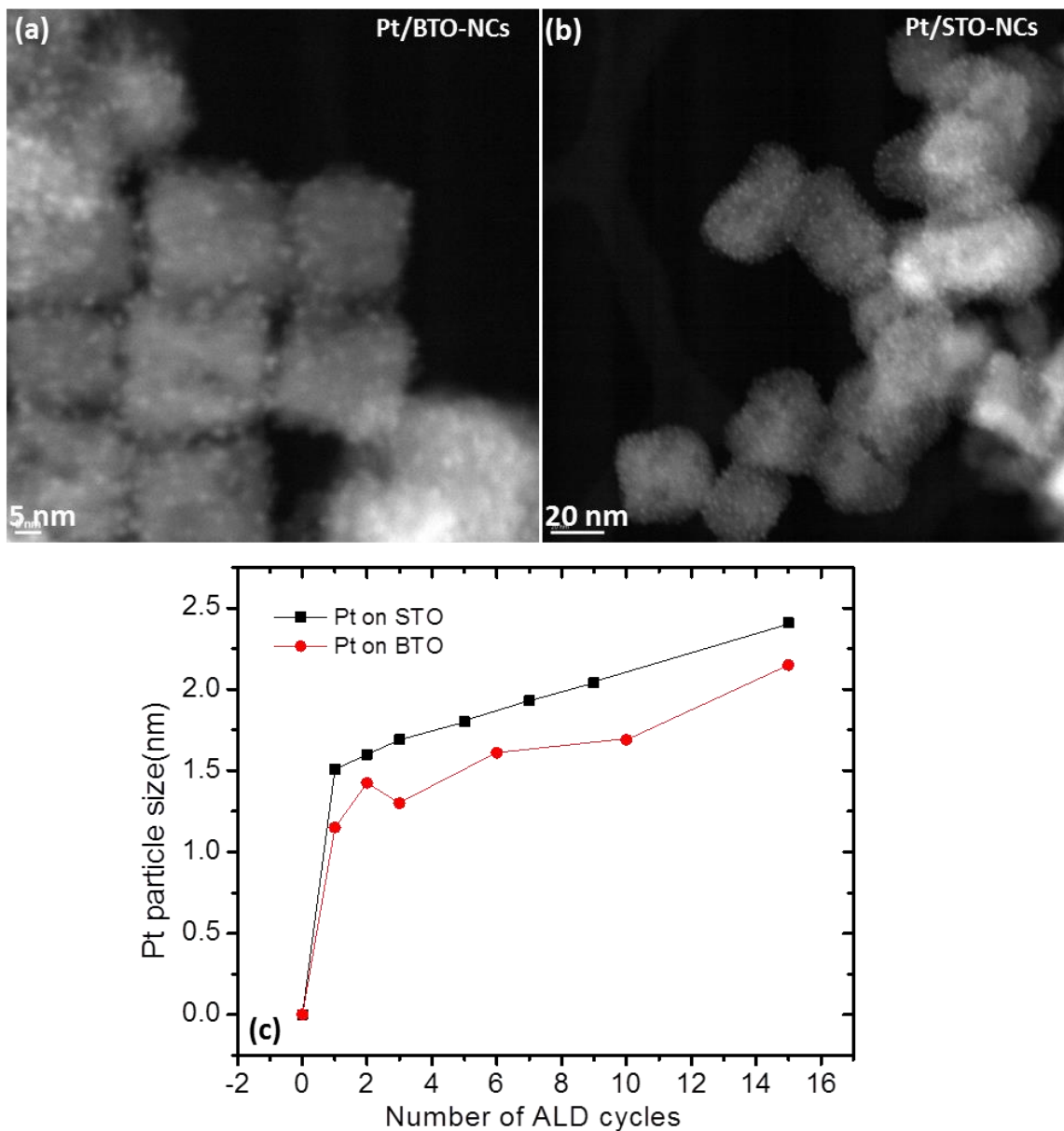


Figure 5.3. HAADF-STEM images of (a) Pt/BTO-NCs (b) Pt/STO-NCs. Both of which is deposition with 2 cycles of ALD at 250 °C. (c) Pt particle size as a function of commenced number of ALD cycles on STO-NCs and BTO-NCs substrates measured based on HAADF images.

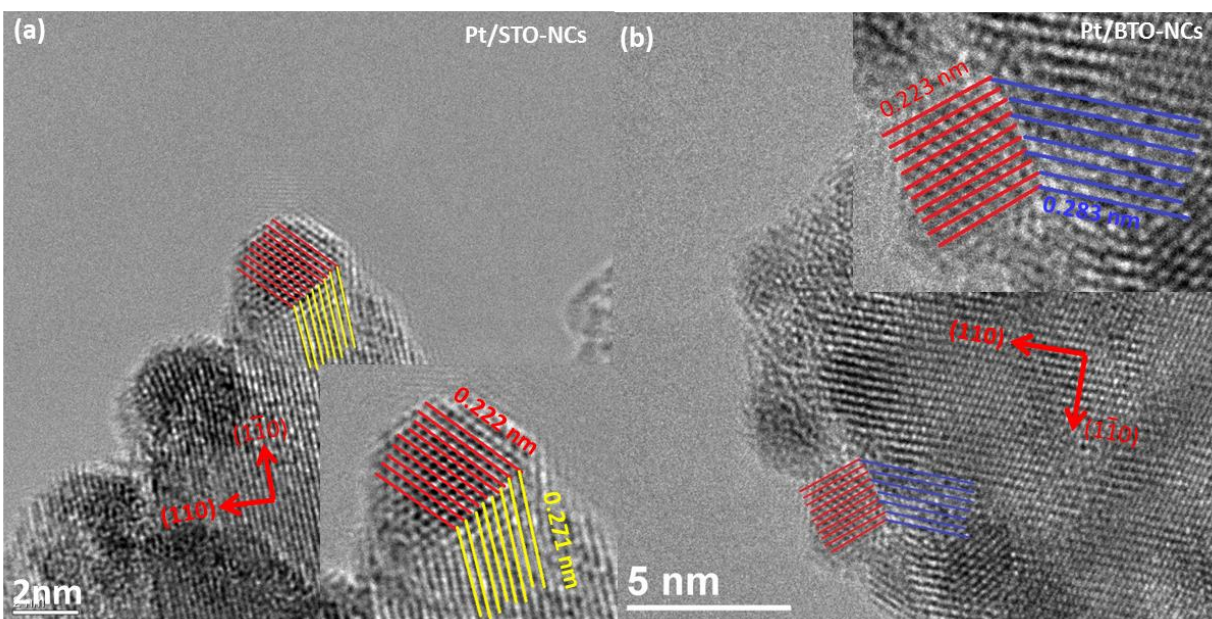


Figure 5.4. HRTEM images of (a) Pt/BTO-NCs, 3 cycles ALD at 200 °C (b) Pt/STO-NCs, 3 cycles ALD at 200 °C. The insert image shows a lattice fringe mismatch between substrates and deposited Pt nanoparticles.

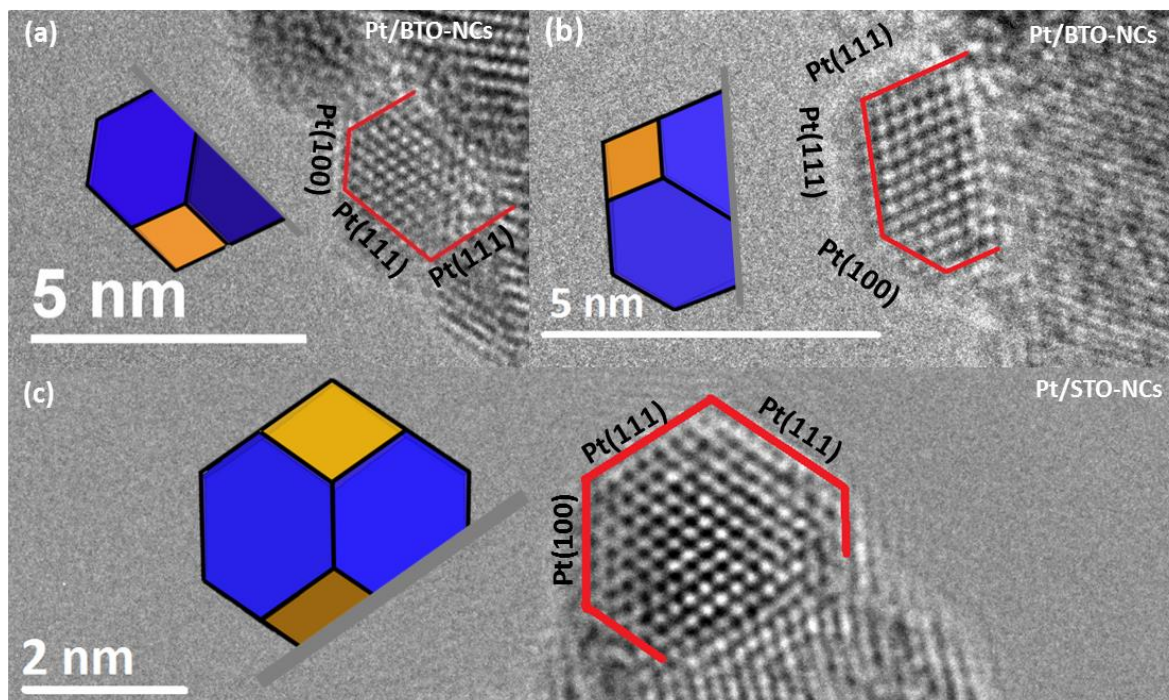


Figure 5.5. HRTEM images shows Winterbottom shape of Pt nanoparticle deposited on (a) (b) BTO-NCs (c) STO-NCs. A simulated Winterbottom shape is overlaid near the Pt nanoparticle.

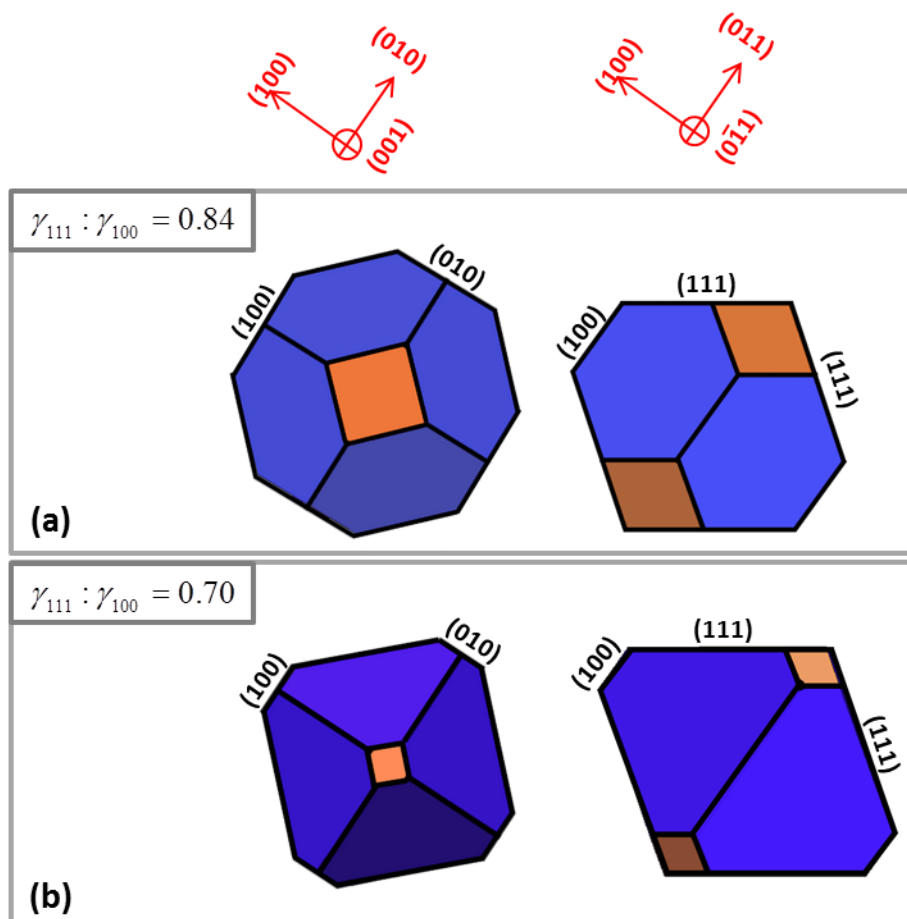


Figure 5.6. Wulff construction of a cluster with (100) and (111) surface exposed. Different ratio shows different shape (a) $\gamma_{111} : \gamma_{100} = 0.84$ (b) $\gamma_{111} : \gamma_{100} = 0.7$.

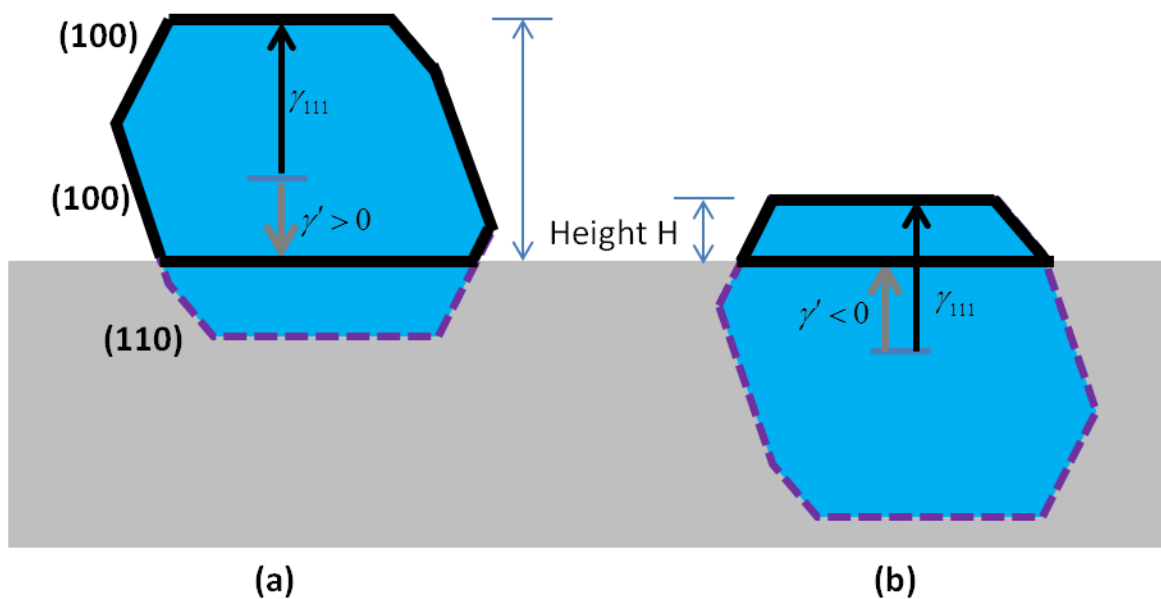


Figure 5.7. Cross section of a cluster supported on a (111) facet for a positive (a) and a negative (b) value of the effective surface energy γ' . H denotes the height of the cluster.

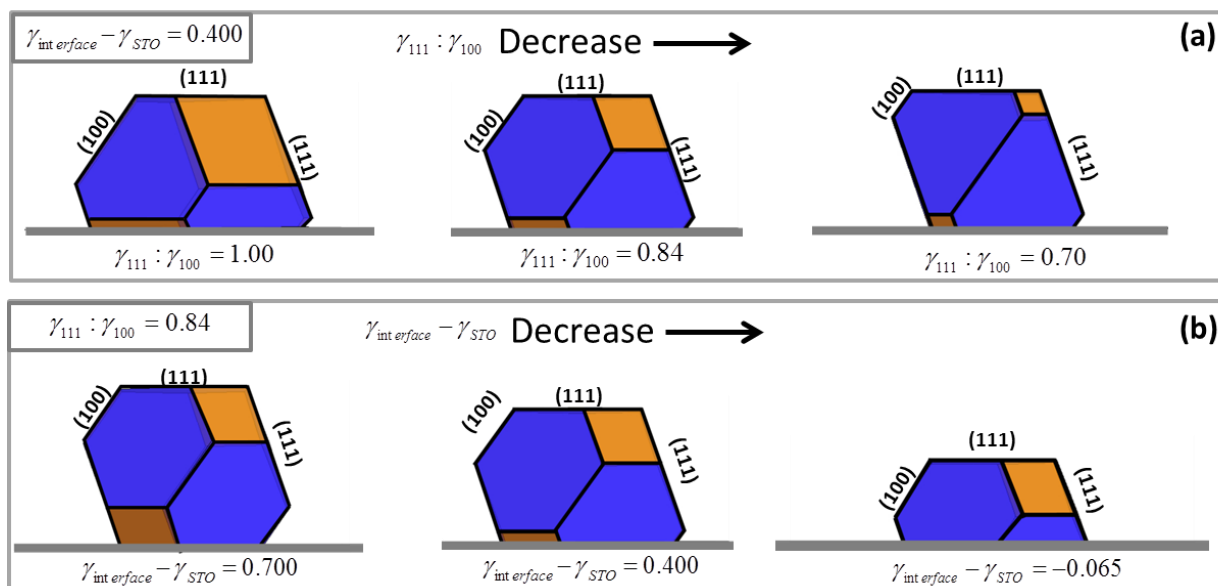


Figure 5.8. Winterbottom construction for Pt on a substrate (a) shows difference in Wulff shape caused by $\gamma_{111} : \gamma_{100}$ ratio. (b) shows different degree of truncation caused by difference in

$$\gamma_{\text{interface}} - \gamma_{\text{STO}}$$

Chapter VI:

**Platinum/Strontium Titanate-Nanocuboids System Towards
Catalytic Application**

6.1: Introduction

The catalytic oxidation of carbon monoxide to carbon dioxide over platinum group metals has been one of the most widely studied surface reactions since the classic work by Langmuir.[211] The relative simplicity of the process has made it a subject of extensive theoretical and experimental investigation.[212-215] Many features of this reaction have already been revealed, including that it proceeds via a Langmuir-Hinshelwood mechanism and is sensitive to the structure and shape of the catalysts.[216-218] Under certain conditions, the reaction shows an oscillatory behavior, hysteresis, and formation of CO₂ with excess translational and vibrational energy.[219-221] It has also been shown that the metal catalyst surface will undergo structural rearrangement (e.g. through sintering or shape transformation) when certain temperature and reactant pressure is satisfied.[222]

CO oxidation is not only of fundamental interest but also has industrial and atmospheric importance in the context of automotive emission control. This reaction takes place within catalytic converters and is one of the main generators of air pollutants and is expected to worsen as the demand for privately owned vehicles increase.[223-225] A large amount of emissions are released from a car during the first minutes after a “cold start” before the catalyst becomes hot enough to convert the harmful emissions to CO₂. This result in a need for catalysts that have low temperature activity for the catalytic converters used in emission abatement systems. The development of active and stable catalyst using noble metals for low-temperature CO oxidation under ambient conditions remains a challenge since typical catalysts require temperatures above 100 °C for efficient operation.[226, 227]

It is well known that the reactivity of catalysts is significantly influenced by its shape and structure.[216] Potential improvements of the catalytic performance may be made by altering the

shape and exposed surfaces of these catalysts. As reported by Enterkin et al, more precise control of the support surface allows one to engineer and tailor supported catalysts with a higher degree of control over what surface orientation is exposed of the particle, which enables the possibility of precise modification and maximization of the reactivity.[13]

In this Chapter, Pt catalysts supported on two types of STO-NCs with two different surface terminations (TiO_2 and SrO) were prepared for CO oxidation, both of which have been well discussed in detail in Chapter IV and V. For comparison, a commercial Pt/ Al_2O_3 catalyst was also tested for CO oxidation. The differences in surface termination of these STO supports were exploited to create Pt catalysts with different surface structure and shape and therefore, potentially different active sites such as corner, edge, surface or Pt/substrates interface. As a result, the reactivity of supported platinum catalysts for CO oxidation varies due to these variances. Additionally, the work of Enterkin et. al demonstratess that STO-NC supports can suppress the deactivation of the Pt catalyst more than other Al_2O_3 or TiO_2 substrates.[190]

6.2: Experimental Methods

6.2.1 STO support material preparation

Two types of STO-NCs were prepared using a sol-precipitation hydrothermal treatment procedure, the SrO terminated STO-NC's procedure has been discussed in detail in Chapter II. The TiO_2 terminated STO-NCs are obtained using an acetic acid assisted hydrothermal synthesis. 80 mL of an aqueous solution containing stoichiometric amounts of Sr and Ti was prepared from $\text{Sr}(\text{OH})_2 \cdot 8\text{H}_2\text{O}$ and TiCl_4 . Coprecipitation of SrTiO_3 was induced by adding 5 g of NaOH pellets

to the above bimetallic precursor solution. Upon dissolution of the NaOH pellets, a highly viscous suspension was obtained, which was subsequently transferred to a 125 mL Teflon-lined autoclave and heated at 240 °C for 36 h. The solution was filtered, and the product washed thoroughly with double-deionized water, and dried at 80 °C for 24 h.

6.2.2 Pt nanoparticle atomic layer deposition

The Pt catalyst was deposited onto the two types of STO-NCs using ALD in a similar manner as described in previous chapters. The Pt ALD on both substrates was accomplished simultaneously in the ALD chamber to ensure the identical deposition conditions. For catalytic testing purposes, ~110 mg of each type of STO-NCs were loaded and uniformly spread in two separate stainless steel trays for each batch of synthesis. All substrates were pre-cleaned in situ using a 200 sccm flow of 15% ozone in oxygen at 200 °C for 15 min before deposition. 1 (200 °C), 3 (250 °C), 6 (250 °C) cycles of alternating exposures of MeCpPtMe₃/purge (300 s/600s) and H₂O/purge (120 s/300s) were conducted in a viscous flow ALD reactor. During deposition a 140 sccm ultrahigh purity nitrogen (99.995%) flow was continuously passing through the reaction chamber increasing the base pressure from 0.32 Torr to 0.90 Torr.

6.2.3 Catalyst Characterization

a. Electron Microscopy.

Transmission electron microscopy (TEM) images of STO-NCs were acquired before and after catalytic testing using a Joel JEM-2100F operated at 200 keV. Both high-resolution electron microscopy (HREM) and High angular annual dark field (HAADF) images of Pt/STO-NCs were recorded.

b. Fourier transform infrared spectroscopy

The atomically precise synthesis of supported Pt nanoparticles is possible as described in previous chapters (Chapter IV & V), wherein the composition, structure and size of the nanoparticles can be controlled by adjusting the ALD parameters. Alongside TEM images, we employed fourier transform infrared spectroscopy (FTIR) to interrogate the surface of Pt nanoparticles deposited with varying ALD cycles on STO-NCs substrates with different terminations to validate this approach. A commercial Pt/Al₂O₃ catalyst was purchased and also tested. The adsorption of carbon monoxide followed by FTIR spectroscopy has long been used to characterize the surface structure and reactivity of metallic catalysts.[118, 228-231] By performing FTIR measurements of CO chemisorption on our materials with varying ALD cycles and substrates, we can analyze the shape, height and wavenumber/position of adsorption peaks and thereby infer the nanoparticle structure.

The FTIR characterization was performed with a Nicolet 6700 diffuse reflectance infrared fourier transform (DRIFT) spectrometer equipped with an in situ diffuse reflectance cell and a high-temperature environmental chamber, Figure 6.1a. This chamber allowed for simulation of the practical CO catalytic test conditions. The Pt catalysts were pretreated prior to analysis with one of following two methods before CO adsorption: 1) reduction by a mixture of 10% H₂ in Ar

at 150 °C for 30 min or 2) oxidization by a 20% O₂ in Ar at 100 °C for 15 min. Following of both pre-treatments, all samples were purged with Ar while they cooled to room temperature before the background spectra were recorded. In-situ spectra were recorded at room temperature after each treatment: CO adsorption, CO removal using an oxygen purge and CO resorption. Spectra was also recorded for CO adsorption on bare STO substrates and for thermal desorption of CO from hydrogen pre-treated Pt catalysts as two control tests. All spectra (2,400-1,400 cm⁻¹; 1 cm⁻¹ resolution) were measured using a Hg-Cd-Te (MCT) detector and the average of 32 scans.

The IR spectrum obtained upon adsorption of CO on Pt generally gives rise to two $\nu_{C=O}$ bands: the first, normally appearing between 2,090 and 2,040 cm⁻¹, is attributed to linearly adsorbed CO on a single Pt atom, and the second, between 1,860 – 1,680 cm⁻¹, which is assigned to CO molecules bridging two or more Pt atoms. The intensity of the bridging CO band is usually weaker than linear CO in the case of platinum.[232] A model proposed by Blyholder aids in understanding the interactions between CO and Pt nanoparticles and how they affect the IR spectra.[233, 234] The model shows that a π bond forms between a CO molecule and a given surface Pt atom when it is adsorbed. The CO becomes a ligand on the surface metal atom partially filling of the d orbitals and resulting in a competition between the CO ligand with the nearby metal atoms for the d electrons of the surface Pt atom. As the coordination number of a surface metal atom increases, which viewed as a potential adsorption site for CO, the competition of CO and the other neighboring atoms will decrease. This reduces the back-bonding from the metal adsorption site to the π^* orbitals of CO leads to an increased $\nu_{C=O}$ frequency. The sensitivity of the $\nu_{C=O}$ frequency to the coordination number of the surface metal atoms results in the use of adsorbed CO as a probe molecule to help determine the surface coordination of Pt

atoms. Several studies have supported the correlation between CO frequency shifts and the coordination of the platinum atoms at the surface, for instance, Greenler et al. reported three different bands, at 2,081, 2,070 and 2,063 cm^{-1} , which were assigned to CO linearly bound to face, corner and edge atoms of Pt/SiO₂ samples.[235] This assignment was corroborated by the results obtained on single crystal planes, where the $\nu_{\text{C=O}}$ was 2,085 cm^{-1} and 2,065 cm^{-1} when CO was adsorbed on terrace sites and step and kink sites, respectively. Kappers and van der Maas reported a linear relation between the frequency of linear CO and the number of nearest neighbors of the surface sites.[236]

Another influence on the $\nu_{\text{C=O}}$ frequency is the CO coverage, which shifts to higher/lower frequencies when the number of CO $2\pi^*$ orbitals competing for the available d electrons of the metal atoms changes. The frequency shift observed due to altering the CO coverage can be explained by dipole-dipole coupling between chemisorbed CO molecules.[237] It has been reported by Crossley A. et. al. that the CO adsorption frequency shift on Pt(111) with increase CO coverage was attributable to dipole coupling.[238] Stoop et al. demonstrated that the adsorption of electron donors, such as ethylene, caused the separation of the CO dipoles, decreasing the dipole-dipole coupling between adjacent CO molecules and resulting in a red shift in the CO frequency without changing the CO bond strength.[239] It must be remarked that CO dipole-dipole coupling can occur even at low coverage and at low temperatures when the CO molecules tend to form clusters.[240]

c. Pt loading measurement

The Pt loading was measured by two ways: 1) from the mass gain recorded by an analytical balance after Pt ALD was performed and 2) from ICP-AES analysis described in Chapter IV.

6.2.4 Catalytic testing

The CO oxidation probe reaction was conducted in a 1/400 OD silica tube plug-flow microreactor (BenchCat 4000, Figure 6.1b). The catalysts were used as prepared and diluted with 300 mg silica dioxide before being transferred to the catalyst bed. The reactor was charged with the catalyst and placed in a clamshell furnace which is marked in the red box in Figure 6.1b. A thermocouple was then positioned at the top of the catalyst bed. The feed direction is from the top of the catalyst bed to the bottom. The reactor temperature was controlled using a programmable temperature controller. The reaction products were quantified using a gas chromatograph (Agilent GC, Figure 6.1c) equipped with a TCD detector. Pt/STO-NCs was evaluated for CO oxidation reactivity and CO turnover frequency (TOF) by passing 0.5% CO, 20% O₂ balanced with He over the catalyst. CO oxidation reactivity is defined as the percent of CO converted to carbon dioxide after passing through the catalyst bed. Carbon dioxide was the only product observed. The space velocity of the gas mixture was selected to maintain a CO conversion below 10% for all trials. For each run, the Pt/STO-NCs catalyst was first stabilized at 70 °C with 10 sccm of the reactant mixture for 4 h before any data was collected. The turnover frequency was calculated based on the moles of CO consumed per total moles of platinum (TOF_t)

and per moles of surface platinum (TOFs), with the percent of surface platinum coming from CO chemisorption results.

6.3: Results and discussion

6.3.1 General information of different Pt catalysts

Three types of Pt catalysts are investigated in this work: Pt/STO-NCs(AA), Pt/STO-NCs(OA) and commercial purchased Pt/Al₂O₃. Pt loading for 1(200 °C), 6(250 °C) cycles ALD deposition on STO-NCs(OA) are 3.60 wt% and 20 wt %, respectively, and for 1(200 °C), 3(250 °C) and 6(250 °C) cycles deposition on STO-NCs(AA) the Pt loadings are 0.562 wt%, 6.1 wt% and 8.9 wt%, respectively. The loading on the commercial Pt/Al₂O₃ is 5 wt%.

The as-deposited Pt nanoparticles exhibited a very narrow size distribution, with sizes ranging from 1 to 2 nm, depending upon number of ALD cycles and reaction temperature used during the synthesis. The uniform nanoparticle dispersion over the surface of the oxide support is remarkable; The HAADF showed that no significant agglomeration of the metal particles was observed (Figure 6.8 a,c,e). One Pt ALD cycle led to particles of ~1.56 nm diameter, while 3 and 6 Pt ALD cycles produced platinum particles of ~1.89 nm and ~2.02 nm diameter, respectively. A very wide size distribution (1-6 nm) was found for the commercial Pt/Al₂O₃ as shown in Figure 6.8a. The dispersion of the Pt particles are estimated from HAADF images and summarized in Table 4.2. All of the dispersion is in the range of 30% - 40%.

6.3.2 Fourier transform infrared studies of CO adsorption

Series of FTIR spectra were recorded of three types of samples which are pretreated with one of two ways: hydrogen reduction or oxygen purge. I will begin with the discussion of Pt catalysts on three different supports and were reduced with hydrogen. Figure 6.2a shows a typical FTIR spectrum for CO saturation on the Pt/STO-NCs (AA) surface. The spectrum shows an extremely weak peak at 2175 cm^{-1} , a weak peak at $1,781\text{ cm}^{-1}$ and a strong peak between $2,060\text{ cm}^{-1} - 2,090\text{ cm}^{-1}$ with a broad shoulder around $1,950\text{ cm}^{-1}$, which we assign to CO adsorption on STO-NCs substrates, bridge/threefold-hollow CO on the Pt particle facets and linear CO on surface/edge/corners of the Pt nanoparticles, respectively.[232] The shoulder that appears around 1950 cm^{-1} is generated by CO adsorbing at the interface of the Pt nanoparticles and the substrates.[241] Due to different structures presented in the Pt/ Al_2O_3 catalyst compared to Pt/STO-NCs, the FTIR peak position is slightly different. As shown in Figure 6.3a, the spectrum shows a peak at $2140\text{ cm}^{-1} - 2,270\text{ cm}^{-1}$ which is assigned to CO adsorption on Al_2O_3 substrates, a peak at 1830 cm^{-1} which is assigned to bridging adsorption and a strong peak at $1,970 - 2,120\text{ cm}^{-1}$ which is assigned to linear CO adsorption. However, there was no evidence in the FTIR spectra of CO adsorption on the interfaces between the Pt and alumina substrate. CO adsorption on the substrate (e.g. STO-NCs $2,175\text{ cm}^{-1}$, Al_2O_3 $2,140\text{ cm}^{-1} - 2,270\text{ cm}^{-1}$) is very weak and can be easily desorbed, e.g. a short time Ar purge ($\sim 3\text{ min}$) will easily desorb these CO molecules, as shown in Figure 6.2b. The band assigned to linear CO adsorption consists of two fine peaks, e.g. $\sim 2,070\text{ cm}^{-1}$ and $2,087\text{ cm}^{-1}$ for CO adsorption on Pt/STO-NCs(AA) (3 cycles, 6 cycles deposition), $2,064\text{ cm}^{-1}$ and $2,084\text{ cm}^{-1}$ for CO adsorption on Pt/ Al_2O_3 and Pt/STO-NCs(OA) (1 cycle, $200\text{ }^\circ\text{C}$). According to the previous discussion, the splitting of the linear CO adsorption peak is likely due to CO molecules adsorbed on different surface sites, e.g. surface ($2,081\text{ cm}^{-1}$), corner ($2,070\text{ cm}^{-1}$) and edge ($2,060\text{ cm}^{-1}$) atom of Pt nanoparticles. Linear

CO adsorption on different Pt particles is summarized in Table 6.1. If we assume all Pt sites are available for CO adsorption at saturated coverages, then the different intensity ratio of the fine peaks in linear adsorption area suggests a difference in the total number of corner, edge and face atom sites between the three types of supported Pt catalysts.

Adsorption of CO onto Pt surfaces is chemisorb which is much stronger than on substrate surface. This adsorption is irreversible which can be thermal stable to temperature high to 373K. 15 min annealing shown in Figure 6.3 doesn't show any apparent evidence of CO desorption. However, as indicated in Figure 6.4, these adsorptions are very sensitive to oxygen exposure which easily removes the adsorbed CO even at room temperature. The removal of CO is likely due to oxygen oxidation as an obvious CO₂ peak shows up at 2,350 cm⁻¹ immediately following oxygen exposure. More importantly, the removal behavior caused by oxygen is different for Pt nanoparticles on the three different substrates. For STO-NCs supported Pt catalysts, all adsorbed CO at Pt/STO-NCs interface and bridging CO desorb quickly (~1 min oxygen exposure) and completely. However, linearly adsorbed CO cannot be completely removed even with significantly longer oxygen exposures (> 8 min). This is either due to strong bonding of CO on the linear adsorption sites or the linearly bound CO is less reactive than the CO at interface sites. Pt/Al₂O₃ shows a significantly slower removal of adsorbed CO which suggests a lower reactivity for CO oxidation. For all Pt catalysts, CO can be easily restored by a short CO exposure (~1 min) after oxygen removal with all linear and bridge adsorption recovering to the original level before the removal. However, the linear adsorption peak assigned to CO adsorbed on surface and corner sites of Pt/STO-NCs (AA) changed, suggesting a possible structural occurring upon CO adsorption. As shown in Figure 6.5, the initial CO FTIR peak has a higher surface sites peak

(2,090 cm^{-1}) than corner sites peak (2,070 cm^{-1}), however, the comparative intensities flipped after reabsorption.

For Pt particles pretreated with oxygen at 100 °C, FTIR studies show very similar results comparing to Pt catalysts pre-reduced with hydrogen, as shown in Figure 6.6. Due to the presence of oxygen atoms remaining on the Pt surface after oxygen pretreatment, CO adsorption takes slightly longer dose time to get a saturated coverage. However, in return removal of CO using a room temperature oxygen purge is much more efficient than similar procedures for hydrogen pre-reduced Pt particles we discussed above. As the spectra in Figure 6.6 show more CO can be removed within even a shorter oxygen exposure and better CO maximum removal. Such behavior strongly implies that Pt nanoparticles with more oxidized state may more active for CO oxidation than metallic ones.

6.3.3 Carbon monoxide combustion catalytic test

To precisely investigate the catalytic performance of these different Pt catalysts, CO oxidation at 70 °C was carried out and the results are summarized in Figure 6.7. Figure 6.7a illustrates the catalytic performance lines for 1c (200 °C), 6c (250 °C) Pt/STO-NCs(OA), 1c (200 °C), 3c (250 °C), 6c (250 °C) Pt/STO-NCs(AA) and commercial Pt/Al₂O₃ for total Pt and surface Pt atoms. To address how the structure and shape alters the reactivity instead of loading and size, 1c Pt/STO-NCs(OA) (10.0 mg), 6 c Pt/STO-NCs(OA) (1.8 mg) and 6c Pt/STO-NCs(AA) (5.6 mg) with same mass of Pt are tested. To check the repeatability, 6 c Pt/STO-NCs (OA), 6c Pt/STO-NCs(AA) and Pt/Al₂O₃ with doubled amount of mass are included. The results indicate that the test is repeatable and Pt nanoparticles sitting on STO substrates are quite promising CO oxidation catalysts, which are superior to conventional commercial Pt/Al₂O₃ in terms of

reactivity. Here the the 11 hours test, the Pt nanoparticles on two types of STO substrates didn't show any evidence of deactivation according to the catalytic performance lines, which suggests there was no sintering of these nanoparticles. HAADF images shown in Figure 6.8 a,b (6c 250 °C Pt/STO-NCs(AA)), c,d (3c 250 °C Pt/STO-NCs(AA)) and e,f (6c 250 °C Pt/STO-NCs(OA)), give a comparison between Pt particles before and after CO oxidation test, which doesn't reveal any particle size and density change also suggesting there is no sintering effects. However, Pt/Al₂O₃ shows clear deactivation after 5 hours run (Figure 6.7 b) due to particle sintering. HAADF images in Figure 6.9 a,b clearly shows Pt particle size increase from 1.62 nm to 2.12 nm after CO oxidation suggesting the sintering of Pt nanoparticles on Al₂O₃ substrates.

Table 2 lists the reaction rates and turnover frequencies (TOFt, TOFs) of the different catalysts for CO oxidation. Pt/STO-NCs(OA) prepared with 1 cycle ALD at 200 °C gives a specific TOFt and TOFs of 0.48 mol.s⁻¹g⁻¹ and 1.14 mol.s⁻¹g⁻¹, which is about doubled that of Pt nanoparticles prepared with 6 cycles ALD at 250 °C on the same substrates. And very similar behavior is found for the catalysts of Pt/STO-NCs (AA). The TOFt and TOFs as a function of Pt particle size of three types of Pt catalysts are plotted in Figure 6.10, all of which indicate CO oxidation reactivity are sensitive to particle size and with increase in particle size the reactivity decrease. The size dependence of Pt reactivity on size can be explained by more total active sites/atoms are present on Pt catalysts with small size as we eliminate the influence of loading by using Pt with same mass (e.g. 1c Pt/STO-NCs(OA) (3.56%*10.0 mg), 6c Pt/STO-NCs(OA) (20%*1.8 mg)). The reactivity of the Pt catalysts also greatly depends on substrates. As indicated in Table 2 for CO oxidation at 70 °C, the Pt in Pt/STO-NCs(OA) is more reactive than that in Pt/STO-NCs(AA), both of which are significantly more reactive than Pt in Pt/Al₂O₃ catalysts with similar particle sizes. In fact, our Pt catalyst was much higher for CO oxidation among a

number of reported catalysts if we assume the slightly different reaction condition didn't change the reaction performance too much.[241] We attribute the higher reactivity of Pt/STO-NCs(OA) to the intrinsic nature of the Pt particles dispersed onto the STO substrates, where STO the surfaces lead to particles with more reactive sites (e.g. corner, edge, surface sites). An even more important substrate effect is that STO creates a particle/STO interface that is significantly more reactive than other Pt/substrates interfaces.

6.4: Conclusion

In summary, we synthesized and characterized a novel Pt catalyst with Pt nanoparticles uniformly dispersed on a STO-NCs support of medium high surface area. By choosing CO oxidation as a probe reaction, we revealed that the catalytic performance is strongly dependent on the supporting material and Pt nanoparticle size. For instance, Pt catalysts supported on STO-NCs shows 4-10 times higher activity than commercial Pt/Al₂O₃ and we observed that smaller Pt nanoparticles on the same support exhibit higher reactivity. Additionally, the structural integrity of Pt catalysts supported on STO-NCs is minimally affected by catalytic testing which might cause ripening and inter-particle sintering, and it does not appear to reduce the catalyst activity during the test. As revealed by FTIR study, there are several intrinsic CO adsorption peaks on the Pt particle surface. The different responses of the various types of adsorbed CO to oxygen removal suggests that different surface sites lead to different reactivity and each catalytic system contains varying amounts of each site. This is another possible know to which the catalytic performance can be tuned.

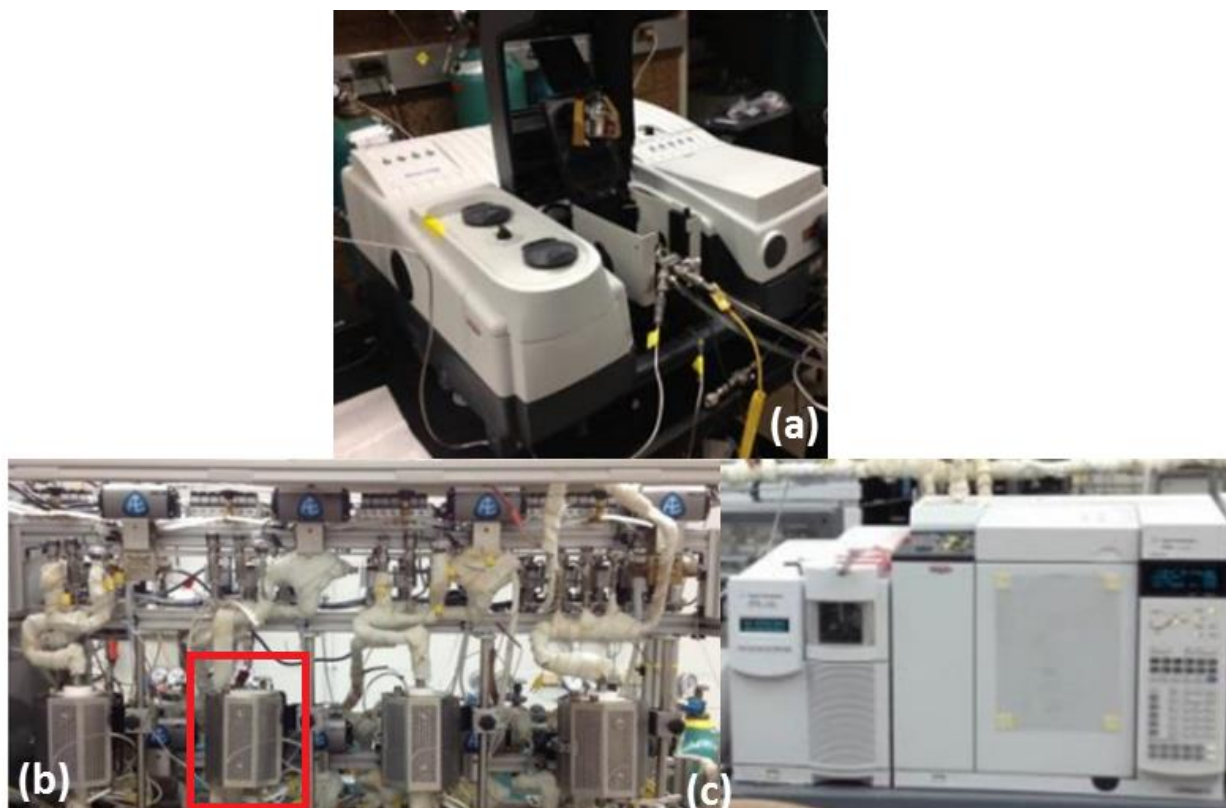


Figure 6.1. Images of (a) Nicolet 6700 DRIFTS (b) reactor BenchCat 4000 with the microreactor and clamshell furnace outlined in red (c) Agilent GC.

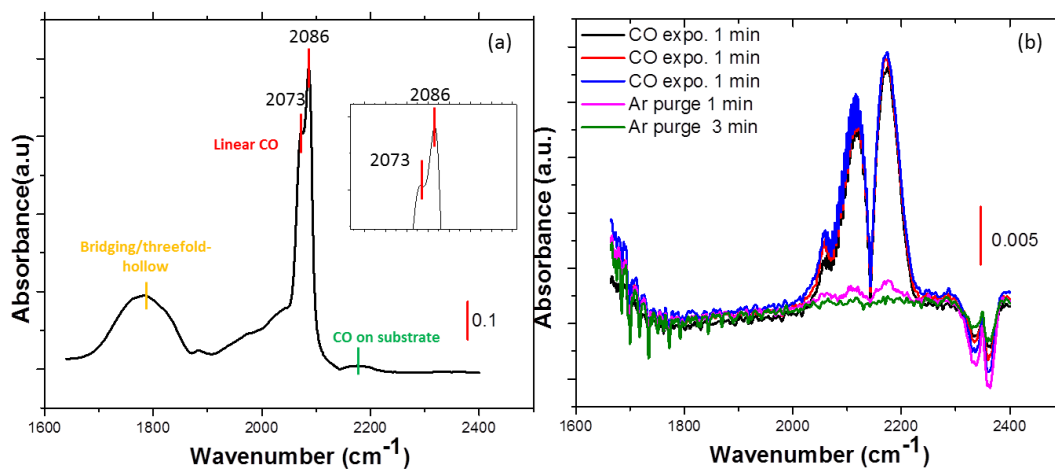


Figure 6.2. (a) A typical FTIR spectrum of CO adsorption on a Pt surface, three types of CO interactions are assigned: bridging/three-fold, linear CO and CO adsorbed on STO-NCs substrates. (b) A detail peak shows CO adsorption on STO-NCs, the adsorption can be easily desorbed.

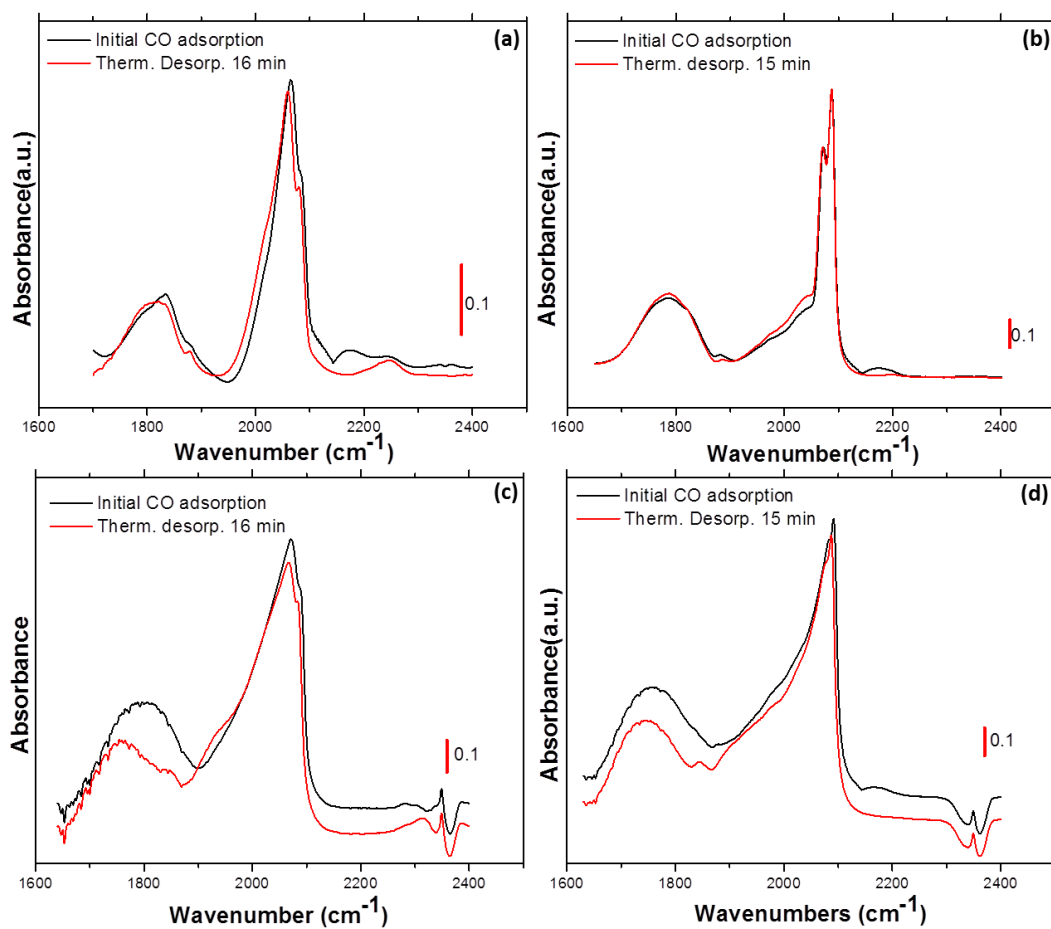


Figure 6.3. FTIR CO spectra of the four different samples does not show obvious changes for thermal desorption at 100 °C (a)Pt/Al₂O₃(commercial) (b) Pt/STO-NCs(AA) prepared using 6 cycles ALD deposition at 250 °C (c) Pt/STO-NCs(OA) prepared using 6 cycles ALD deposition at 250 °C (d) Pt/STO-NCs(AA) prepared using 3 cycles ALD deposition at 250 °C.

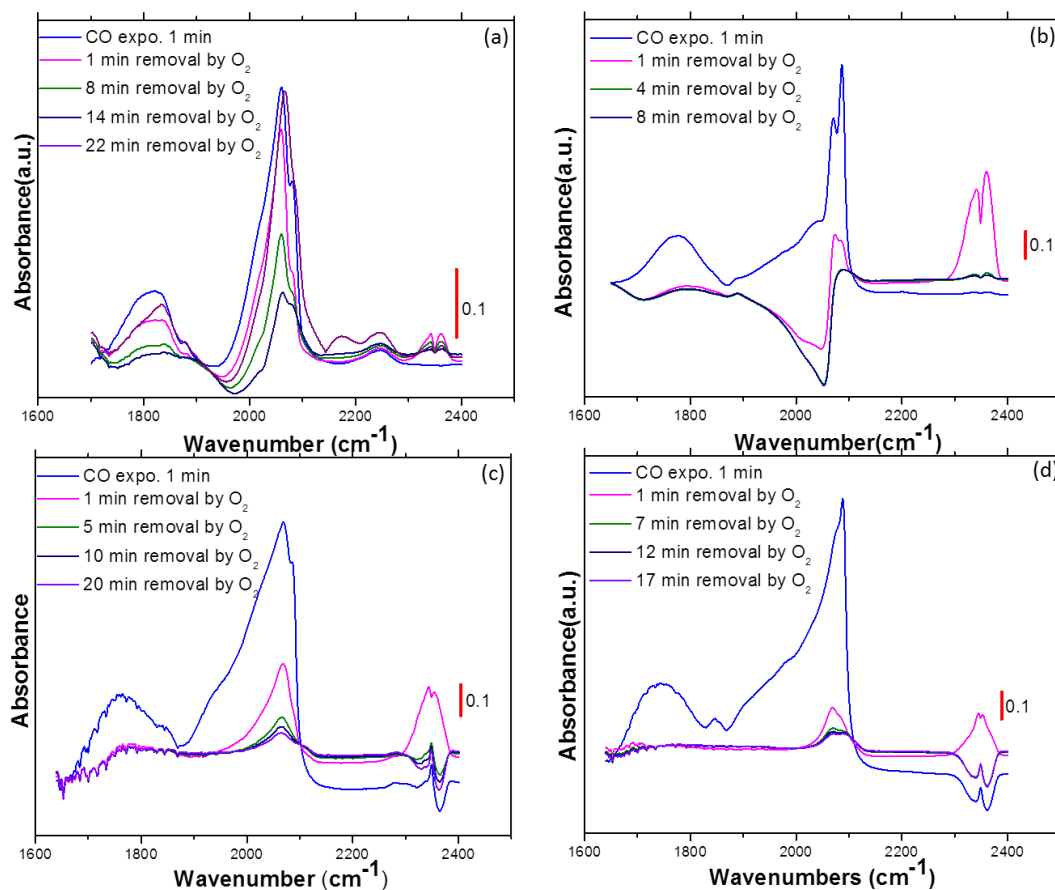


Figure 6.4. FTIR CO spectra evolves with varying oxygen dosing duration on the four different samples, described in Figure 6.3.

Table 6.1. Linear CO adsorption fine peak composition of different Pt catalysts

Sample	Linear Adsorption peak composition		
Pt/STO-NCs(AA) 6c-250°C	interface	Surface	Corner
Pt/ST Pt/STO-NCs(AA) 3c-250°C	interface	Surface	Corner
Pt/STO-NCs(OA) 6c-250°C	interface	Surface	Corner
Pt/STO-NCs(OA) 1c-200°C	interface	Surface	Edge
Pt/Al ₂ O ₃ (commercial)	x	Surface	Edge

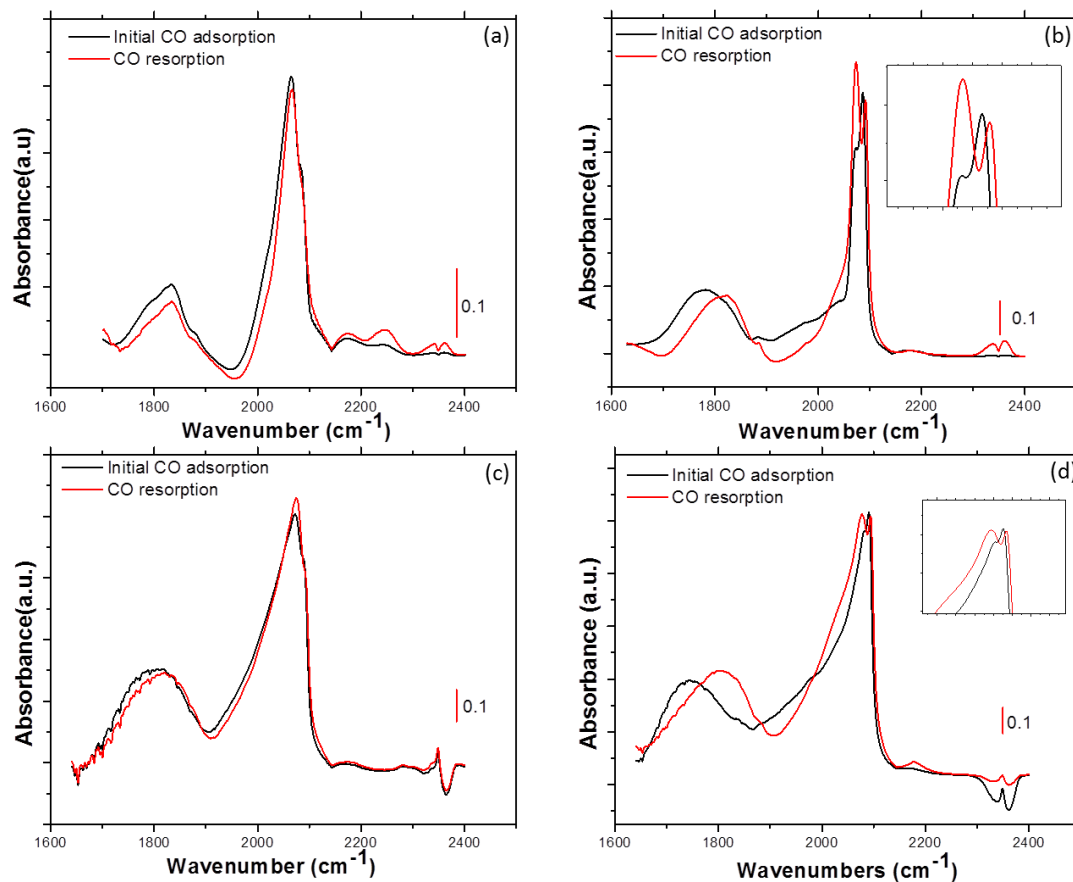


Figure 6.5. Initial CO adsorption and resorption after oxygen removal on four different Pt samples, describe in Figure 6.3. The inset spectra in (b) and (d) show that the linear CO resorption peaks changed remarkably comparing to initial CO adsorption on Pt/STO-NCs(AA).

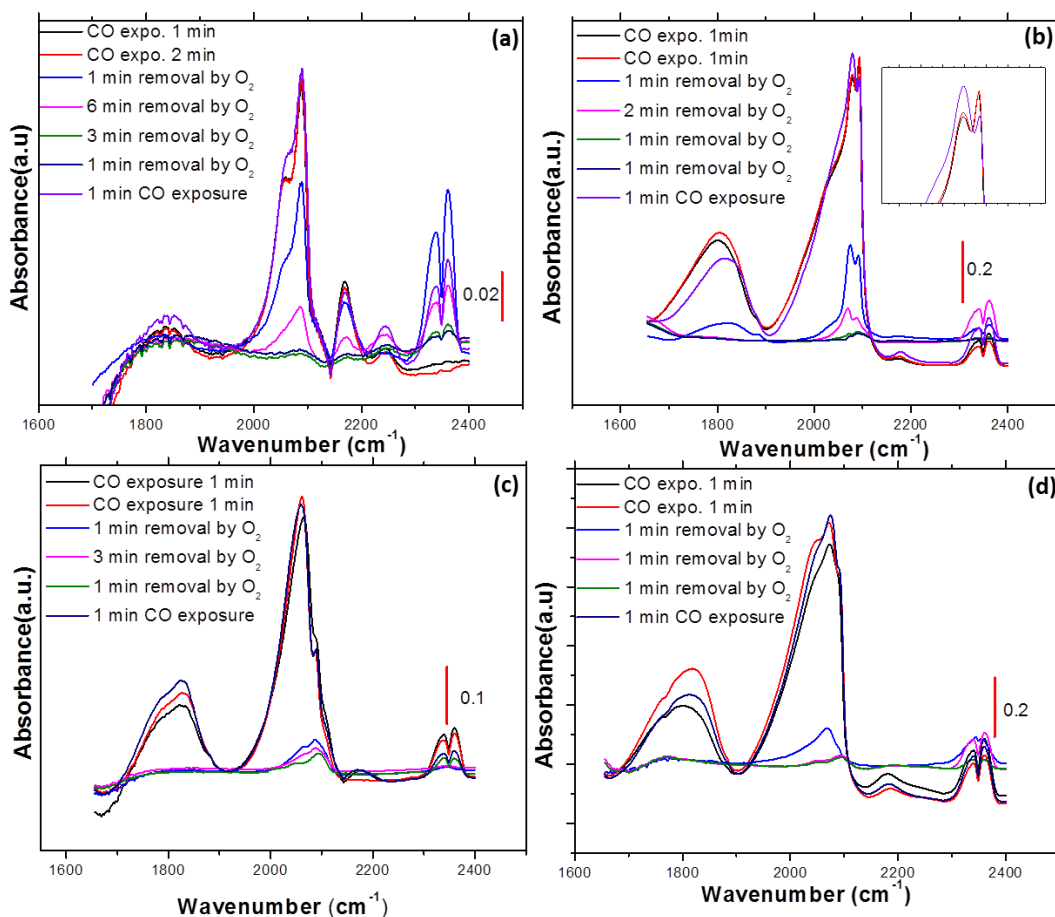


Figure 6.6. FTIR CO spectra evolves with different treatment on four different sample same pretreated using oxygen exposure (a) Pt/Al₂O₃ (commercial) (b) Pt/STO-NCs(AA) prepared using 6 cycles ALD deposition at 250 °C (c) Pt/STO-NCs(OA) prepared using 1 cycles ALD deposition at 200 °C (d) Pt/STO-NCs(OA) prepared using 6 cycles ALD deposition at 250 °C.

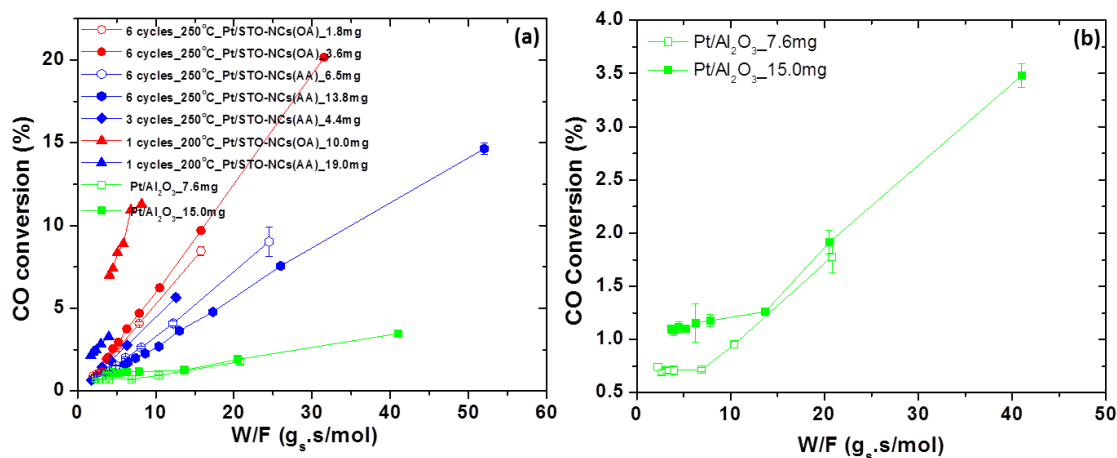


Figure 6.7. CO catalytic results of different Pt catalysts (a) CO conversion as a function of $W_{\text{surface Pt}}/F$. (b) Plot of CO conversion of Pt/Al₂O₃ clearly shows deactivation after 5 hours.

Table 6.2. CO oxidation turnover frequency at 70 °C for Pt/STO-NCs and Pt/Al₂O₃

Catalysts	Size (nm)	dispersion	Wt%	TOF _t (mol/g _t /s ⁻¹) ^a	TOF _s (mol/g _s /s ⁻¹) ^b
1c/200°C/OA	1.56	42.3	3.60	0.48	1.14
1c/200°C/AA	1.58	41.8	0.56	0.21	0.49
3c/250°C/AA	1.89	34.9	6.1	0.16	0.47
6c/250°C/OA	2.02	32.7	20	0.20	0.60
6c/250°C/AA	2.08	31.5	8.9	0.10	0.32
Pt/Al ₂ O ₃	1.62	40.7	5.0	0.034	0.083

^aTOF calculated based total Pt mass used. ^bTOF calculated based surface Pt atom.

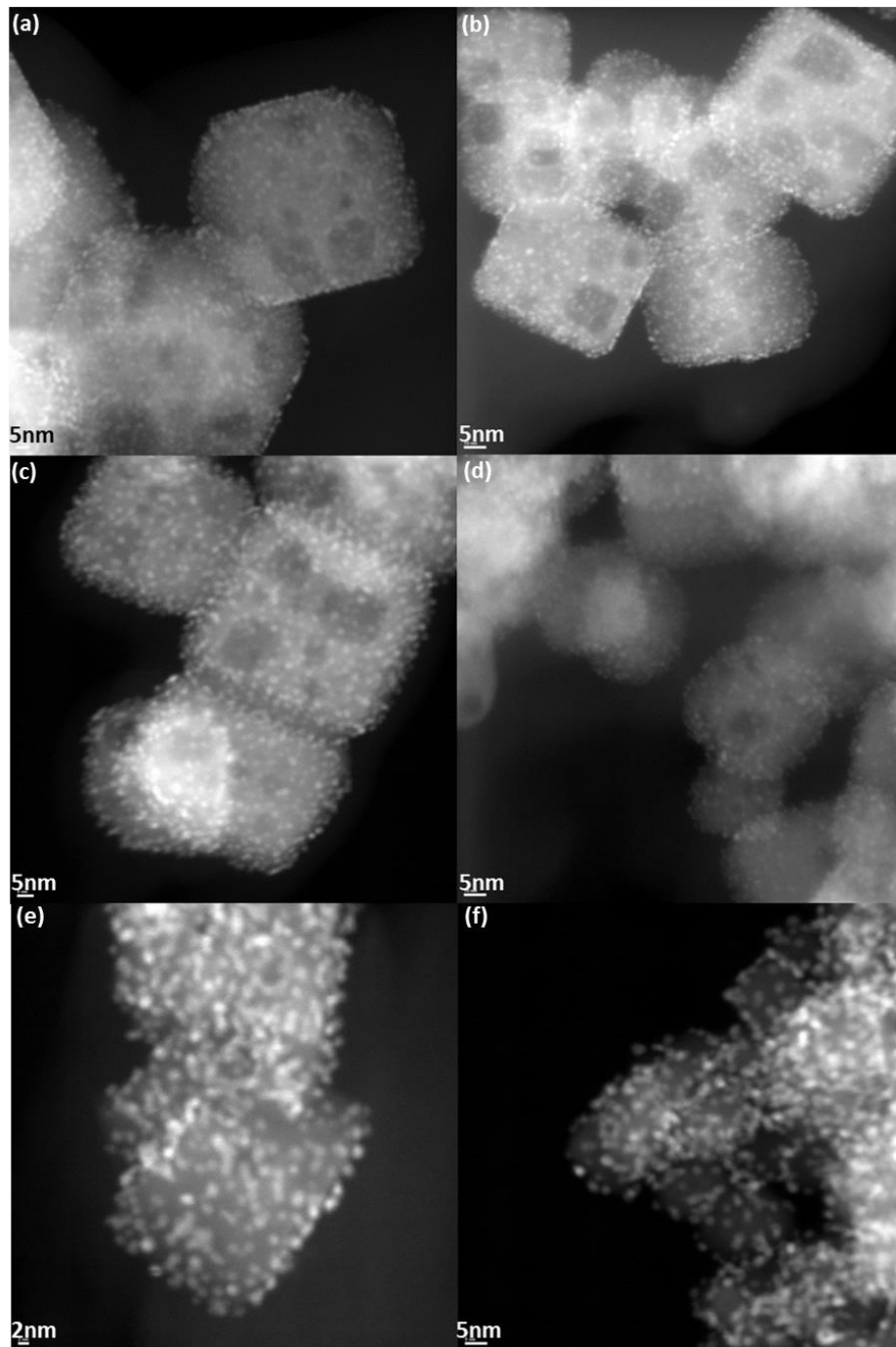


Figure 6.8. HAADF images of three different Pt/STO-NCs before (left side) and after (right side) CO oxidation test. (a),(b) 6c 250 °C Pt/STO-NCs(AA), (c),(d) 3c 250 °C Pt/STO-NCs(AA) and (e),(f) 6c 250 °C Pt/STO-NCs(OA).

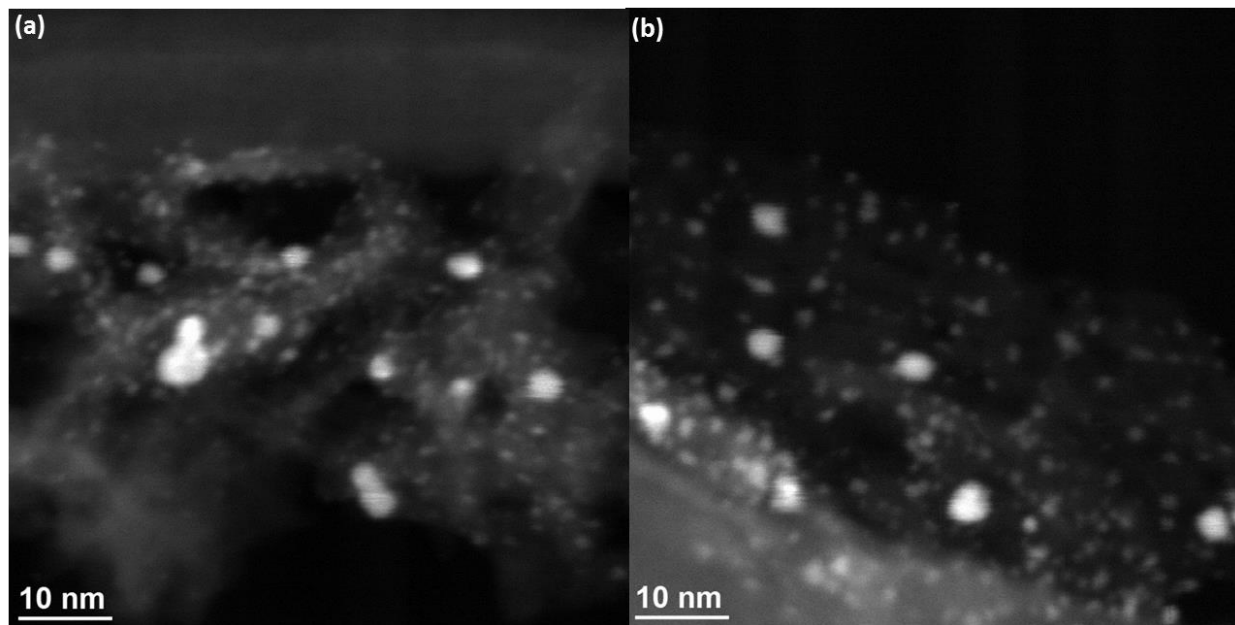


Figure 6.9. HAADF images of Pt/Al₂O₃ (a) before and (b) after CO oxidation test.

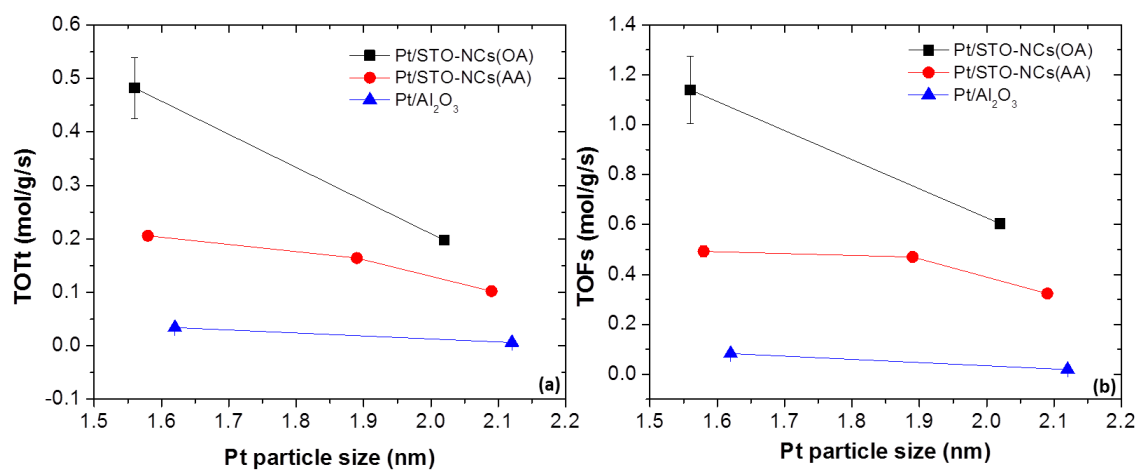


Figure 6.10. (a) TOF_t and (b) TOF_s as a function of Pt particle size of different Pt catalysts.

Chapter VII:

Conclusion

Catalysis continues to be an area where great potential of improving catalytic performance can be achieved through synthesis approaches. This dissertation examines an integral aspect of heterogeneous catalysis deposited using atomic layer deposition, namely the size, density, composition and shape of supported nanoparticles primarily in terms of the nanoscale morphology. Investigating catalytic materials at nanometer length scale is essential to developing and understanding the next generation of catalysts using novel synthesis techniques. Key properties of catalytic nanoparticles include the size, dispersion, loading, shape and composition are strongly related to the nucleation and growth, substrates and materials used for the synthesis. From a materials science perspective, these properties will impact the catalytic properties the nanoparticles exhibit and the performance they yield as a function of their morphology. This dissertation may now be evaluated under all these terms.

We began with ALD deposition of platinum nanoparticles on SC-STO substrates, as it's much easier to tailor the surface composition and structure on SC-STO than any nanoscale STO materials thus potentially benefit us for understanding catalytic performance of the system. The deposition can be greatly improved by contamination removal and hydroxyl enriching using BHF-HP etching. Following of that, Pt nanoparticle are deposited on different types of STO-NCS using ALD and extensively characterization techniques, such as HREM, HAADF, XPS and ICP-AES are used to understand how will Pt particle properties changed with ALD variables such as reaction temperature, number of ALD cycles, types of deposition strategies (e.g. AB-type, ABC-type ALD and static ABC-type ALD) and even selection of substrates and reagent. It shows that Pt particle size, density and loading vary with reaction temperature, number of cycles, ALD deposition strategy and substrates, reagent selection. While Pt structure and shape is

determined only on substrates selection, changing of 2nd reagent can lead to different chemical states and compositions.

Additionally, the formation mechanism of Pt nanoparticles is dug in details. In initial cycle ALD deposition, the Pt particles formed beginning with nucleation followed by growth. The final size is temperature dependent which affects the net Pt deposition. For multiple cycles, the particle size increases with the number of ALD cycles and the increase in size per cycle also affected by net Pt deposition during that cycle. However, the increase in size per cycle is significantly lower than first cycle due to carbonaceous material left on the surface from ligand decomposition.

Finally we move toward to direct catalytic application of these deposited Pt nanoparticles using a probe CO oxidation reaction. It turns out Pt/STO-NCs catalysts are quite promising catalysts for CO oxidation which has outstandingly activity about 4-10 times higher than commercial Pt/Al₂O₃. Besides substrates, the catalytic performance of CO oxidation is greatly influenced by Pt particle size, initial chemical state. FTIR studies imply that Pt nanoparticles on different substrates with different size can either own different type or amount of active sites which alters the catalytic performance.

As a whole, Pt nanoparticle deposited using ALD are ultrafine and uniformly dispersed on the STO substrates. The precious properties of the particles such as size, density, composition, surface structure and shape can be changed by tuning over extensively ALD synthesis parameters, which will benefit us for improving and controlling the catalytic performance of these systems. The work done in this dissertation are not limited to Pt/STO system but also helpful for

understanding other noble materials on various metal oxides substrates (e.g. TiO_2 , barium titanate, magnesium oxide etc) as the surface reaction taken place may be very similar.

References

1. Lin, Y.Y., et al., *Synthesis-Dependent Atomic Surface Structures of Oxide Nanoparticles*. Physical Review Letters, 2013. **111**(15).
2. Beaumont, S.K., G. Kyriakou, and R.M. Lambert, *Identity of the Active Site in Gold Nanoparticle-Catalyzed Sonogashira Coupling of Phenylacetylene and Iodobenzene*. Journal of the American Chemical Society, 2010. **132**(35): p. 12246-12248.
3. Yao, Y.F.Y., *The Oxidation of Co and Hydrocarbons over Noble-Metal Catalysts*. Journal of Catalysis, 1984. **87**(1): p. 152-162.
4. Raimondi, F., et al., *Nanoparticles in energy technology: Examples from electrochemistry and catalysis*. Angewandte Chemie-International Edition, 2005. **44**(15): p. 2190-2209.
5. Haller, G.L. and D.E. Resasco, *Metal Support Interaction - Group-VIII Metals and Reducible Oxides*. Advances in Catalysis, 1989. **36**: p. 173-235.
6. Verykios, X.E., Wieckowski, A., Savinova, E. R., Vayenas, C. G., Eds.; Marcel Dekker., *Support Effects on Catalytic Performance of Nanoparticles*. In *Catalysis and Electrocatalysis at Nanoparticle Surfaces*; Wieckowski, A., Savinova, E. R., Vayenas, C. G., Eds.; Marcel Dekker.: 2003.
7. Coq, B.F., F. , *Effects of Particle Size and Support on Some Catalytic Properties of Metallic and Bimetallic Catalysts*. In *Catalysis and Electrocatalysis at Nanoparticle Surfaces*; Wieckowski, A., Savinova, E. R., Vayenas, C. G., Eds.; Marcel Dekker: . 2003.
8. Panagiotopoulou, P. and D.I. Kondarides, *Effect of the nature of the support on the catalytic performance of noble metal catalysts for the water-gas shift reaction*. Catalysis Today, 2006. **112**(1-4): p. 49-52.
9. Campbell, C.T., *Metal films and particles on oxide surfaces: Structural, electronic and chemisorptive properties*. Journal of the Chemical Society-Faraday Transactions, 1996. **92**(9): p. 1435-1445.
10. Fu, Q. and T. Wagner, *Interaction of nanostructured metal overlayers with oxide surfaces*. Surface Science Reports, 2007. **62**(11): p. 431-498.
11. Viswanathan, V., F.Y.F. Wang, and H. Pitsch, *Effect of particle size and support on the catalytic activity of Platinum nanoparticles for oxygen reduction reaction*. Abstracts of Papers of the American Chemical Society, 2010. **239**.
12. Huang, M.H., S. Rej, and S.C. Hsu, *Facet-dependent properties of polyhedral nanocrystals*. Chemical Communications, 2014. **50**(14): p. 1634-1644.

13. Enterkin, J.A., K.R. Poeppelmeier, and L.D. Marks, *Oriented Catalytic Platinum Nanoparticles on High Surface Area Strontium Titanate Nanocuboids (vol 11, pg 993, 2011)*. Nano Letters, 2011. **11**(8): p. 3510-3510.
14. Hayek, K., R. Kramer, and Z. Paal, *Metal-support boundary sites in catalysis*. Applied Catalysis a-General, 1997. **162**(1-2): p. 1-15.
15. Che, M. and C.O. Bennett, *The Influence of Particle-Size on the Catalytic Properties of Supported Metals*. Advances in Catalysis, 1989. **36**: p. 55-172.
16. Ponec, V., *Catalysis by Alloys in Hydrocarbon Reactions*. Advances in Catalysis, 1983. **32**: p. 149-214.
17. Tauster, S.J., S.C. Fung, and R.L. Garten, *Strong Metal-Support Interactions - Group-8 Noble-Metals Supported on Tio₂*. Journal of the American Chemical Society, 1978. **100**(1): p. 170-175.
18. Dauscher, A. and G. Maire, *Isomerization and Hydrogenolysis Reactions of Hexanes over Platinum Catalysts Supported on Physical Mixtures of Tio₂ and Ceo₂*. Journal of Molecular Catalysis, 1991. **69**(2): p. 259-270.
19. Bond, G.C., R.R. Rajaram, and R. Burch, *Hydrogenolysis of Propane, Normal-Butane, and Isobutane over Various Pretreated Ru/Tio₂ Catalysts*. Journal of Physical Chemistry, 1986. **90**(20): p. 4877-4881.
20. Sadeghi, H.R. and V.E. Henrich, *Smsi in Rh/Tio₂ Model Catalysts - Evidence for Oxide Migration*. Journal of Catalysis, 1984. **87**(1): p. 279-282.
21. Simoens, A.J., et al., *A Study of the Nickel-Titanium Oxide Interaction*. Journal of Catalysis, 1984. **86**(2): p. 359-372.
22. Bernal, S., et al., *Metal-Support Interaction Phenomena in Rhodium Ceria and Rhodium Titania Catalysts - Comparative-Study by High-Resolution Transmission Electron-Spectroscopy*. Applied Catalysis a-General, 1993. **99**(1): p. 1-8.
23. Belzunegui, J.P., J.M. Rojo, and J. Sanz, *H-1-Nmr Procedure to Estimate the Extent of Metal-Surface Covered by Tiox Overlayers in Reduced Rh/Tio₂ Catalysts*. Journal of Physical Chemistry, 1991. **95**(9): p. 3463-3465.
24. Hu, L.H., et al., *Perovskite nanocuboid catalyst: Synthesis from a Lamellar microemulsion*. Abstracts of Papers of the American Chemical Society, 2013. **245**.
25. Rabuffetti, F.A., et al., *Synthesis-dependent first-order Raman scattering in SrTiO₃ nanocubes at room temperature*. Chemistry of Materials, 2008. **20**(17): p. 5628-5635.
26. deLigny, D. and P. Richet, *High-temperature heat capacity and thermal expansion of SrTiO₃ and SrZrO₃ perovskites*. Physical Review B, 1996. **53**(6): p. 3013-3022.

27. Iwahara, H., et al., *Proton Conduction in Sintered Oxides and Its Application to Steam Electrolysis for Hydrogen-Production*. Solid State Ionics, 1981. **3-4**(Aug): p. 359-363.
28. Uchida, H., N. Maeda, and H. Iwahara, *Relation between Proton and Hole Conduction in Srceo3-Based Solid Electrolytes under Water-Containing Atmospheres at High-Temperatures*. Solid State Ionics, 1983. **11**(2): p. 117-124.
29. Iwahara, H., et al., *Proton Conduction in Sintered Oxides Based on Baceo3*. Journal of the Electrochemical Society, 1988. **135**(2): p. 529-533.
30. Mori, K., et al., *New Route for the Preparation of Pd and PdAu Nanoparticles Using Photoexcited Ti-Containing Zeolite as an Efficient Support Material and Investigation of Their Catalytic Properties*. Langmuir, 2009. **25**(18): p. 11180-11187.
31. Su, B.T., et al., *Preparation of Nanosized CPF/ZnO Catalytic Material*. Chinese Journal of Inorganic Chemistry, 2009. **25**(11): p. 1982-1987.
32. Li, W., et al., *Preparation of highly ordered mesoporous AISBA-15-SO3H hybrid material for the catalytic synthesis of chalcone under solvent-free condition*. Applied Surface Science, 2010. **256**(10): p. 3183-3190.
33. Marcilly, C., *Preparation of Catalysts .1. Particle Germination and Growth - Importance of the Super-Saturation of the Medium*. Revue De L Institut Francais Du Petrole, 1984. **39**(2): p. 189-208.
34. Tsai, W., J.A. Schwarz, and C.T. Driscoll, *Differential Cation-Exchange Capacity (Dcec) of Nickel Supported on Silica Aluminas*. Journal of Catalysis, 1982. **78**(1): p. 88-95.
35. Ahonen, M., M. Pessa, and T. Suntola, *Study of Znte Films Grown on Glass Substrates Using an Atomic Layer Evaporation Method*. Thin Solid Films, 1980. **65**(3): p. 301-307.
36. Suntola, T. and J. Hyvarinen, *Atomic Layer Epitaxy*. Annual Review of Materials Science, 1985. **15**: p. 177-195.
37. Suntola, T., *Atomic Layer Epitaxy*. Acta Polytechnica Scandinavica-Electrical Engineering Series, 1989(64): p. 242-270.
38. Nishizawa, J., H. Abe, and T. Kurabayashi, *Molecular Layer Epitaxy*. Journal of the Electrochemical Society, 1985. **132**(5): p. 1197-1200.
39. Lakomaa, E.L., S. Haukka, and T. Suntola, *Atomic Layer Growth of Tio2 on Silica*. Applied Surface Science, 1992. **60-1**: p. 742-748.
40. Haukka, S., E.L. Lakomaa, and T. Suntola, *Analytical and Chemical Techniques in the Study of Surface Species in Atomic Layer Epitaxy*. Thin Solid Films, 1993. **225**(1-2): p. 280-283.

41. Haukka, S., et al., *Dispersion and Distribution of Titanium Species Bound to Silica from TiCl₄*. Langmuir, 1993. **9**(12): p. 3497-3506.
42. Utraiainen, M., et al., *Porous silicon host matrix for deposition by atomic layer epitaxy*. Thin Solid Films, 1997. **297**(1-2): p. 39-42.
43. Ott, A.W., et al., *Modification of porous alumina membranes using Al₂O₃ atomic layer controlled deposition*. Chemistry of Materials, 1997. **9**(3): p. 707-714.
44. Berland, B.S., et al., *In situ monitoring of atomic layer controlled pore reduction in alumina tubular membranes using sequential surface reactions*. Chemistry of Materials, 1998. **10**(12): p. 3941-3950.
45. Enterkin, J.A., K.R. Poepelmeier, and L.D. Marks, *Oriented catalytic platinum nanoparticles on high surface area strontium titanate nanocuboids*. Abstracts of Papers of the American Chemical Society, 2011. **241**.
46. Christensen, S.T., et al., *Supported Ru-Pt Bimetallic Nanoparticle Catalysts Prepared by Atomic Layer Deposition*. Nano Letters, 2010. **10**(8): p. 3047-3051.
47. Smeds, S., et al., *Chemisorption and TPD studies of hydrogen on Ni/Al₂O₃*. Applied Catalysis a-General, 1996. **144**(1-2): p. 177-194.
48. Backman, L.B., et al., *Characterisation of Co/SiO₂ catalysts prepared from Co(acac)₃ by gas phase deposition*. Applied Catalysis a-General, 2001. **208**(1-2): p. 223-234.
49. Christensen, S.T., et al., *Controlled Growth of Platinum Nanoparticles on Strontium Titanate Nanocubes by Atomic Layer Deposition*. Small, 2009. **5**(6): p. 750-757.
50. Lu, J.L. and P.C. Stair, *Low-Temperature ABC-Type Atomic Layer Deposition: Synthesis of Highly Uniform Ultrafine Supported Metal Nanoparticles*. Angewandte Chemie-International Edition, 2010. **49**(14): p. 2547-2551.
51. Lei, Y., et al., *Synthesis of Pt-Pd Core-Shell Nanostructures by Atomic Layer Deposition: Application in Propane Oxidative Dehydrogenation to Propylene*. Chemistry of Materials, 2012. **24**(18): p. 3525-3533.
52. Ueltzen, M., *The Verneuil Flame Fusion Process - Substances*. Journal of Crystal Growth, 1993. **132**(1-2): p. 315-328.
53. Boutonnet, M., et al., *Monodispersed Colloidal Metal Particles from Nonaqueous Solutions - Catalytic Behavior in Hydrogenolysis and Isomerization of Hydrocarbons of Supported Platinum Particles*. Catalysis Letters, 1991. **9**(5-6): p. 347-354.

54. Fu, Q.H., et al., *Polymeric surfactants based on oleic acid IV. Lamellar liquid crystal polymerization of sodium oleate/oleic acid/aliphatic diene/water system*. Journal of Dispersion Science and Technology, 2000. **21**(7): p. 1007-1021.
55. Ge, J.P., et al., *Formation of disperse nanoparticles at the oil/water interface in normal microemulsions*. Chemistry-a European Journal, 2006. **12**(25): p. 6552-6558.
56. Zhao, X.J., R.P. Bagwe, and W.H. Tan, *Development of organic-dye-doped silica nanoparticles in a reverse microemulsion*. Advanced Materials, 2004. **16**(2): p. 173-+.
57. Ganguli, A.K., et al., *Microemulsion route to the synthesis of nanoparticles*. Pure and Applied Chemistry, 2008. **80**(11): p. 2451-2477.
58. Esin, V.O., et al., *Mechanism and Shapes of Crystal-Growth*. Journal of Crystal Growth, 1984. **66**(2): p. 459-464.
59. Hu, L.H., et al., *SrTiO₃ Nanocuboids from a Lamellar Microemulsion*. Chemistry of Materials, 2013. **25**(3): p. 378-384.
60. Setinc, T., et al., *Inherent defects in sol-precipitation/hydrothermally derived SrTiO₃ nanopowders*. Ceramics International, 2013. **39**(6): p. 6727-6734.
61. Rabuffetti, F.A., P.C. Stair, and K.R. Poeppelmeier, *Synthesis-Dependent Surface Acidity and Structure of SrTiO₃ Nanoparticles*. Journal of Physical Chemistry C, 2010. **114**(25): p. 11056-11067.
62. <http://office.microsoft.com/en-us/excel-help/using-excel-solver-to-set-quantity-and-pricing-HA001111864.aspx>.
63. Jia, C.L., M. Lentzen, and K. Urban, *Atomic-resolution imaging of oxygen in perovskite ceramics*. Science, 2003. **299**(5608): p. 870-873.
64. Wulff, G., *On the question of speed of growth and dissolution of crystal surfaces*. Zeitschrift Fur Kristallographie Und Mineralogie, 1901. **34**(5/6): p. 449-530.
65. Sekerka, R.F., *Equilibrium and growth shapes of crystals: how do they differ and why should we care?* Crystal Research and Technology, 2005. **40**(4-5): p. 291-306.
66. Frank, F.C., *In Growth and perfection of crystals;*
67. Pileni, M.P., *The role of soft colloidal templates in controlling the size and shape of inorganic nanocrystals*. Nature Materials, 2003. **2**(3): p. 145-150.
68. Eastoe, J., M.J. Hollamby, and L. Hudson, *Recent advances in nanoparticle synthesis with reversed micelles*. Advances in Colloid and Interface Science, 2006. **128**: p. 5-15.

69. Eckert, J.O., et al., *Kinetics and mechanisms of hydrothermal synthesis of barium titanate*. Journal of the American Ceramic Society, 1996. **79**(11): p. 2929-2939.
70. Knauss, K.G., et al., *Ti(IV) hydrolysis constants derived from rutile solubility measurements made from 100 to 300 degrees C*. Applied Geochemistry, 2001. **16**(9-10): p. 1115-1128.
71. Zhang, S.C., et al., *Formation mechanisms of SrTiO₃ nanoparticles under hydrothermal conditions*. Materials Science and Engineering B-Solid State Materials for Advanced Technology, 2004. **110**(1): p. 11-17.
72. Topallar, H., Y. Bayrak, and M. Iscan, *Thermodynamics of dissociation of strontium, barium and nickel caproates in water*. Turkish Journal of Chemistry, 1997. **21**(3): p. 195-199.
73. Aarik, J., et al., *Titanium isopropoxide as a precursor for atomic layer deposition: characterization of titanium dioxide growth process*. Applied Surface Science, 2000. **161**(3-4): p. 385-395.
74. Blanquart, T., et al., *[Zr(NEtMe)₂(guan-NEtMe)₂] as a Novel Atomic Layer Deposition Precursor: ZrO₂ Film Growth and Mechanistic Studies*. Chemistry of Materials, 2013. **25**(15): p. 3088-3095.
75. Loginova, E., et al., *Factors influencing graphene growth on metal surfaces*. New Journal of Physics, 2009. **11**.
76. Vo, D.Q., E.J. Kim, and S. Kim, *Surface modification of hydrophobic nanocrystals using short-chain carboxylic acids*. Journal of Colloid and Interface Science, 2009. **337**(1): p. 75-80.
77. Jung, I., et al., *Synthesis of low-temperature-processable and highly conductive Ag ink by a simple ligand modification: the role of adsorption energy*. Journal of Materials Chemistry C, 2013. **1**(9): p. 1855-1862.
78. Akbashev, A.R., G.N. Chen, and J.E. Spanier, *A Facile Route for Producing Single-Crystalline Epitaxial Perovskite Oxide Thin Films*. Nano Letters, 2014. **14**(1): p. 44-49.
79. Aaltonen, T., et al., *Atomic layer deposition of platinum thin films*. Chemistry of Materials, 2003. **15**(9): p. 1924-1928.
80. Elam, J.W., N.P. Dasgupta, and F.B. Prinz, *ALD for clean energy conversion, utilization, and storage*. Mrs Bulletin, 2011. **36**(11): p. 899-906.
81. Knez, M., K. Niesch, and L. Niinisto, *Synthesis and surface engineering of complex nanostructures by atomic layer deposition*. Advanced Materials, 2007. **19**(21): p. 3425-3438.
82. George, S.M., *Atomic Layer Deposition: An Overview*. Chemical Reviews, 2010. **110**(1): p. 111-131.

83. Miikkulainen, V., et al., *Atomic layer deposition of $\text{Li}_x\text{Ti}_y\text{O}_z$ thin films*. Rsc Advances, 2013. **3**(20): p. 7537-7542.
84. Keranen, J., et al., *Preparation, characterization and activity testing of vanadia catalysts deposited onto silica and alumina supports by atomic layer deposition*. Applied Catalysis a-General, 2002. **228**(1-2): p. 213-225.
85. Cho, S., et al., *Ethanol sensors based on ZnO nanotubes with controllable wall thickness via atomic layer deposition, an O-2 plasma process and an annealing process*. Sensors and Actuators B-Chemical, 2012. **162**(1): p. 300-306.
86. Erkens, I.J.M., et al., *Room Temperature Sensing of O-2 and CO by Atomic Layer Deposition Prepared ZnO Films Coated with Pt Nanoparticles*. Atomic Layer Deposition Applications 9, 2013. **58**(10): p. 203-214.
87. Roy, D. and S.B. Krupanidhi, *Excimer Laser Ablated Barium Strontium-Titanate Thin-Films for Dynamic Random-Access Memory Applications*. Applied Physics Letters, 1993. **62**(10): p. 1056-1058.
88. Krupanidhi, S.B. and G.M. Rao, *Pulsed-Laser Deposition of Strontium-Titanate Thin-Films for Dynamic Random-Access Memory Applications*. Thin Solid Films, 1994. **249**(1): p. 100-108.
89. Yan, H., T. Jo, and H. Okuzaki, *Low-Voltage Pentacene Field-Effect Transistors Fabricated on High-Dielectric-Constant Strontium Titanate Insulator*. Japanese Journal of Applied Physics, 2010. **49**(3).
90. Uchida, K., et al., *A single crystalline strontium titanate thin film transistor*. Journal of Applied Physics, 2010. **107**(9).
91. Carr, R.G. and G.A. Somorjai, *Hydrogen-Production from Photolysis of Steam Adsorbed onto Platinized SrTiO_3* . Nature, 1981. **290**(5807): p. 576-577.
92. Wagner, F.T., S. Ferrer, and G.A. Somorjai, *Photocatalytic Hydrogen-Production from Water over SrTiO_3 Crystal-Surfaces, Electron-Spectroscopy Studies of Adsorbed H-2, O-2 and H2o*. Surface Science, 1980. **101**(1-3): p. 462-474.
93. Wagner, F.T. and G.A. Somorjai, *Photocatalytic and Photoelectrochemical Hydrogen-Production on Strontium-Titanate Single-Crystals*. Journal of the American Chemical Society, 1980. **102**(17): p. 5494-5502.
94. Marti, X., et al., *Epitaxial growth of biferroic $\text{YMnO}_3(0001)$ on platinum electrodes*. Journal of Crystal Growth, 2007. **299**(2): p. 288-294.
95. Schmidt, S., et al., *Microstructure of epitaxial $\text{SrTiO}_3/\text{Pt}/\text{Ti}/\text{sapphire}$ heterostructures*. Journal of Materials Research, 2005. **20**(9): p. 2261-2265.

96. Novotny, Z., et al., *Probing the surface phase diagram of Fe₃O₄(001) towards the Fe-rich limit: Evidence for progressive reduction of the surface (vol 87, 195410, 2013)*. Physical Review B, 2013. **88**(3).
97. Jacobson, P., et al., *Decomposition of catechol and carbonaceous residues on TiO₂(110): A model system for cleaning of extreme ultraviolet lithography optics*. Journal of Vacuum Science & Technology B, 2008. **26**(6): p. 2236-2240.
98. Dulub, O., et al., *Electron-induced oxygen desorption from the TiO₂(011)-2x1 surface leads to self-organized vacancies*. Science, 2007. **317**(5841): p. 1052-1056.
99. Li, M., et al., *The influence of the bulk reduction state on the surface structure and morphology of rutile TiO₂(110) single crystals*. Journal of Physical Chemistry B, 2000. **104**(20): p. 4944-4950.
100. Russell, B.C. and M.R. Castell, *Surface of sputtered and annealed polar SrTiO₃(111): TiO_x-rich (n x n) reconstructions*. Journal of Physical Chemistry C, 2008. **112**(16): p. 6538-6545.
101. Egashira, M., et al., *Temperature Programmed Desorption Study of Water Adsorbed on Metal-Oxides .1. Anatase and Rutile*. Bulletin of the Chemical Society of Japan, 1978. **51**(11): p. 3144-3149.
102. Egashira, M., et al., *Temperature Programmed Desorption Study of Water Adsorbed on Metal-Oxides .2. Tin Oxide Surfaces*. Journal of Physical Chemistry, 1981. **85**(26): p. 4125-4130.
103. Neuwald, U., et al., *Wet Chemical Etching of Si(100) Surfaces in Concentrated NH₄F Solution - Formation of (2x1)H Reconstructed Si(100) Terraces Versus (111) Faceting*. Surface Science, 1993. **296**(1): p. L8-L14.
104. Gosalvez, M.A. and R.M. Nieminen, *Surface morphology during anisotropic wet chemical etching of crystalline silicon*. New Journal of Physics, 2003. **5**.
105. Polli, A.D., et al., *Growth of platinum on TiO₂- and SrO-terminated SrTiO₃(100)*. Surface Science, 2000. **448**(2-3): p. 279-289.
106. Kawasaki, M., et al., *Atomic Control of the SrTiO₃ Crystal-Surface*. Science, 1994. **266**(5190): p. 1540-1542.
107. Bednorz, J.G. and H.J. Scheel, *Growth of SrTiO₃ Crystals Using Verneuil Method*. Zeitschrift Fur Kristallographie, 1977. **146**(1-3): p. 91-91.
108. Mochizuki, S., et al., *Defect-induced optical absorption and photoluminescence of Verneuil grown SrTiO₃ crystal*. Physica B-Condensed Matter, 2006. **376**: p. 816-819.
109. http://en.wikipedia.org/wiki/Chemical-mechanical_planarization.

110. Hullar, T. and C. Anastasio, *Yields of hydrogen peroxide from the reaction of hydroxyl radical with organic compounds in solution and ice*. Atmospheric Chemistry and Physics, 2011. **11**(14): p. 7209-7222.
111. Cantrell, C.A., et al., *Carbon Kinetic Isotope Effect in the Oxidation of Methane by the Hydroxyl Radical*. Journal of Geophysical Research-Atmospheres, 1990. **95**(D13): p. 22455-22462.
112. Wang, J.J., et al., *TiO₂ nanoparticles with increased surface hydroxyl groups and their improved photocatalytic activity*. Catalysis Communications, 2012. **19**: p. 96-99.
113. Simonsen, M.E., Z.S. Li, and E.G. Sogaard, *Influence of the OH groups on the photocatalytic activity and photoinduced hydrophilicity of microwave assisted sol-gel TiO₂ film*. Applied Surface Science, 2009. **255**(18): p. 8054-8062.
114. Takahashi, K. and H. Yui, *Analysis of Surface OH Groups on TiO₂ Single Crystal with Polarization Modulation Infrared External Reflection Spectroscopy*. Journal of Physical Chemistry C, 2009. **113**(47): p. 20322-20327.
115. Ortion, J.M., Y. Cordier, and J.C. Garcia, *Temperature dependence of GaAs chemical etching using AsCl₃*. Journal of Crystal Growth, 1996. **164**(1-4): p. 97-103.
116. Liu, H.S., et al., *A review of anode catalysis in the direct methanol fuel cell*. Journal of Power Sources, 2006. **155**(2): p. 95-110.
117. Jiang, X.R., et al., *Application of atomic layer deposition of platinum to solid oxide fuel cells*. Chemistry of Materials, 2008. **20**(12): p. 3897-3905.
118. Alayoglu, S., et al., *Ru-Pt core-shell nanoparticles for preferential oxidation of carbon monoxide in hydrogen*. Nature Materials, 2008. **7**(4): p. 333-338.
119. Fox, M.A. and M.T. Dulay, *Heterogeneous Photocatalysis*. Chemical Reviews, 1993. **93**(1): p. 341-357.
120. Yuliati, L. and H. Yoshida, *Photocatalytic conversion of methane*. Chemical Society Reviews, 2008. **37**(8): p. 1592-1602.
121. Yoshida, H., Y. Yazawa, and T. Hattori, *Effects of support and additive on oxidation state and activity of Pt catalyst in propane combustion*. Catalysis Today, 2003. **87**(1-4): p. 19-28.
122. Lashdaf, M., et al., *Deposition of platinum into beta-zeolite*. Recent Advances in the Science and Technology of Zeolites and Related Materials, Pts a - C, 2004. **154**: p. 1708-1713.
123. Ahmadi, T.S., et al., *Shape-controlled synthesis of colloidal platinum nanoparticles*. Science, 1996. **272**(5270): p. 1924-1926.

124. Zhang, J., et al., *Synthesis and Oxygen Reduction Activity of Shape-Controlled Pt₃Ni Nanopolyhedra*. Nano Letters, 2010. **10**(2): p. 638-644.
125. Solla-Gullon, J., et al., *Shape-dependent electrocatalysis: methanol and formic acid electrooxidation on preferentially oriented Pt nanoparticles*. Physical Chemistry Chemical Physics, 2008. **10**(25): p. 3689-3698.
126. Lee, I., et al., *Tuning selectivity in catalysis by controlling particle shape*. Nature Materials, 2009. **8**(2): p. 132-138.
127. Bratlie, K.M., et al., *Platinum nanoparticle shape effects on benzene hydrogenation selectivity*. Nano Letters, 2007. **7**(10): p. 3097-3101.
128. Croy, J.R., et al., *Size dependent study of MeOH decomposition over size-selected pt nanoparticles synthesized via micelle encapsulation*. Catalysis Letters, 2007. **118**(1-2): p. 1-7.
129. Stair, P.C., *Advanced synthesis for advancing heterogeneous catalysis*. Journal of Chemical Physics, 2008. **128**(18).
130. Lopez, T., et al., *Spectroscopic Characterization and Catalytic Properties of Sol-Gel Pd/SiO₂ Catalysts*. Journal of Catalysis, 1992. **138**(2): p. 463-473.
131. Xie, Y., et al., *In Situ Controllable Loading of Ultrafine Noble Metal Particles on Titania*. Journal of the American Chemical Society, 2009. **131**(19): p. 6648-+.
132. Okamoto, K., et al., *Formation of nanoarchitectures including subnanometer palladium clusters and their use as highly active catalysts*. Journal of the American Chemical Society, 2005. **127**(7): p. 2125-2135.
133. Schafer, S., et al., *Platinum nanoparticles deposited on wide-bandgap semiconductor surfaces for catalytic applications*. Physica Status Solidi C: Current Topics in Solid State Physics, Vol 7, No 2, 2010. **7**(2): p. 411-414.
134. Faust, M., et al., *Synthesis of Pt/SiO₂ Catalyst Nanoparticles from a Continuous Aerosol Process using Novel Cyclo-octadienylplatinum Precursors*. Chemical Vapor Deposition, 2013. **19**(7-9): p. 274-283.
135. Chen, Y.J., et al., *Low-Temperature Organometallic Chemical Vapor-Deposition of Platinum*. Applied Physics Letters, 1988. **53**(17): p. 1591-1592.
136. Hiratani, M., et al., *Platinum film growth by chemical vapor deposition based on autocatalytic oxidative decomposition*. Journal of the Electrochemical Society, 2001. **148**(8): p. C524-C527.
137. Xue, Z.L., et al., *Organometallic Chemical Vapor-Deposition of Platinum - Reaction-Kinetics and Vapor-Pressures of Precursors*. Chemistry of Materials, 1992. **4**(1): p. 162-166.

138. Kwak, B.S., et al., *Study of Epitaxial Platinum Thin-Films Grown by Metalorganic Chemical Vapor-Deposition*. Journal of Applied Physics, 1992. **72**(8): p. 3735-3740.
139. Lee, J.M., et al., *Effect of O-2 addition on the deposition of Pt thin films by metallorganic chemical vapor deposition*. Journal of the Electrochemical Society, 1998. **145**(3): p. 1066-1069.
140. Xue, Z.L., et al., *Characterization of (Methylcyclopentadienyl)Trimethylplatinum and Low-Temperature Organometallic Chemical Vapor-Deposition of Platinum Metal*. Journal of the American Chemical Society, 1989. **111**(24): p. 8779-8784.
141. Lu, J.L., et al., *Coking- and Sintering-Resistant Palladium Catalysts Achieved Through Atomic Layer Deposition*. Science, 2012. **335**(6073): p. 1205-1208.
142. Puurunen, R.L., *Surface chemistry of atomic layer deposition: A case study for the trimethylaluminum/water process*. Journal of Applied Physics, 2005. **97**(12).
143. Lim, B.S., A. Rahtu, and R.G. Gordon, *Atomic layer deposition of transition metals*. Nature Materials, 2003. **2**(11): p. 749-754.
144. Pagan-Torres, Y.J., et al., *Synthesis of Highly Ordered Hydrothermally Stable Mesoporous Niobia Catalysts by Atomic Layer Deposition*. Acs Catalysis, 2011. **1**(10): p. 1234-1245.
145. King, J.S., et al., *Ultralow loading Pt nanocatalysts prepared by atomic layer deposition on carbon aerogels*. Nano Letters, 2008. **8**(8): p. 2405-2409.
146. Elam, J.W., et al., *Atomic layer deposition of palladium films on Al₂O₃ surfaces*. Thin Solid Films, 2006. **515**(4): p. 1664-1673.
147. Lu, J.L. and P.C. Stair, *Nano/Subnanometer Pd Nanoparticles on Oxide Supports Synthesized by AB-type and Low-Temperature ABC-type Atomic Layer Deposition: Growth and Morphology*. Langmuir, 2010. **26**(21): p. 16486-16495.
148. Tinnemans, A.H.A., et al., *Formation of Methanol and Other C-1-C-3 Compounds in the Photoassisted Reaction of Formaldehyde and Water over Strontium-Titanate Suspensions Containing Transition-Metal Oxide Deposits*. Nouveau Journal De Chimie-New Journal of Chemistry, 1982. **6**(7-8): p. 373-379.
149. Aurianblajeni, B., M. Halmann, and J. Manassen, *Photo-Reduction of Carbon-Dioxide and Water into Formaldehyde and Methanol on Semiconductor-Materials*. Solar Energy, 1980. **25**(2): p. 165-170.
150. Setthapun, W., et al., *Genesis and Evolution of Surface Species during Pt Atomic Layer Deposition on Oxide Supports Characterized by in Situ XAFS Analysis and Water-Gas Shift Reaction*. Journal of Physical Chemistry C, 2010. **114**(21): p. 9758-9771.

151. Linsebigler, A.L., G.Q. Lu, and J.T. Yates, *Photocatalysis on TiO₂ Surfaces - Principles, Mechanisms, and Selected Results*. Chemical Reviews, 1995. **95**(3): p. 735-758.
152. Mackus, A.J.M., et al., *Catalytic Combustion and Dehydrogenation Reactions during Atomic Layer Deposition of Platinum*. Chemistry of Materials, 2012. **24**(10): p. 1752-1761.
153. Mackus, A.J.M., et al., *Influence of Oxygen Exposure on the Nucleation of Platinum Atomic Layer Deposition: Consequences for Film Growth, Nanopatterning, and Nanoparticle Synthesis*. Chemistry of Materials, 2013. **25**(9): p. 1905-1911.
154. Lee, S.W., et al., *Influences of metal, non-metal precursors, and substrates on atomic layer deposition processes for the growth of selected functional electronic materials*. Coordination Chemistry Reviews, 2013. **257**(23-24): p. 3154-3176.
155. Verykios, X.E., *Support Effects on Catalytic Performance of Nanoparticles In Catalysis*. 2003.
156. Sinfelt, J.H., *Hydrogenolysis of Ethane over Supported Platinum*. Journal of Physical Chemistry, 1964. **68**(2): p. 344-&.
157. Taylor, W.F., J.H. Sinfelt, and D.J.C. Yates, *Catalysis over Supported Metals .4. Ethane Hydrogenolysis over Dilute Nickel Catalysts*. Journal of Physical Chemistry, 1965. **69**(11): p. 3857-&.
158. Taylor, W.F., D.J.C. Yates, and J.H. Sinfelt, *Catalysis over Supported Metals .2. Effect of Support on Catalytic Activity of Nickel for Ethane Hydrogenolysis*. Journal of Physical Chemistry, 1964. **68**(10): p. 2962-&.
159. Shahrjerdi, D., et al., *Unpinned metal gate/high-kappa GaAs capacitors: Fabrication and characterization*. Applied Physics Letters, 2006. **89**(4).
160. Deak, D.S., *Strontium titanate surfaces (vol 23, pg 127, 2007)*. Materials Science and Technology, 2007. **23**(5): p. 630-630.
161. Christensen, S.T., et al., *Nanoscale Structure and Morphology of Atomic Layer Deposition Platinum on SrTiO₃ (001)*. Chemistry of Materials, 2009. **21**(3): p. 516-521.
162. Zhou, Y., et al., *Growth of Pt Particles on the Anatase TiO₂ (101) Surface*. Journal of Physical Chemistry C, 2012. **116**(22): p. 12114-12123.
163. Winterbo.WI, *Equilibrium Shape of a Small Particle in Contact with a Foreign Substrate*. Acta Metallurgica, 1967. **15**(2): p. 303-&.
164. Aaltonen, T., et al., *Reaction mechanism studies on atomic layer deposition of ruthenium and platinum*. Electrochemical and Solid State Letters, 2003. **6**(9): p. C130-C133.

165. Asthagiri, A. and D.S. Sholl, *First principles study of Pt adhesion and growth on SrO- and TiO₂-terminated SrTiO₃(100)*. Journal of Chemical Physics, 2002. **116**(22): p. 9914-9925.
166. Marsh, A.L. and J.L. Gland, *Mechanisms of deep benzene oxidation on the Pt(111) surface using temperature-programmed reaction methods*. Surface Science, 2003. **536**(1-3): p. 145-154.
167. Gland, J.L., B.A. Sexton, and G.B. Fisher, *Oxygen Interactions with the Pt(111) Surface*. Surface Science, 1980. **95**(2-3): p. 587-602.
168. Elliott, S.D., *Mechanism, Products, and Growth Rate of Atomic Layer Deposition of Noble Metals (vol 26, pg 9179, 2010)*. Langmuir, 2010. **26**(15): p. 13020-13020.
169. Kessels, W.M.M., et al., *Surface reactions during atomic layer deposition of Pt derived from gas phase infrared spectroscopy*. Applied Physics Letters, 2009. **95**(1).
170. Christensen, S.T. and J.W. Elam, *Atomic Layer Deposition of Ir-Pt Alloy Films*. Chemistry of Materials, 2010. **22**(8): p. 2517-2525.
171. Eisert, F., A.P. Elg, and A. Rosen, *Adsorption of Oxygen and Hydrogen on Pt(111) Studied with 2nd-Harmonic Generation*. Applied Physics a-Materials Science & Processing, 1995. **60**(2): p. 209-215.
172. Christensen, S.T.E., J. W. , *Atomic Layer Deposition of Ir-Pt Alloy Films*. Chem. Mater., 2010. **22**: p. 2517-2525.
173. Setthapun, W.W., W. D.; Kim, S. M.; Feng, H.; Elam, J. W.; Rabuffetti, F. A.; Poepelmeier, K. R.; Stair, P. C.; Stach, E. A.; Ribeiro, F. H.; Miller, J. T.; Marshall, C. L., *Genesis and Evolution of Surface Species during Pt Atomic Layer Deposition on Oxide Supports Characterized by in Situ XAFS Analysis and Water Gas Shift Reaction*. J. Phys. Chem. C 2010, . **114**: p. 9758–9771.
174. Enterkin, J.A., K.R. Poepelmeier, and L.D. Marks, *Oriented Catalytic Platinum Nanoparticles on High Surface Area Strontium Titanate Nanocuboids*. Nano Letters, 2011. **11**(3): p. 993-997.
175. Giordano, L., et al., *Nucleation of Pd dimers at defect sites of the MgO(100) surface*. Physical Review Letters, 2004. **92**(9).
176. Haas, G., et al., *Nucleation and growth of supported clusters at defect sites: Pd/MgO(001)*. Physical Review B, 2000. **61**(16): p. 11105-11108.
177. Gu, C.K., et al., *Formation of Metal-Semiconductor Core-shell Nanoparticles Using Electrochemical Atomic Layer Deposition*. Atomic Layer Deposition Applications 4, 2008. **16**(4): p. 181-190.
178. Citir, M., et al., *Direct determination of the ionization energies of PtC, PtO, and PtO₂ with VUV radiation*. Journal of Physical Chemistry A, 2008. **112**(39): p. 9584-9590.

179. Campbell, C.T. and J.R.V. Sellers, *Anchored metal nanoparticles: Effects of support and size on their energy, sintering resistance and reactivity*. Faraday Discuss., 2013. **162**(Fabrication, Structure and Reactivity of Anchored Nanoparticles): p. 9-30.
180. Harris, P.J.F., *Growth and Structure of Supported Metal Catalyst Particles*. International Materials Reviews, 1995. **40**(3): p. 97-115.
181. Blakely, J.M. and H. Mykura, *Surface Self Diffusion and Surface Energy Measurements on Platinum by Multiple Scratch Method*. Acta Metallurgica, 1962. **10**(May): p. 565-&.
182. Mackus, A.J.M.L., N.; Baker, L.; Kessels, W. M. M. , *Catalytic Combustion and Dehydrogenation Reactions during Atomic Layer Deposition of Platinum*. Chem. Mater. , 2012. **24** p. 1752-1761.
183. Pentcheva, R. and A.E. Pickett, *Electronic phenomena at complex oxide interfaces: insights from first principles*. Journal of Physics-Condensed Matter, 2010. **22**(4).
184. Joshi, P.C. and S.B. Krupanidhi, *Structural and Electrical Characteristics of SrTiO₃ Thin-Films for Dynamic Random-Access Memory Applications*. Journal of Applied Physics, 1993. **73**(11): p. 7627-7634.
185. Hodak, S.K., et al., *Design of Low Cost Gas Sensor Based on SrTiO₃ and BaTiO₃ Films*. Journal of Nanoscience and Nanotechnology, 2010. **10**(11): p. 7236-7238.
186. Hu, Y., et al., *A new form of nanosized SrTiO₃ material for near-human-body temperature oxygen sensing applications*. Journal of Physical Chemistry B, 2004. **108**(30): p. 11214-11218.
187. Zhao, T., et al., *Stress-induced enhancement of second-order nonlinear optical susceptibilities of barium titanate films*. Journal of Applied Physics, 2000. **87**(10): p. 7448-7451.
188. Moret, M.P., et al., *Optical properties of PbTiO₃, PbZrxTi1-xO₃, and PbZrO₃ films deposited by metalorganic chemical vapor on SrTiO₃*. Journal of Applied Physics, 2002. **92**(1): p. 468-474.
189. Cardin, J., et al., *Pb(Zr,Ti)O₃ ceramic thick films for optical device applications*. Advanced Organic and Inorganic Optical Materials, 2003. **5122**: p. 371-376.
190. Enterkin, J.A., et al., *Propane Oxidation over Pt/SrTiO₃ Nanocuboids*. Acs Catalysis, 2011. **1**(6): p. 629-635.
191. Li, X.C., L.T. Luo, and K.Q. Liu, *Preparation and catalytic performance of superfine Ni/BaTiO₃ catalyst*. Reaction Kinetics and Catalysis Letters, 2003. **80**(2): p. 261-268.
192. Sulaeman, U., S. Yin, and T. Sato, *Effect of Sr/Ti Ratio on the Photocatalytic Properties of SrTiO₃*. 3rd International Congress on Ceramics (Icc): Novel Chemical Processing Sol-Gel and Solution-Based Processing, 2011. **18**.

193. Prade, J., et al., *Surface Relaxation, Surface Reconstruction and Surface Dynamics Close to the Antiferrodistortive Phase-Transition of SrTiO₃(001) Slabs with Free SrO and TiO₂ Surfaces*. Journal of Physics-Condensed Matter, 1993. **5**(1): p. 1-12.
194. Erdman, N., et al., *Surface structures of SrTiO₃ (001): A TiO₂-rich reconstruction with a c(4 x 2) unit cell*. Journal of the American Chemical Society, 2003. **125**(33): p. 10050-10056.
195. Erdman, N., et al., *The structure and chemistry of the TiO₂-rich surface of SrTiO₃(001)*. Nature, 2002. **419**(6902): p. 55-58.
196. Jiang, Q.D. and J. Zegenhagen, *SrTiO₃(001) Surfaces and Growth of Ultra-Thin GdBa₂Cu₃O_{7-x} Films Studied by Leed/Aes and UHV-Stm*. Surface Science, 1995. **338**(1-3): p. L882-L888.
197. Matsumoto, T., et al., *Stm-Imaging of a SrTiO₃(100) Surface with Atomic-Scale Resolution*. Surface Science, 1992. **278**(3): p. L153-L158.
198. Johnston, K., et al., *SrTiO₃(001)(2x1) reconstructions: First-principles calculations of surface energy and atomic structure compared with scanning tunneling microscopy images*. Physical Review B, 2004. **70**(8).
199. Kobayashi, D., et al., *High-resolution synchrotron-radiation photoemission characterization for atomically-controlled SrTiO₃(001) substrate surfaces subjected to various surface treatments*. Journal of Applied Physics, 2004. **96**(12): p. 7183-7188.
200. Kuang, Q. and S.H. Yang, *Template Synthesis of Single-Crystal-Like Porous SrTiO₃ Nanocube Assemblies and Their Enhanced Photocatalytic Hydrogen Evolution*. ACS Applied Materials & Interfaces, 2013. **5**(9): p. 3683-3690.
201. Hu, W.B., et al., *Synthesis and characterization of In₂O₃ nanocube via a solvothermal-calcination route*. Materials Chemistry and Physics, 2009. **118**(2-3): p. 277-280.
202. Du, J.M., J.S. Zhang, and D.J. Kang, *Controlled synthesis of anatase TiO₂ nano-octahedra and nanospheres: shape-dependent effects on the optical and electrochemical properties*. Crystengcomm, 2011. **13**(12): p. 4270-4275.
203. Vehkamäki, M., et al., *Growth of SrTiO₃ and BaTiO₃ thin films by atomic layer deposition*. Electrochemical and Solid State Letters, 1999. **2**(10): p. 504-506.
204. Fan, H.M., et al., *Photoinduced Charge Transfer Properties and Photocatalytic Activity in Bi₂O₃/BaTiO₃ Composite Photocatalyst*. ACS Applied Materials & Interfaces, 2012. **4**(9): p. 4853-4857.
205. van Benthem, K., C. Elsasser, and R.H. French, *Bulk electronic structure of SrTiO₃: Experiment and theory*. Journal of Applied Physics, 2001. **90**(12): p. 6156-6164.

206. Maye, M.M., et al., *Mediator-template assembly of nanoparticles*. Journal of the American Chemical Society, 2005. **127**(5): p. 1519-1529.
207. Murray, C.B., C.R. Kagan, and M.G. Bawendi, *Self-Organization of Cdse Nanocrystallites into 3-Dimensional Quantum-Dot Superlattices*. Science, 1995. **270**(5240): p. 1335-1338.
208. Schrader, M.E., *Young-Dupre Revisited*. Langmuir, 1995. **11**(9): p. 3585-3589.
209. Zucker, R.V., et al., *New software tools for the calculation and display of isolated and attached interfacial-energy minimizing particle shapes*. Journal of Materials Science, 2012. **47**(24): p. 8290-8302.
210. Komanicky, V., et al., *Fabrication and characterization of platinum nanoparticle arrays of controlled size, shape and orientation*. Electrochimica Acta, 2010. **55**(27): p. 7934-7938.
211. Langmuir, I., *The mechanism of the catalytic action of platinum in the reactions $2CO + O_2 = 2CO_2$ and $2H_2 + O_2 = 2H_2O$* . Transactions of the Faraday Society, 1922. **17**(2): p. 0621-0654.
212. Bar, M., et al., *Theoretical Modeling of Spatiotemporal Self-Organization in a Surface Catalyzed Reaction Exhibiting Bistable Kinetics*. Journal of Chemical Physics, 1992. **96**(11): p. 8595-8604.
213. Andrade, R.F.S., G. Dewel, and P. Borckmans, *Modeling of the Kinetic Oscillations in the Co Oxidation on Pt(100)*. Journal of Chemical Physics, 1989. **91**(4): p. 2675-2682.
214. Mai, J., W. Vonniessen, and A. Blumen, *The Co+O₂ Reaction on Metal-Surfaces - Simulation and Mean-Field Theory - the Influence of Diffusion*. Journal of Chemical Physics, 1990. **93**(5): p. 3685-3692.
215. Ziff, R.M., E. Gulari, and Y. Barshad, *Kinetic Phase-Transitions in an Irreversible Surface-Reaction Model*. Physical Review Letters, 1986. **56**(24): p. 2553-2556.
216. Kang, Y., et al., *Heterogeneous Catalysts Need Not Be so "Heterogeneous": Monodisperse Pt Nanocrystals by Combining Shape-Controlled Synthesis and Purification by Colloidal Recrystallization*. Journal of the American Chemical Society, 2013. **135**(7): p. 2741-2747.
217. Xie, X.W., et al., *Low-temperature oxidation of CO catalysed by Co₃O₄ nanorods*. Nature, 2009. **458**(7239): p. 746-749.
218. Campbell, C.T., et al., *A Molecular-Beam Study of the Catalytic-Oxidation of Co on a Pt(111) Surface*. Journal of Chemical Physics, 1980. **73**(11): p. 5862-5873.
219. Ertl, G., *Oscillatory Kinetics and Spatiotemporal Self-Organization in Reactions at Solid-Surfaces*. Science, 1991. **254**(5039): p. 1750-1755.

220. Allers, K.H., et al., *Fast Reaction-Products from the Oxidation of Co on Pt(111) - Angular and Velocity Distributions of the Co₂ Product Molecules*. Journal of Chemical Physics, 1994. **100**(5): p. 3985-3998.
221. Bald, D.J., R. Kunkel, and S.L. Bernasek, *Diode laser absorption study of internal energies of CO₂ produced from catalytic CO oxidation*. Journal of Chemical Physics, 1996. **104**(19): p. 7719-7728.
222. Falta, J., et al., *Low-Energy Electron-Diffraction Profile Analysis of Reaction-Induced Substrate Changes on Pt(110) during Catalytic Co Oxidation*. Physical Review B, 1992. **45**(12): p. 6858-6867.
223. Kummer, J.T., *Use of Noble-Metals in Automobile Exhaust Catalysts*. Journal of Physical Chemistry, 1986. **90**(20): p. 4747-4752.
224. Shelef, M. and R.W. McCabe, *Twenty-five years after introduction of automotive catalysts: what next?* Catalysis Today, 2000. **62**(1): p. 35-50.
225. Twigg, M.V., *Progress and future challenges in controlling automotive exhaust gas emissions*. Applied Catalysis B-Environmental, 2007. **70**(1-4): p. 2-15.
226. Trimm, D.L. and Z.I. Onsan, *Onboard fuel conversion for hydrogen-fuel-cell-driven vehicles*. Catalysis Reviews-Science and Engineering, 2001. **43**(1-2): p. 31-84.
227. Oh, S.H. and G.B. Hoflund, *Low-temperature catalytic carbon monoxide oxidation over hydrous and anhydrous palladium oxide powders*. Journal of Catalysis, 2007. **245**(1): p. 35-44.
228. Mott, D., et al., *Synergistic activity of gold-platinum alloy nanoparticle catalysts*. Catalysis Today, 2007. **122**(3-4): p. 378-385.
229. Bradley, J.S., et al., *Infrared and EXAFS study of compositional effects in nanoscale colloidal palladium-copper alloys*. Chemistry of Materials, 1996. **8**(8): p. 1895-1903.
230. Toshima, N. and T. Yonezawa, *Bimetallic nanoparticles - novel materials for chemical and physical applications*. New Journal of Chemistry, 1998. **22**(11): p. 1179-1201.
231. Park, S., et al., *Electrochemical infrared characterization of CO domains on ruthenium decorated platinum nanoparticles*. Abstracts of Papers of the American Chemical Society, 2003. **225**: p. U619-U619.
232. deMenorval, L.C., et al., *Characterization of mono- and bi-metallic platinum catalysts using CO FTIR spectroscopy - Size effects and topological segregation*. Journal of the Chemical Society-Faraday Transactions, 1997. **93**(20): p. 3715-3720.
233. Blyholder, G., *Molecular Orbital View of Chemisorbed Carbon Monoxide*. Journal of Physical Chemistry, 1964. **68**(10): p. 2772-&.

234. Blyholder, G., *Cndo Model of Carbon-Monoxide Chemisorbed on Nickel*. Journal of Physical Chemistry, 1975. **79**(7): p. 756-761.
235. Greenler, R.G., et al., *Stepped Single-Crystal Surfaces as Models for Small Catalyst Particles*. Surface Science, 1985. **152**(Apr): p. 338-345.
236. Kappers, M.J. and J.H. Vandermaas, *Correlation between Co Frequency and Pt Coordination-Number - a Drift Study on Supported Pt Catalysts*. Catalysis Letters, 1991. **10**(5-6): p. 365-373.
237. Hammaker, R.M., S.A. Francis, and R.P. Eischens, *Infrared Study of Intermolecular Interactions for Carbon Monoxide Chemisorbed on Platinum*. Spectrochimica Acta, 1965. **21**(7): p. 1295-&.
238. Crossley, A. and D.A. King, *Infrared-Spectra for Co Isotopes Chemisorbed on Pt[111] - Evidence for Strong Adsorbate Coupling Interactions*. Surface Science, 1977. **68**(1): p. 528-538.
239. Stoop, F., F.J.C.M. Toolenaar, and V. Ponec, *Geometric and Ligand Effects in the Infrared-Spectra of Adsorbed Carbon-Monoxide*. Journal of Catalysis, 1982. **73**(1): p. 50-56.
240. Bartok, M., J. Sarkany, and A. Sitkei, *Investigation of Interactions between Metals and Adsorbed Organic-Compounds by Infrared Spectroscopic Study of Adsorbed Co .1. Infrared Study of Co Adsorption and Desorption on Pt/Cab-O-Sil Catalyst*. Journal of Catalysis, 1981. **72**(2): p. 236-245.
241. Qiao, B.T., et al., *Single-atom catalysis of CO oxidation using Pt-1/FeOx*. Nature Chemistry, 2011. **3**(8): p. 634-641.